Supplementary Material

Simon Seelig[1], Magdalena Seelig[1], Matevž Vremec[1,2], Martin Masten[1], Thomas Wagner[1], Karl Krainer[3], Michael Avian[4], Klaus Haslinger[4], Heike Brielmann[5], Albrecht Leis[6], Markus Ribis[7], Maria Obwegs[8], Matthias Hausleber[9], Rudolf Philippitsch[10], Richild Mauthner-Weber[10], Ernst Überreiter[10], Gerfried Winkler[1]

[1]Department of Earth Sciences, NAWI Graz Geocenter, University of Graz, Heinrichstraße 26, 8010 Graz, Austria
[2]Alma Mater Europaea University, Slovenska ulica 17, 2000 Maribor, Slovenia
[3]Institute of Geology, University of Innsbruck, Innrain 52, 6020 Innsbruck, Austria
[4]Department of Climate Impact Research, GeoSphere Austria, Hohe Warte 38, 1190 Vienna, Austria
[5]Team Groundwater, Environment Agency Austria, Spittelauer Lände 5, 1090 Vienna, Austria
[6]JR-AquaConSol, Steyrergasse 21, 8010 Graz, Austria
[7]geo.zt gmbh poscher beratende geologen, Saline 17, 6060 Hall in Tirol, Austria
[8]now at Geo Group Austria ZT GmbH, Reininghausstraße 13a, 8020 Graz, Austria
[9]now at Geoconsult ZT GmbH, Leechgasse 37, 8010 Graz, Austria
[10]Federal Ministry of Agriculture and Forestry, Climate and Environmental Protection, Regions and Water Management, Marxergasse 2, 1030 Vienna, Austria

Correspondence to: Simon Seelig (simon.seelig@uni-graz.at)

This document provides additional details on study site characteristics, hydrological model structure and performance, projected climate change signals, and statistical analyses of hydrometeorological change across the investigated alpine catchments. Supplementary Figures S1–S9 summarize the characteristics of the study sites. Supplementary Figure S10 illustrates the applied hydrological model structure. Model performance during the historical period is presented for each subcatchment in Supplementary Figures S11–S25.

Projected climate change signals for runoff and snow cover at the individual catchment scale are shown in Supplementary Figures S26–S35. Supplementary Figure S36 shows projected changes in hydrometeorological related to snow dynamics and atmospheric drivers across the five study sites. Supplementary Figure S37 illustrates how seasonal runoff shifts scale with the percentage of catchment area draining through rock glaciers, while Supplementary Figure S38 examines this relationship for annual high- and low-flow extremes.

Supplementary Figures S39–S43 present projected changes in indices related to snow dynamics at the subcatchment scale. Extreme value analyses for individual catchments are provided in Supplementary Figures S44–S48. Supplementary Tables S1–S4 summarize Hodges–Lehmann estimates and corresponding p-values from rank-sum tests used to quantify projected changes in hydrometeorological indices and extreme events.

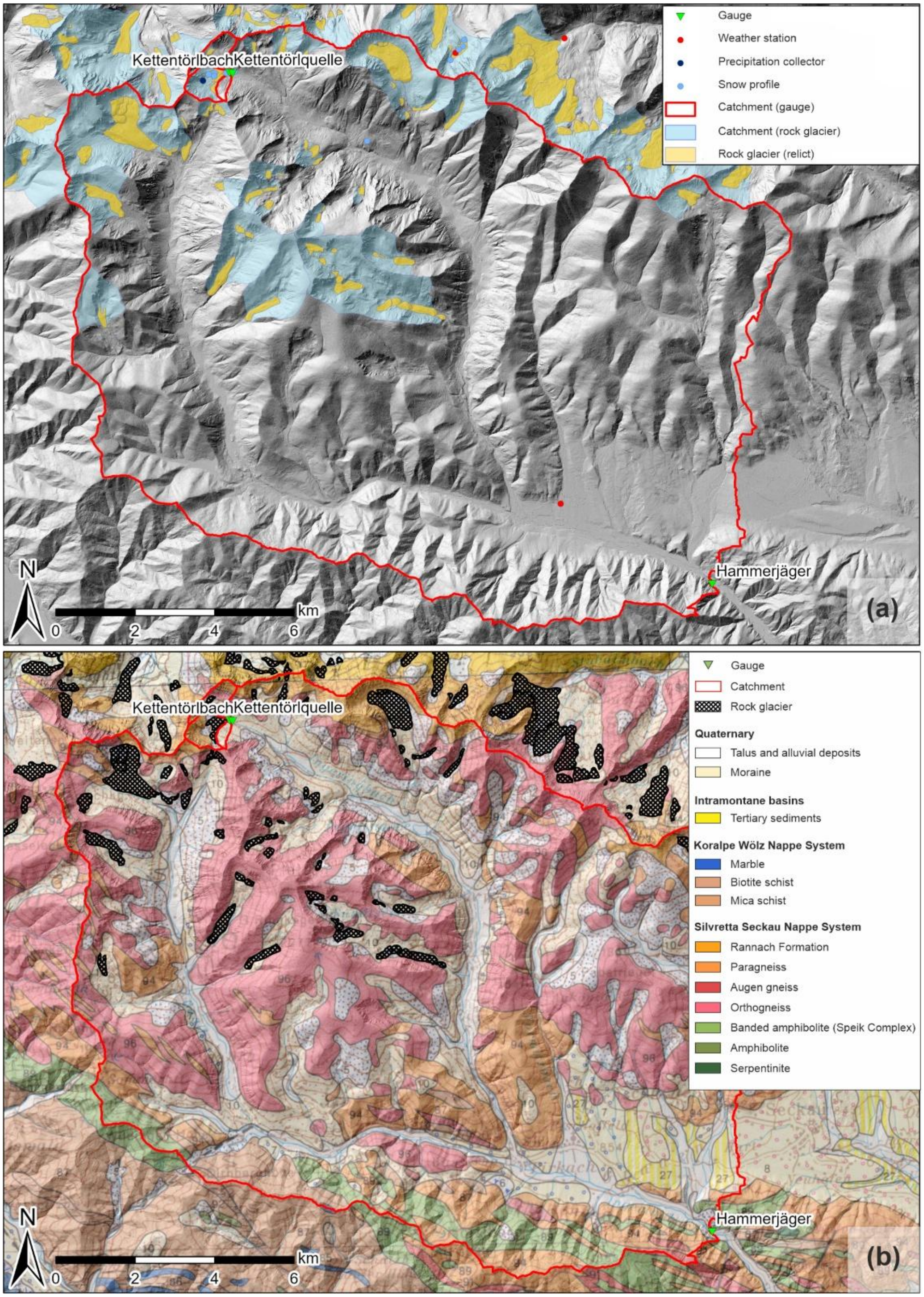

Supplementary Figure S1: Study area Seckau Alps, encompassing the Ingering and Gaal valleys (Styria). (a) Location of the gauging stations and their corresponding catchment areas, as well as the rock glaciers and their catchment areas. (b) Geological map of the study area. Data sources: Open Data Austria (www.data.gv.at), GeoSphere Austria (www.geologie.ac.at).

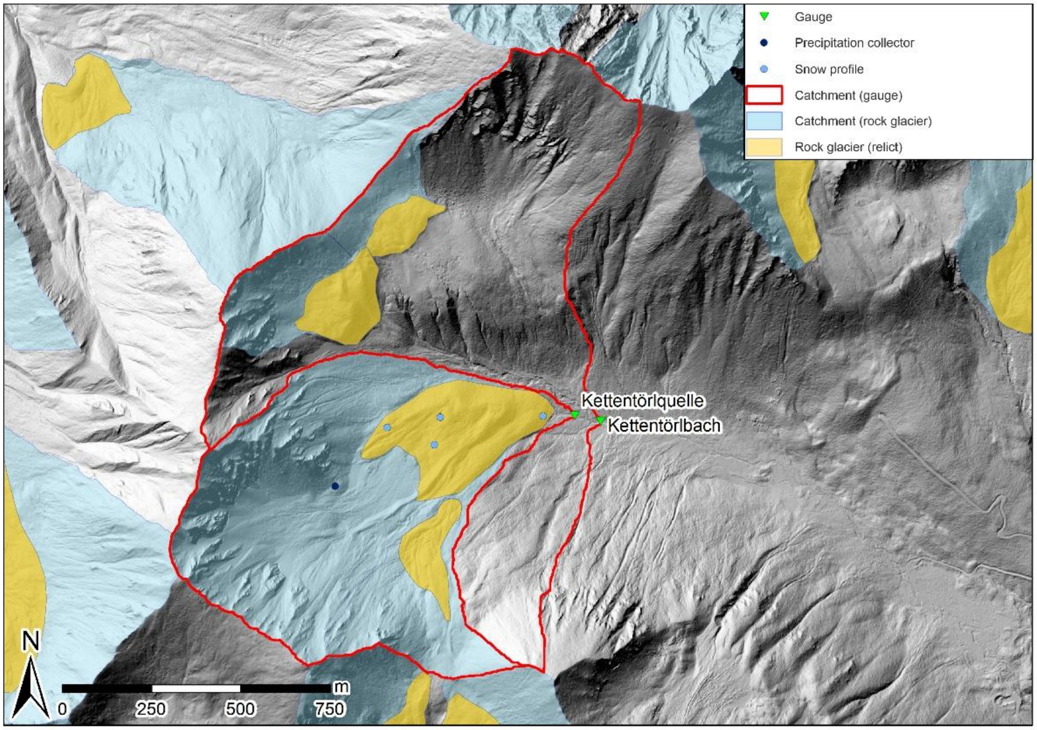

Supplementary Figure S2: Catchment areas of the Kettentörlquelle and Kettentörlbach catchments at the head of the Ingering Valley. The Kettentörlbach catchment features dominant rock slopes and alpine meadows. The nested Kettentörl spring catchment is 99% drained by two rock glaciers, with vegetation ranging from lower-reach mountain pine to high-elevation alpine grasslands and steep rock faces.

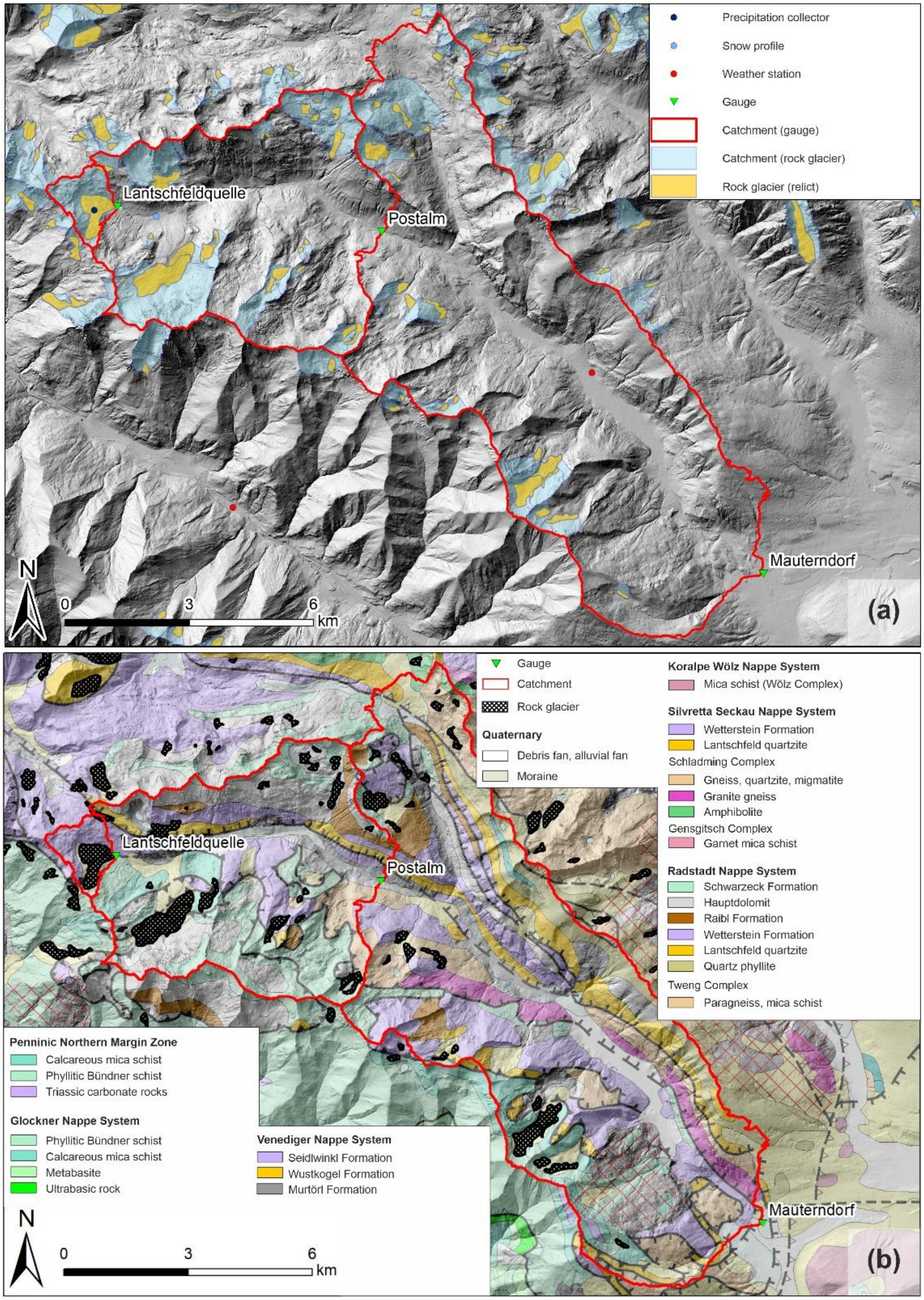

Supplementary Figure S3: Study area Radstadt Alps, encompassing Lantschfeld and Taurach valleys (Salzburg). (a) Location of the gauging stations and their associated catchment areas, as well as the rock glaciers and their catchment areas. (b) Geological map of the study area. Data sources: Open Data Austria (www.data.gv.at), GeoSphere Austria (www.geologie.ac.at).

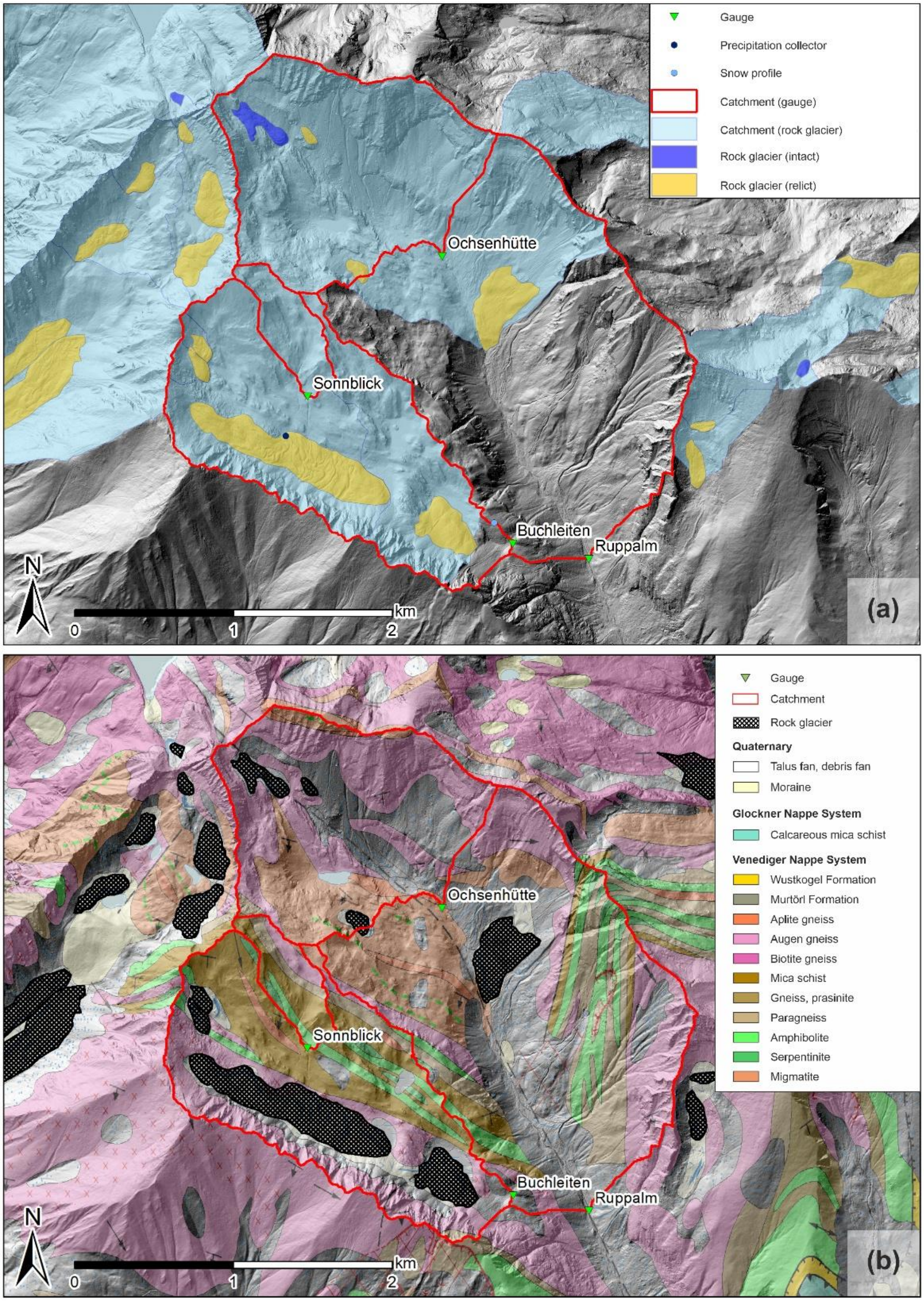

Supplementary Figure S4: Study area Reißeck Group (Carinthia). (a) Location of the gauging stations and their associated catchment areas, as well as the rock glaciers and their catchment areas. (b) Geological map of the study area. Data sources: Open Data Austria (www.data.gv.at), GeoSphere Austria (www.geologie.ac.at).

Supplementary Figure S5: Perennially standing water bodies in the Reißeck Group study area: (a) in the catchment of the Ochsenhütte gauging station (Hartriegelsee) and (b)–(f) in the catchment of the Buchleiten gauging station (Roßalm). Photos: Gerfried Winkler, Michael Avian, Simon Seelig.

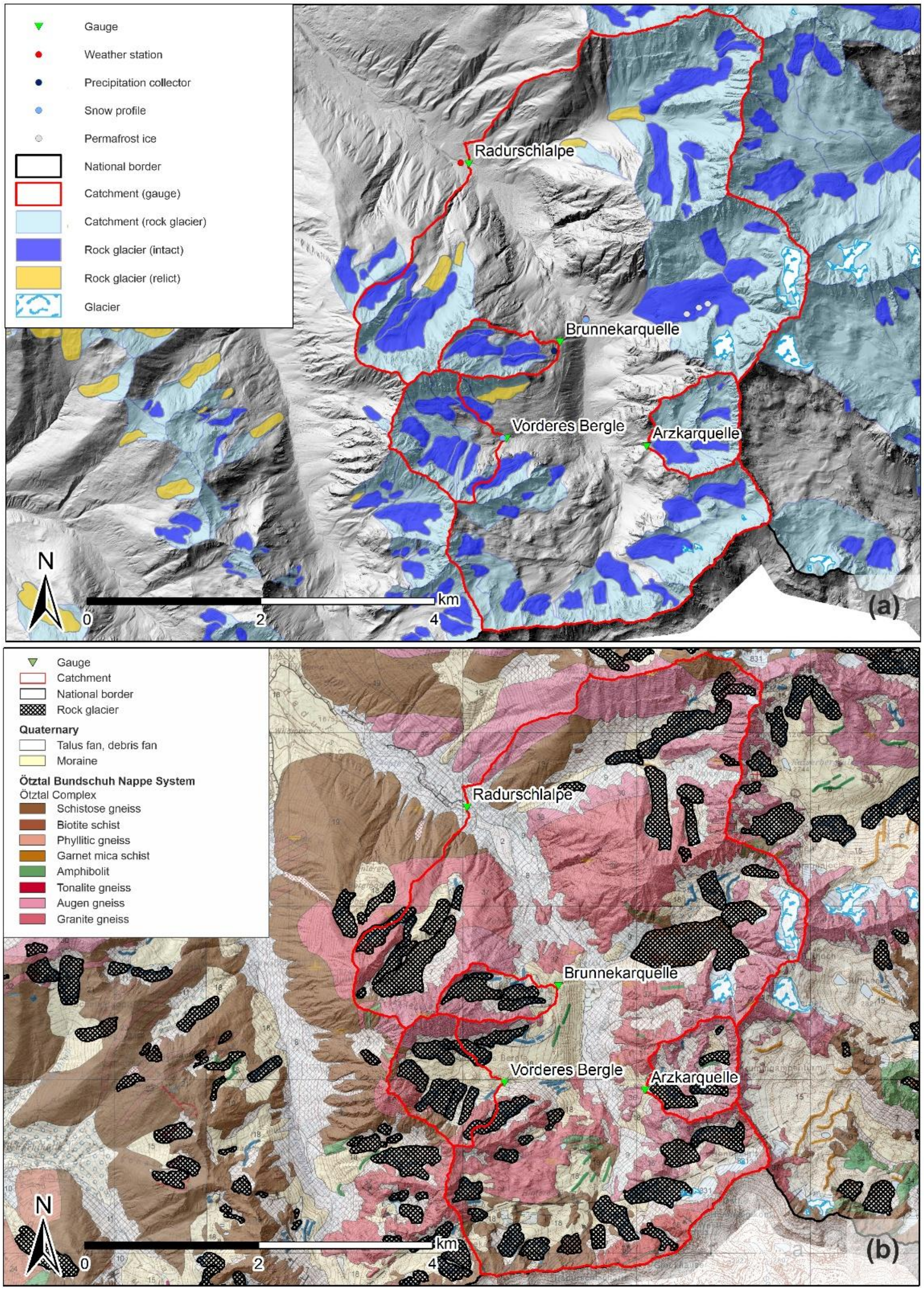

Supplementary Figure S6: Study area Ötztal Alps (Tyrol). (a) Location of the gauging stations and their associated catchment areas, the rock glaciers and their catchment areas, as well as the glaciers. (b) Geological map of the study area. Data sources: Open Data Austria (www.data.gv.at), GeoSphere Austria (www.geologie.ac.at).

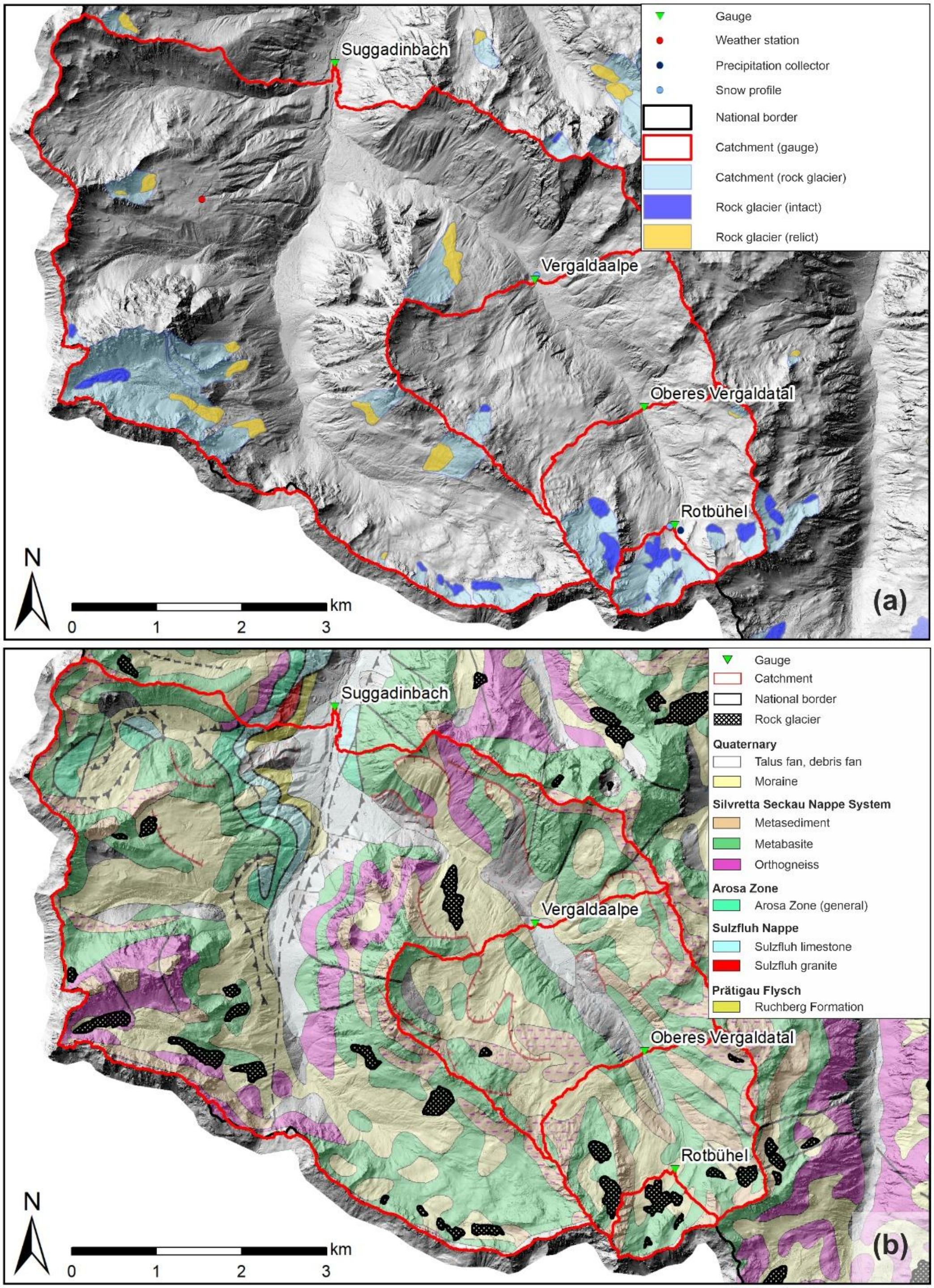

Supplementary Figure S7: Study area Silvretta Alps, encompassing Vergalda and Valzifenz valleys (Vorarlberg). (a) Location of the gauging stations and their associated catchment areas, as well as the rock glaciers and their catchment areas. (b) Geological map of the study area. Data sources: Open Data Austria (www.data.gv.at), GeoSphere Austria (www.geologie.ac.at).

Supplementary Figure S8: Rotbühel rock glacier, with lake at the rock glacier front draining the rock glacier and Eisentälispitze (2875 m) in the background. The Rotbühel gauging station is located downstream from the lake, which might affect hydrological modeling as detailed in the main text. Photo: Simon Seelig.

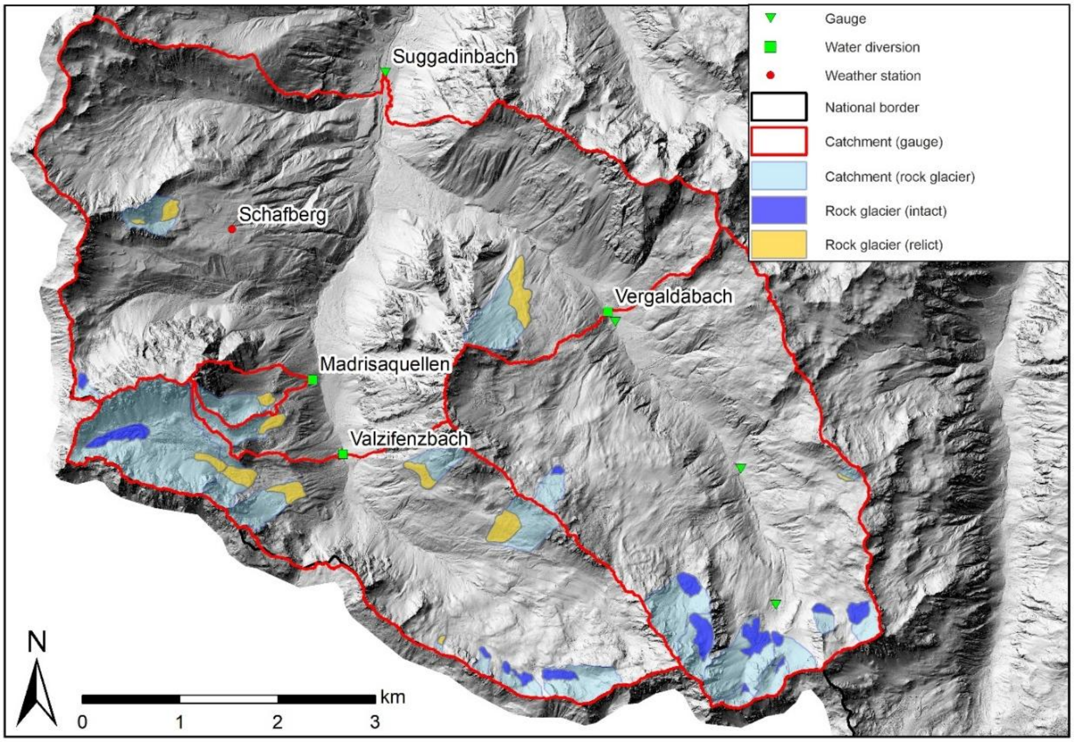

Supplementary Figure S9: Diversions in the Silvretta Alps study area and their associated catchment areas, including the locations of the gauging stations installed during this project. Data source: Open Data Austria (www.data.gv.at).

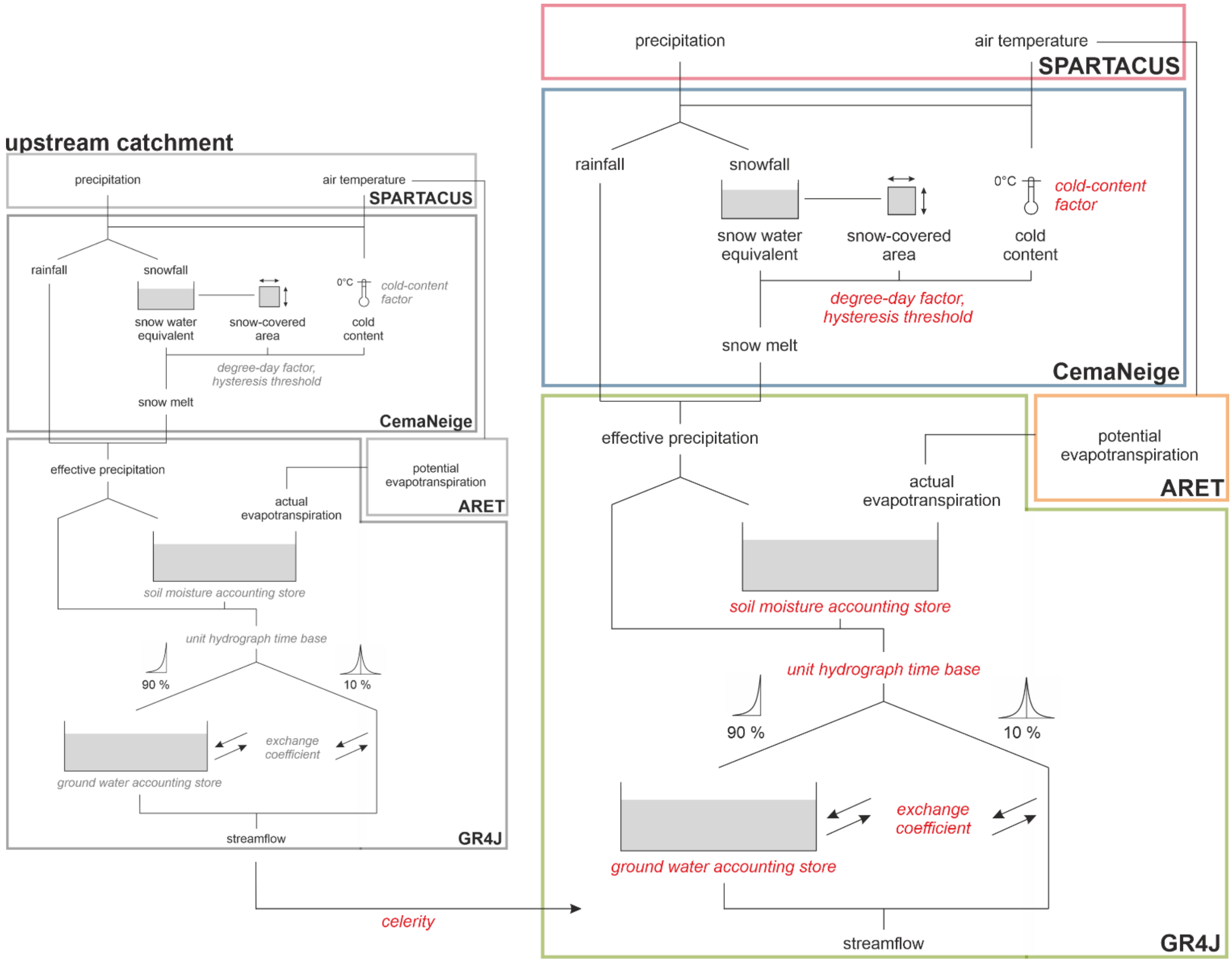

Supplementary Figure S10: Employed hydrological model structure, including data sources, the snow model structure of CemaNeige (Valéry et al., 2014b; Riboust et al., 2019) and the rainfall–runoff model structure of GR4J (Perrin et al., 2003). Parameters adjusted during model calibration are shown in red and italics. These were calibrated using multi-objective calibration against the observed discharge and snow cover extent. Input datasets were area-weighted and averaged daily over the investigated catchment. Cascading model framework structure: First, the upstream catchments were calibrated, followed by the downstream area with delayed inflow.

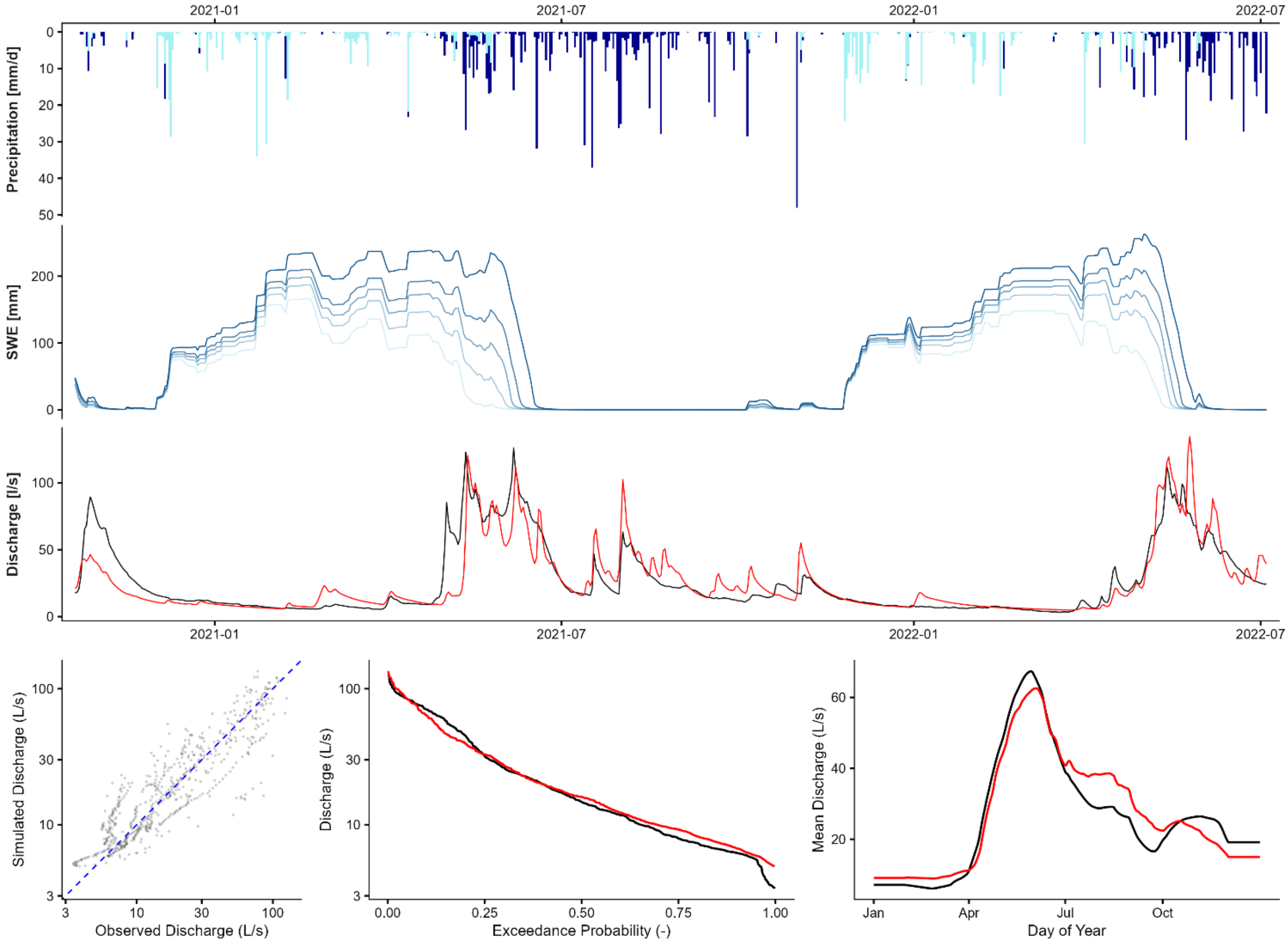

Supplementary Figure S11: Model results for the Kettentörlquelle catchment (Seckau Alps). The figure illustrates the simulated hydrological response of the catchment, including the partitioning of catchment-average precipitation into snowfall and rainfall. The temporal evolution of snow water equivalent (SWE) is shown as the catchment-wide median together with five elevation-band–resolved model time series. Simulated discharge is evaluated against observed discharge to assess the model's ability to reproduce streamflow dynamics. A set of complementary diagnostics is provided, including (i) a scatterplot of observed versus simulated discharge with a 1:1 reference line, (ii) flow duration curves comparing observed and simulated discharge to evaluate performance across low- and high-flow conditions, and (iii) a 30-day rolling mean of observed and simulated discharge highlighting seasonal dynamics. Model calibration was performed using daily discharge observations (weight = 75%) for the period 20.10.2020–04.07.2022 and satellite-derived snow-covered area (SCA; weight = 5% per each of five elevation bands) for 27.02.2000–30.12.2022, both at daily temporal resolution. Satellite-derived snow-covered area is only available under cloud-free conditions. Overall, the model captures both snow accumulation/melt dynamics and discharge variability well. Performance metrics for the calibration period indicate good agreement between simulations and observations, with KGE′ = 0.86, correlation coefficient = 0.87, coefficient of variation ratio = 0.99, and model bias = 1.01.

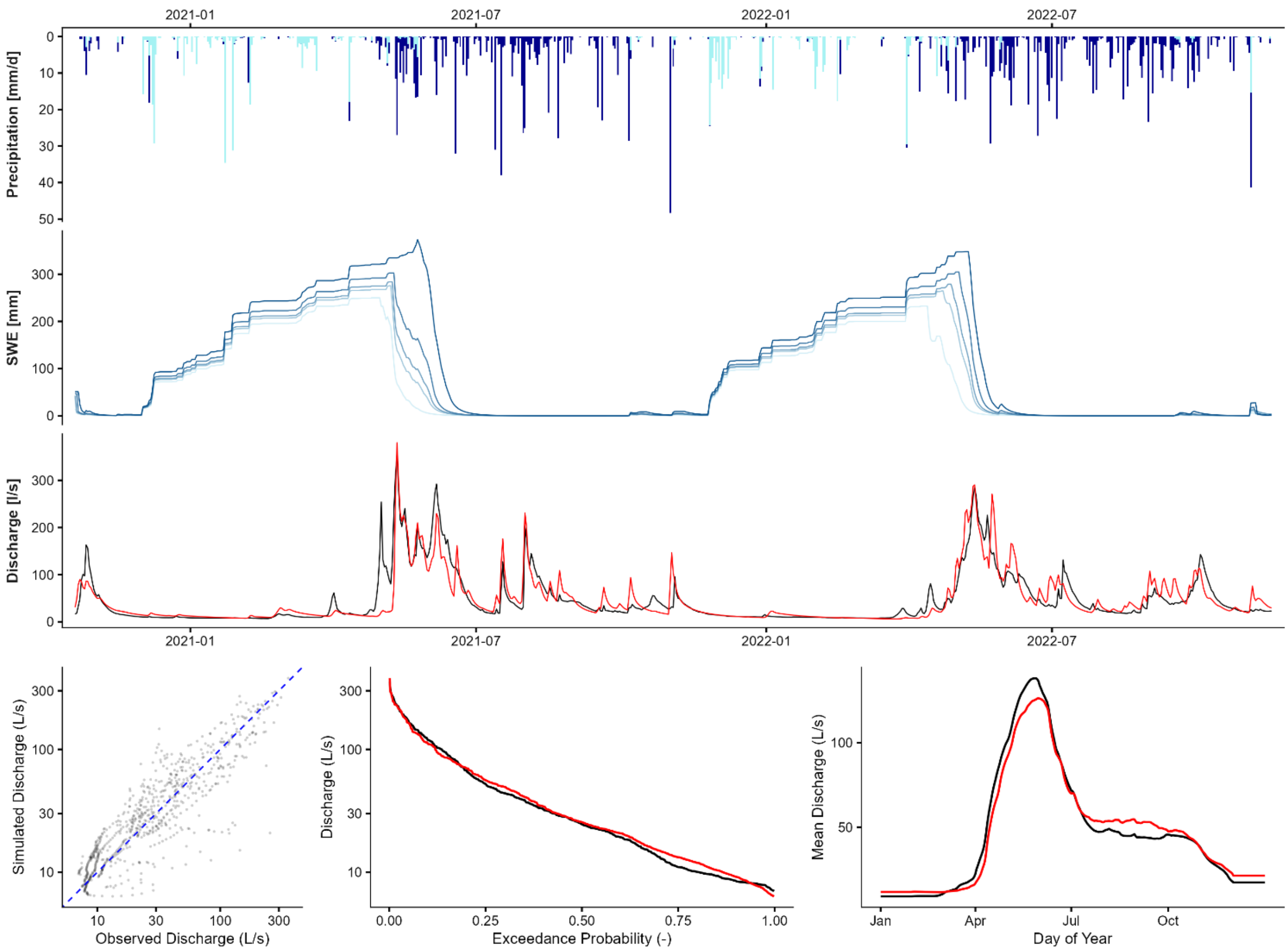

Supplementary Figure S12: Model results for the Kettentörlbach catchment (Seckau Alps). The figure shows the simulated hydrological response of the catchment, including the partitioning of catchment-average precipitation into snowfall and rainfall. The evolution of snow water equivalent (SWE) is presented as the catchment-wide median together with five elevation-band–resolved model time series. Simulated discharge is compared against observed discharge to evaluate the model's representation of runoff dynamics. A set of diagnostic plots is included, consisting of (i) a scatterplot of observed versus simulated discharge with a 1:1 reference line, (ii) flow duration curves comparing observed and simulated discharge across the full range of hydrological conditions, and (iii) a 30-day rolling mean of observed and simulated discharge highlighting seasonal variability. Model calibration was based on daily discharge observations (weight = 75%) for the period 20.10.2020–17.11.2022 and satellite-derived snow-covered area (SCA; weight = 5% per each of five elevation bands) for 27.02.2000–30.12.2022, both at daily temporal resolution. Satellite-derived snow-covered area is only available under cloud-free conditions. Overall, the model reproduces both snow dynamics and discharge variability well, with slightly stronger skill in streamflow dynamics compared to the previous catchment variant. Performance metrics for the calibration period indicate good agreement between simulations and observations, with KGE′ = 0.86, correlation coefficient = 0.89, coefficient of variation ratio = 0.99, and model bias = 1.02.

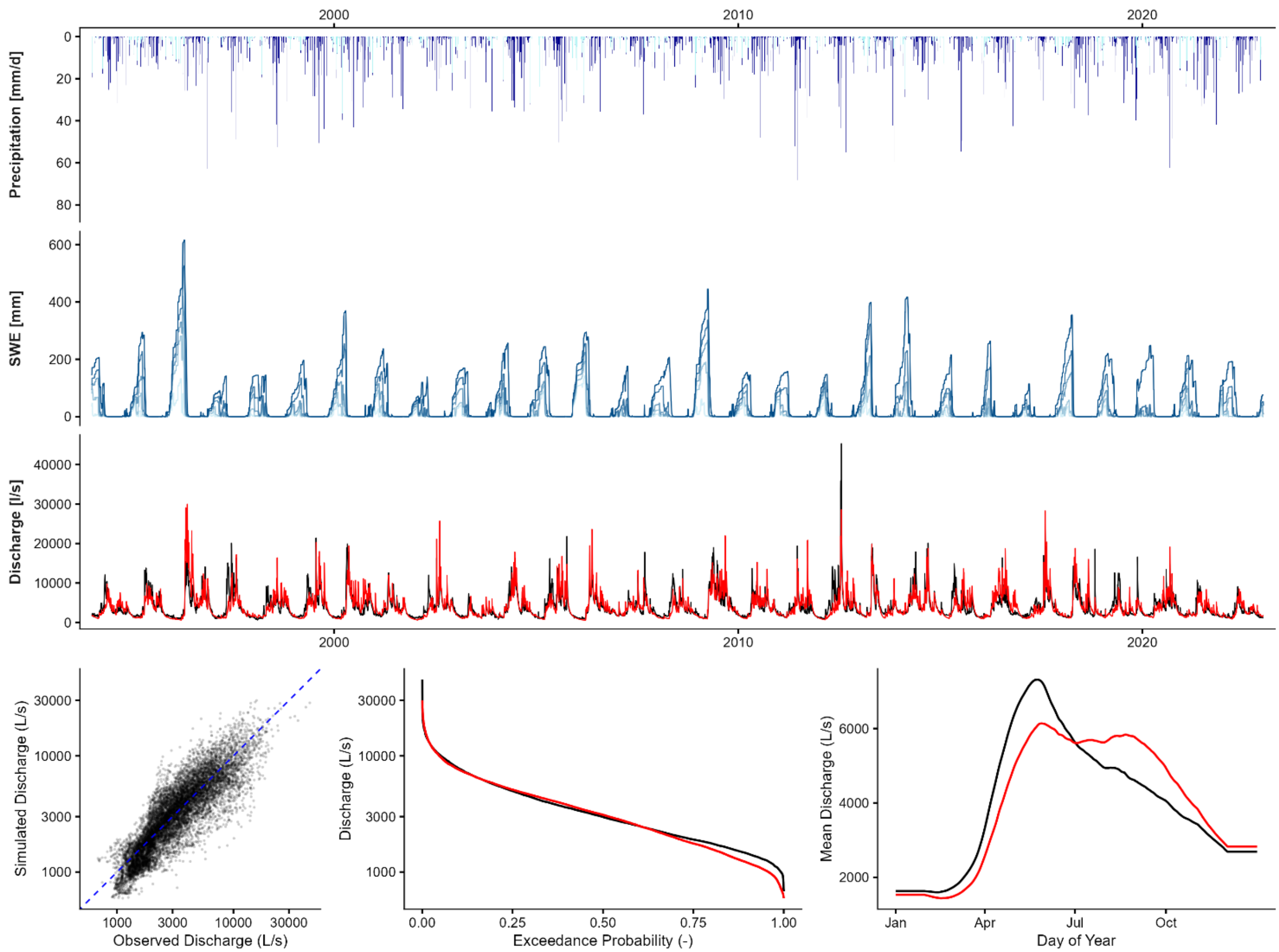

Supplementary Figure S13: Model results for the Hammerjäger catchment (Seckau Alps). The figure presents the simulated hydrological response of the catchment, including the partitioning of catchment-average precipitation into snowfall and rainfall components. The temporal evolution of snow water equivalent (SWE) is shown as the catchment-wide median together with five elevation-band–resolved model time series. Simulated discharge is compared with observed discharge to assess the model's ability to reproduce runoff dynamics. Diagnostic panels include (i) a scatterplot of observed versus simulated discharge with a 1:1 reference line, (ii) flow duration curves comparing observed and simulated discharge across the full range of hydrological conditions, and (iii) a 30-day rolling mean of observed and simulated discharge highlighting seasonal variability. Model calibration was based on daily discharge observations (weight = 75%) over the period 01.01.1994–31.12.2022 and satellite-derived snow-covered area (SCA; weight = 5% per each of five elevation bands) for 25.02.2000–31.12.2022, both at daily temporal resolution. Satellite-derived snow-covered area is only available under cloud-free conditions. Overall, the model reproduces snow dynamics and discharge variability with moderate skill, while showing slightly reduced performance compared to other catchments in the Seckau Alps. Performance metrics for the calibration period indicate reasonable agreement between simulations and observations, with KGE′ = 0.76, correlation coefficient = 0.81, coefficient of variation ratio = 1.08, and model bias = 1.04.

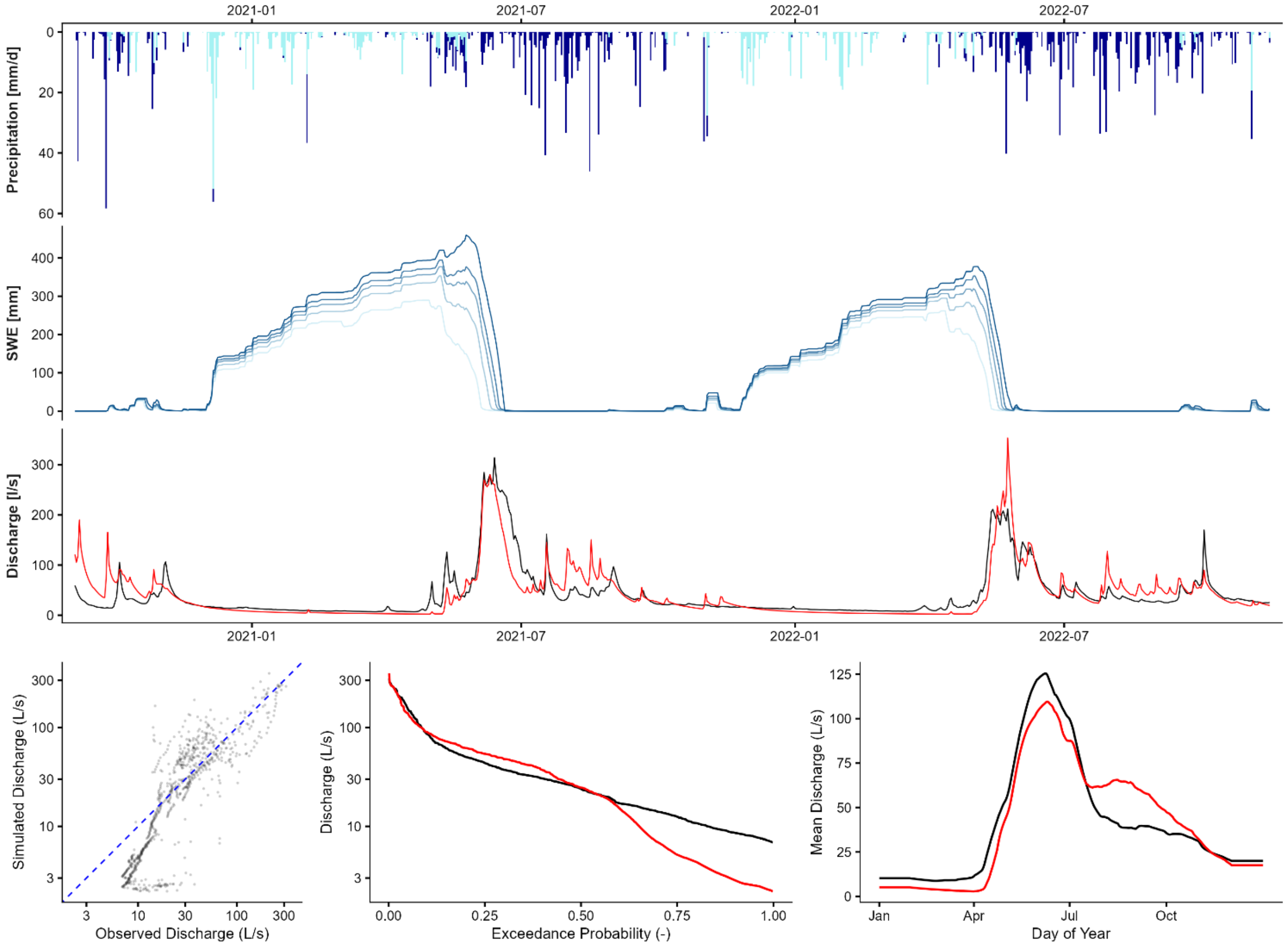

Supplementary Figure S14: Model results for the Lantschfeldquelle catchment (Radstadt Alps). The figure illustrates the simulated hydrological response of the catchment, including the partitioning of catchment-average precipitation into snowfall and rainfall components. The temporal evolution of snow water equivalent (SWE) is shown as the catchment-wide median together with five elevation-band–resolved model time series. Simulated discharge is evaluated against observed discharge to assess the model's representation of runoff dynamics. Diagnostic panels include (i) a scatterplot of observed versus simulated discharge with a 1:1 reference line, (ii) flow duration curves comparing observed and simulated discharge across the full range of hydrological conditions, and (iii) a 30-day rolling mean of observed and simulated discharge highlighting seasonal variability. Model calibration was based on daily discharge observations (weight = 75%) for the period 04.09.2020–16.11.2022 and satellite-derived snow-covered area (SCA; weight = 5% per each of five elevation bands) for 25.02.2000–31.12.2022, both at daily temporal resolution. Satellite-derived snow-covered area is only available under cloud-free conditions. Overall, the model captures both snow dynamics and streamflow variability well, although with slightly higher variability in simulated discharge compared to observations. Performance metrics for the calibration period indicate good agreement between simulations and observations, with KGE′ = 0.86, correlation coefficient = 0.87, coefficient of variation ratio = 1.02, and model bias = 1.01.

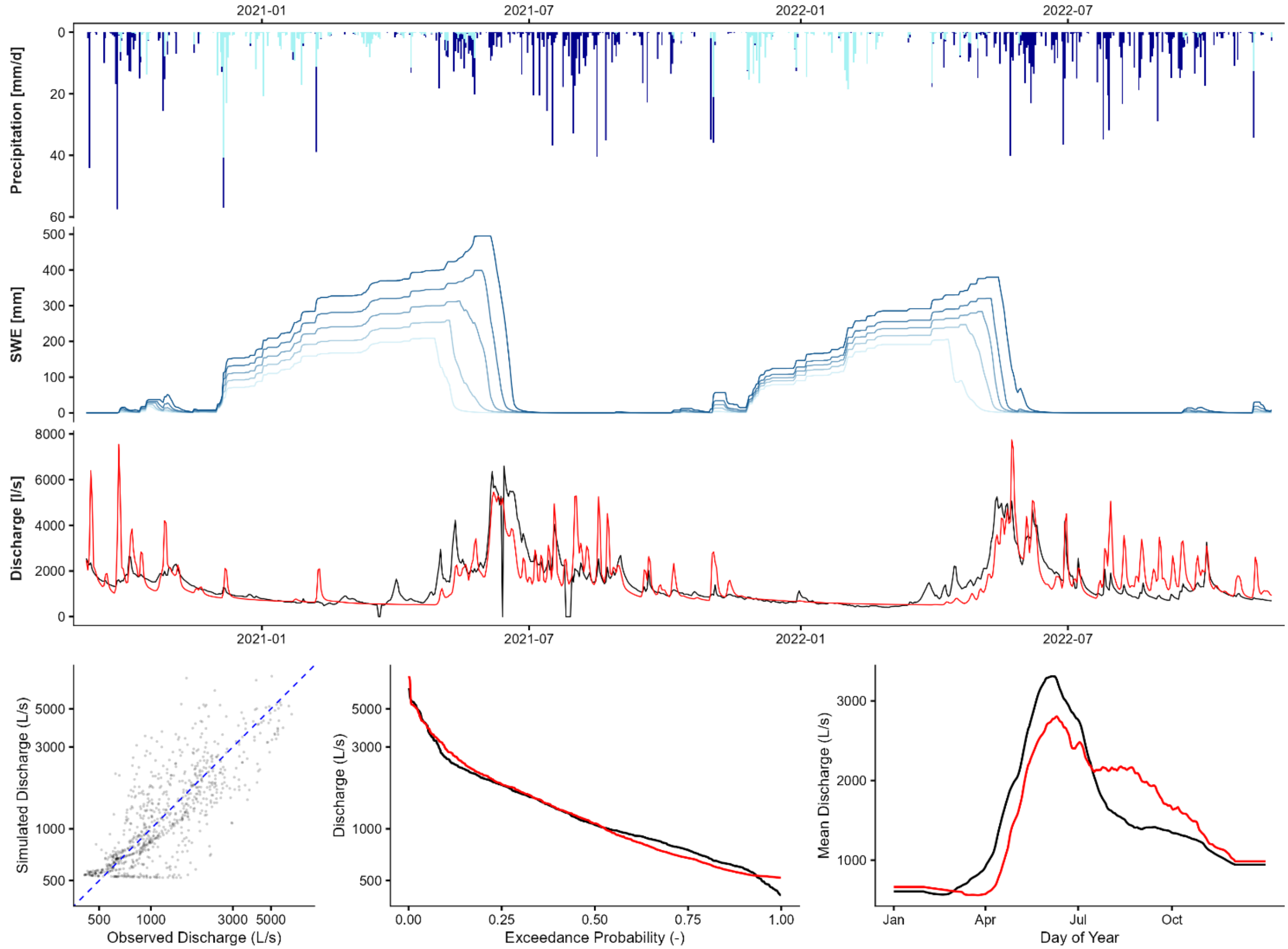

Supplementary Figure S15: Model results for the Postalm catchment (Radstadt Alps). The figure summarizes the simulated hydrological behaviour of the catchment, including the partitioning of catchment-average precipitation into snowfall and rainfall components. The temporal evolution of snow water equivalent (SWE) is shown as the catchment-wide median together with five elevation-band–resolved model time series. Simulated discharge is compared with observed discharge to evaluate the model's ability to reproduce runoff dynamics. Diagnostic panels include (i) a scatterplot of observed versus simulated discharge with a 1:1 reference line, (ii) flow duration curves comparing observed and simulated discharge across the full range of hydrological conditions, and (iii) a 30-day rolling mean of observed and simulated discharge highlighting seasonal variability. Model calibration was based on daily discharge observations (weight = 75%) for the period 04.09.2020–16.11.2022 and satellite-derived snow-covered area (SCA; weight = 5% per each of five elevation bands) for 25.02.2000–31.12.2022, both at daily temporal resolution. Satellite-derived snow-covered area is only available under cloud-free conditions. Overall, the model reproduces snow dynamics and streamflow variability, though with comparatively lower performance than most other Radstadt Alps catchments. Performance metrics for the calibration period indicate acceptable agreement between simulations and observations, with KGE′ = 0.74, correlation coefficient = 0.77, coefficient of variation ratio = 1.06, and model bias = 1.05.

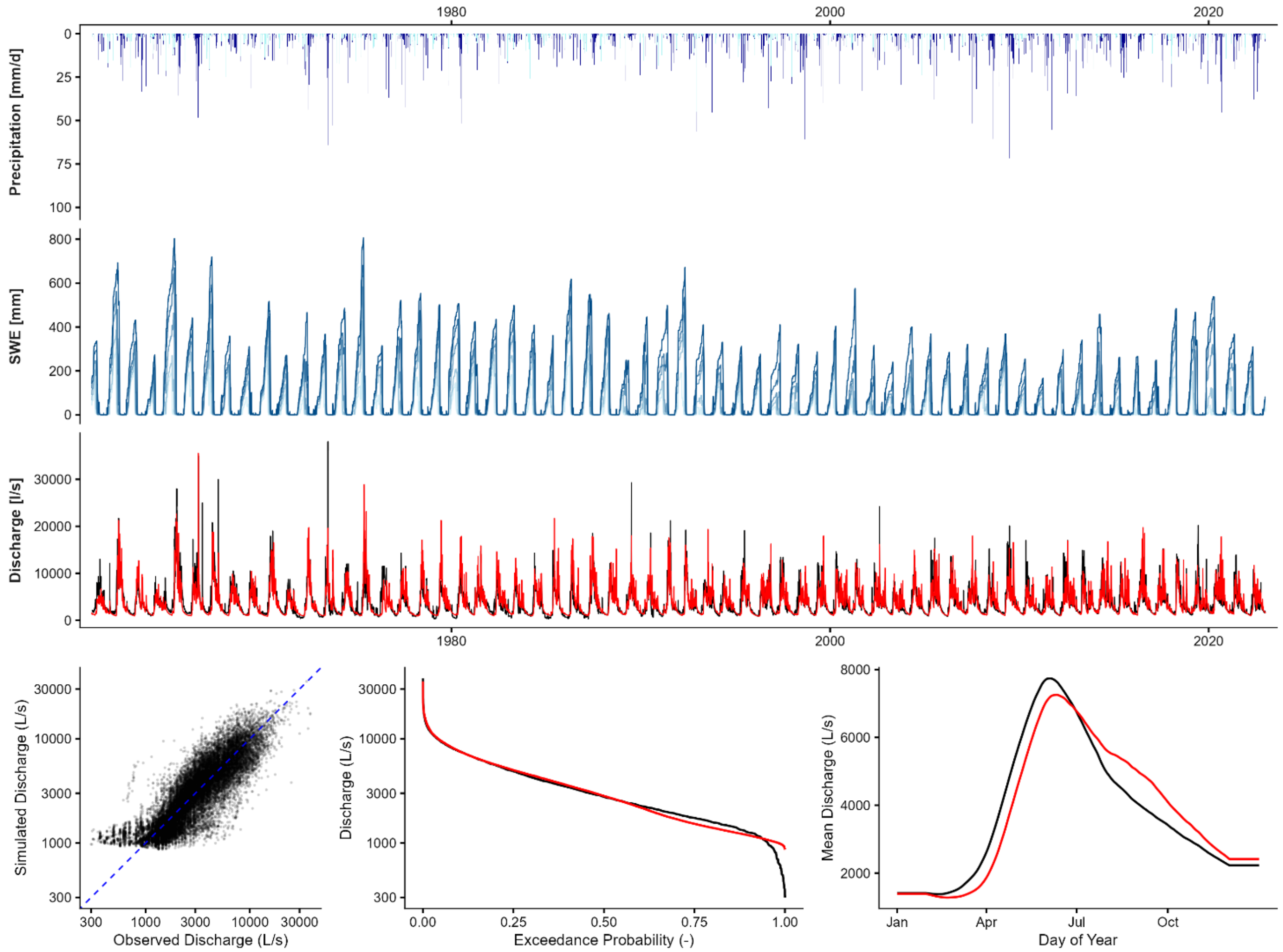

Supplementary Figure S16: Model results for the Mauterndorf catchment (Radstadt Alps). The figure depicts the simulated hydrological behaviour of the catchment, including the partitioning of catchment-average precipitation into snowfall and rainfall components. The temporal evolution of snow water equivalent (SWE) is shown as the catchment-wide median together with five elevation-band–resolved model time series. Simulated discharge is evaluated against observed discharge to assess the model's ability to reproduce runoff dynamics. Complementary diagnostic panels include (i) a scatterplot of observed versus simulated discharge with a 1:1 reference line, (ii) flow duration curves comparing observed and simulated discharge across the full hydrological range, and (iii) a 30-day rolling mean of observed and simulated discharge highlighting seasonal variability. Model calibration was based on daily discharge observations (weight = 75%) over the extended period 01.11.1961–31.12.2022 and satellite-derived snow-covered area (SCA; weight = 5% per each of five elevation bands) for 25.02.2000–31.12.2022, both at daily temporal resolution. Satellite-derived snow-covered area is only available under cloud-free conditions. Overall, the model reproduces snow dynamics and discharge variability reasonably well over the long calibration period, with some degradation in performance compared to shorter, more recent calibration windows. Performance metrics indicate satisfactory agreement between simulations and observations, with KGE′ = 0.79, correlation coefficient = 0.83, coefficient of variation ratio = 1.07, and model bias = 1.04.

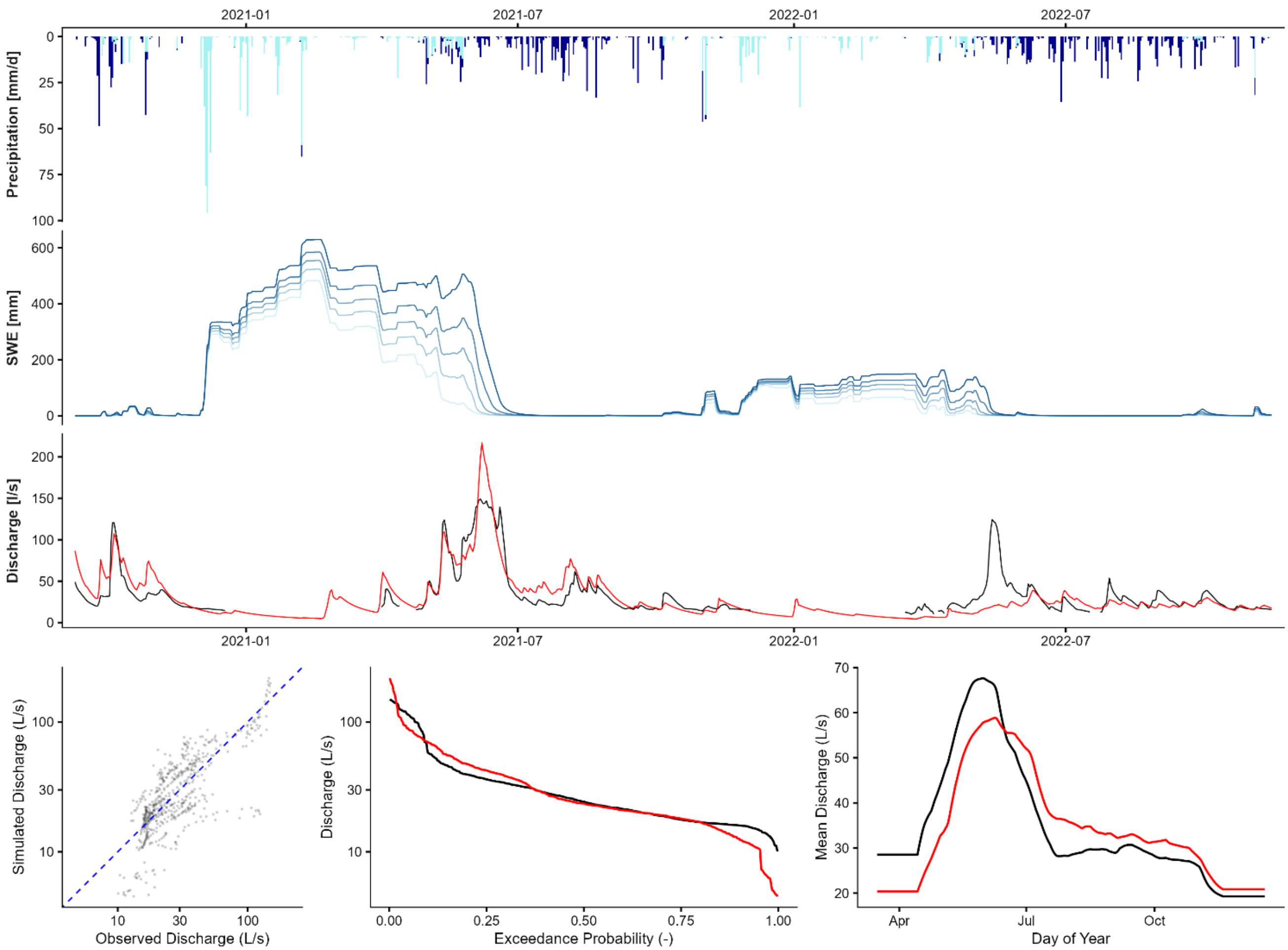

Supplementary Figure S17: Model results for the Buchleiten catchment (Reißeck Group). The figure presents the simulated hydrological response of the catchment, including the partitioning of catchment-average precipitation into snowfall and rainfall components. The temporal evolution of snow water equivalent (SWE) is shown as the catchment-wide median together with five elevation-band–resolved model time series. Simulated discharge is compared with observed discharge to evaluate the model's ability to reproduce runoff dynamics. Diagnostic panels include (i) a scatterplot of observed versus simulated discharge with a 1:1 reference line, (ii) flow duration curves comparing observed and simulated discharge across the full range of hydrological conditions, and (iii) a 30-day rolling mean of observed and simulated discharge highlighting seasonal variability. Model calibration was based on daily discharge observations (weight = 75%) over the period 09.09.2020–15.11.2022 and satellite-derived snow-covered area (SCA; weight = 5% per each of five elevation bands) for 26.02.2000–31.12.2022, both at daily temporal resolution. Satellite-derived snow-covered area is only available under cloud-free conditions. Overall, the model reproduces snow dynamics and streamflow variability well, with generally consistent performance across diagnostic plots. Performance metrics for the calibration period indicate good agreement between simulations and observations, with KGE′ = 0.83, correlation coefficient = 0.84, coefficient of variation ratio = 1.04, and model bias = 1.01.

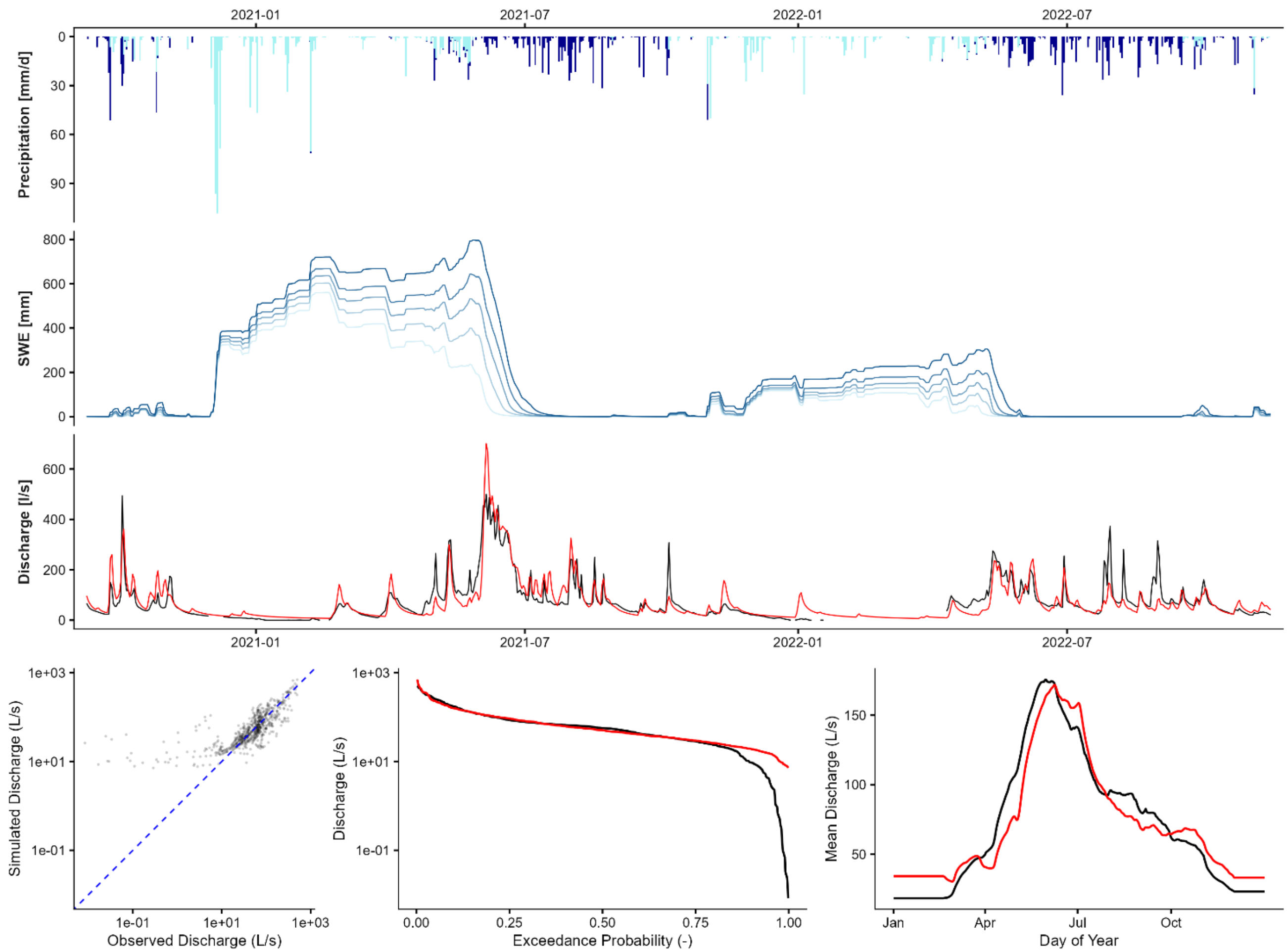

Supplementary Figure S18: Model results for the Ochsenhütte catchment (Reißeck Group). The figure shows the simulated hydrological response of the catchment, including the partitioning of catchment-average precipitation into snowfall and rainfall components. The temporal evolution of snow water equivalent (SWE) is presented as the catchment-wide median together with five elevation-band–resolved model time series. Simulated discharge is evaluated against observed discharge to assess the model's ability to reproduce runoff dynamics. Diagnostic panels include (i) a scatterplot of observed versus simulated discharge with a 1:1 reference line, (ii) flow duration curves comparing observed and simulated discharge across the full range of hydrological conditions, and (iii) a 30-day rolling mean of observed and simulated discharge highlighting seasonal variability. Model calibration was based on daily discharge observations (weight = 75%) over the period 09.09.2020–15.11.2022 and satellite-derived snow-covered area (SCA; weight = 5% per each of five elevation bands) for 26.02.2000–31.12.2022, both at daily temporal resolution. Satellite-derived snow-covered area is only available under cloud-free conditions. Overall, the model reproduces snow dynamics and streamflow variability well, with consistent performance across diagnostics. Performance metrics for the calibration period indicate good agreement between simulations and observations, with KGE′ = 0.86, correlation coefficient = 0.87, coefficient of variation ratio = 1.03, and model bias = 1.01.

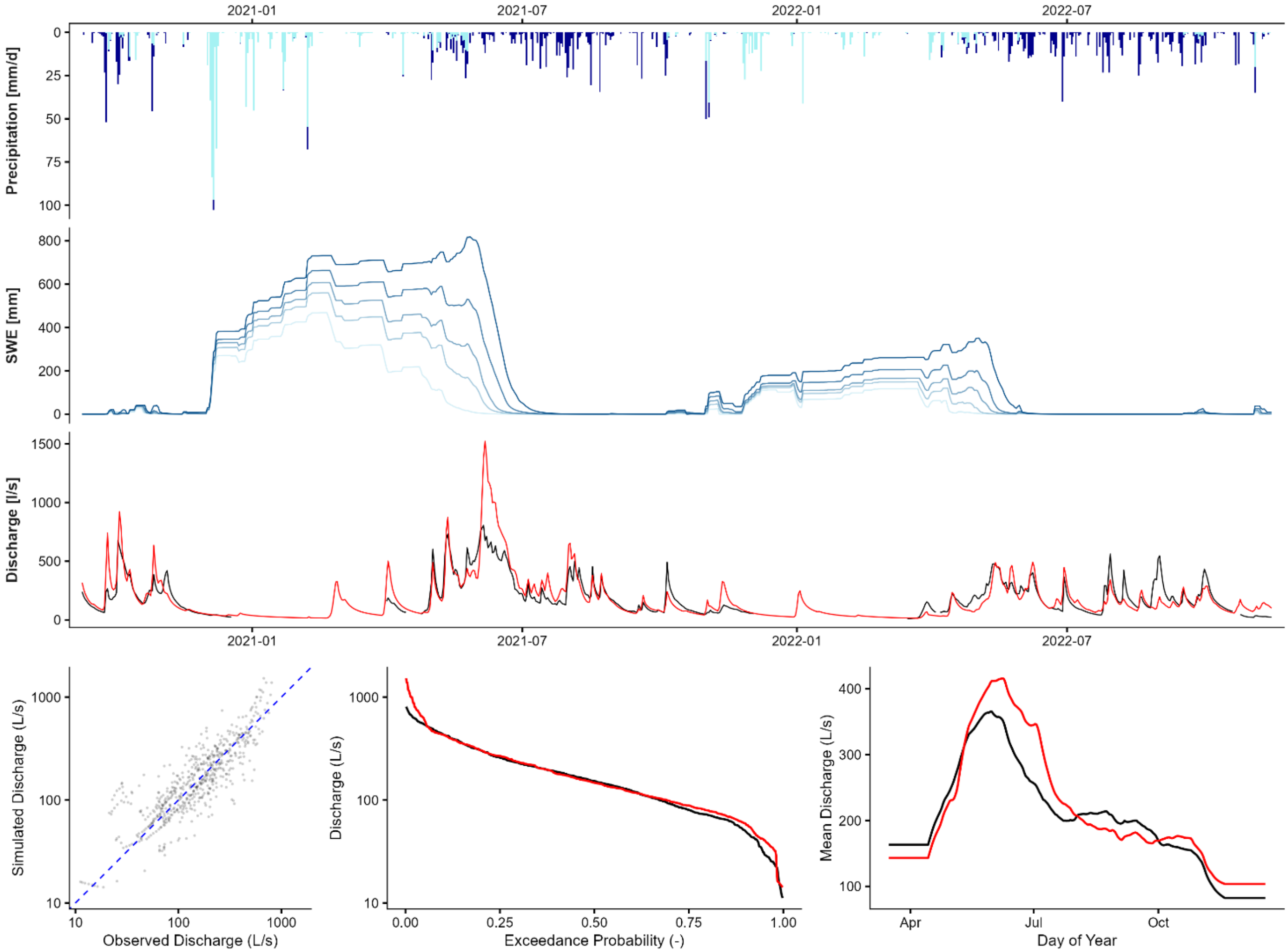

Supplementary Figure S19: Model results for the Ruppalm catchment (Reißeck Group). The figure presents the simulated hydrological response of the catchment, including the partitioning of catchment-average precipitation into snowfall and rainfall components. The temporal evolution of snow water equivalent (SWE) is shown as the catchment-wide median together with five elevation-band–resolved model time series. Simulated discharge is compared with observed discharge to evaluate the model's ability to reproduce runoff dynamics. Diagnostic panels include (i) a scatterplot of observed versus simulated discharge with a 1:1 reference line, (ii) flow duration curves comparing observed and simulated discharge across the full range of hydrological conditions, and (iii) a 30-day rolling mean of observed and simulated discharge highlighting seasonal variability. Model calibration was based on daily discharge observations (weight = 75%) over the period 09.09.2020–15.11.2022 and satellite-derived snow-covered area (SCA; weight = 5% per each of five elevation bands) for 26.02.2000–31.12.2022, both at daily temporal resolution. Satellite-derived snow-covered area is only available under cloud-free conditions. Overall, the model reproduces snow dynamics and streamflow variability well, with consistent performance across diagnostics. Performance metrics for the calibration period indicate good agreement between simulations and observations, with KGE′ = 0.86, correlation coefficient = 0.87, coefficient of variation ratio = 1.02, and model bias = 1.02.

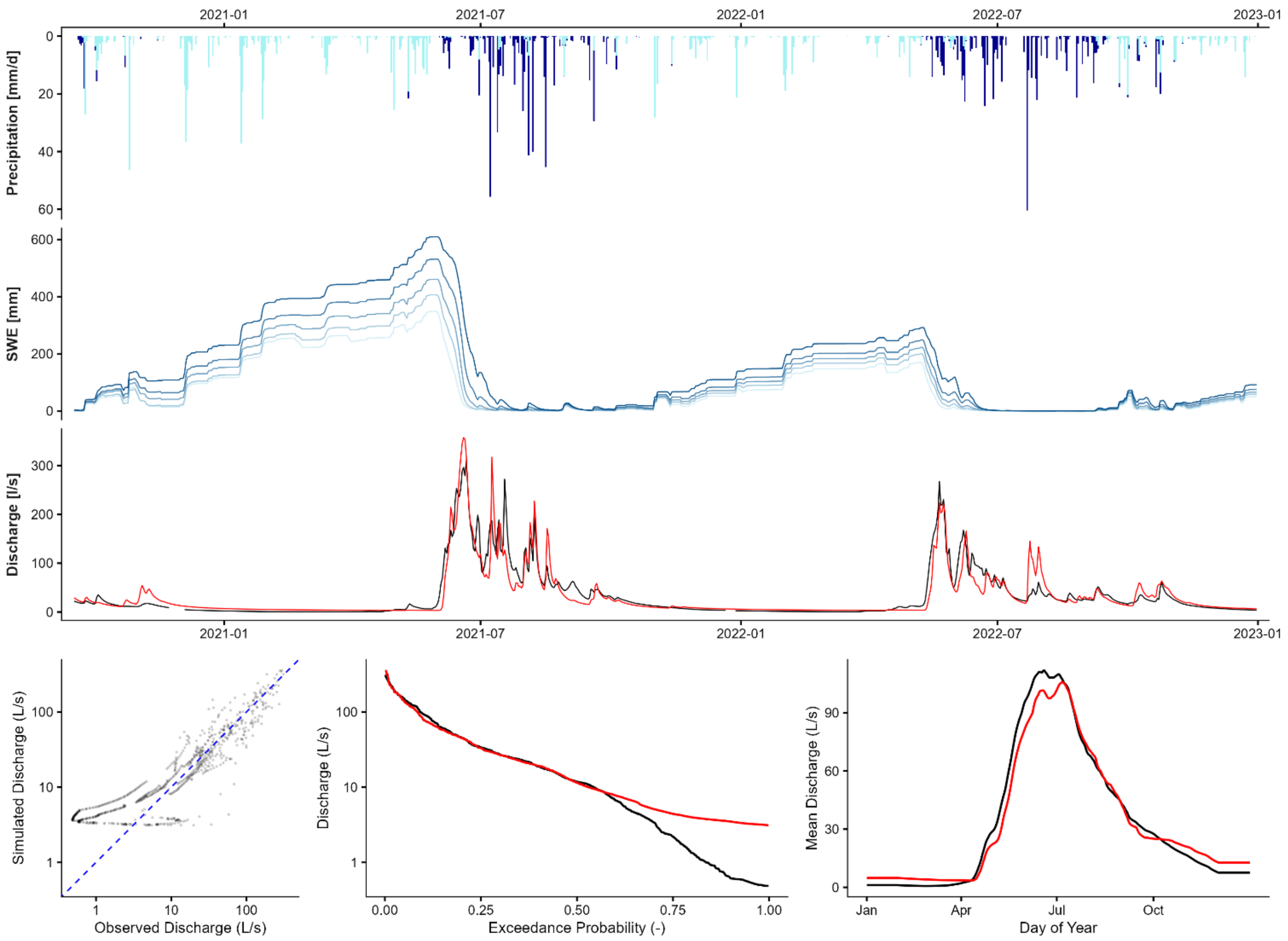

Supplementary Figure S20: Model results for the Arzkarquelle catchment (Ötztal Alps). The figure presents the simulated hydrological response of the catchment, including the partitioning of catchment-average precipitation into snowfall and rainfall components. The temporal evolution of snow water equivalent (SWE) is shown as the catchment-wide median together with five elevation-band–resolved model time series. Simulated discharge is compared with observed discharge to assess the model's ability to reproduce runoff dynamics. Diagnostic panels include (i) a scatterplot of observed versus simulated discharge with a 1:1 reference line, (ii) flow duration curves comparing observed and simulated discharge across the full range of hydrological conditions, and (iii) a 30-day rolling mean of observed and simulated discharge highlighting seasonal variability. Model calibration was based on daily discharge observations (weight = 75%) over the period 17.09.2020–31.12.2022 and satellite-derived snow-covered area (SCA; weight = 5% per each of five elevation bands) for 26.02.2000–30.12.2022, both at daily temporal resolution. Satellite-derived snow-covered area is only available under cloud-free conditions. Overall, the model reproduces snow dynamics and streamflow variability well, with particularly strong performance in capturing seasonal discharge patterns. Performance metrics for the calibration period indicate good agreement between simulations and observations, with KGE′ = 0.91, correlation coefficient = 0.92, coefficient of variation ratio = 1.00, and model bias = 1.02.

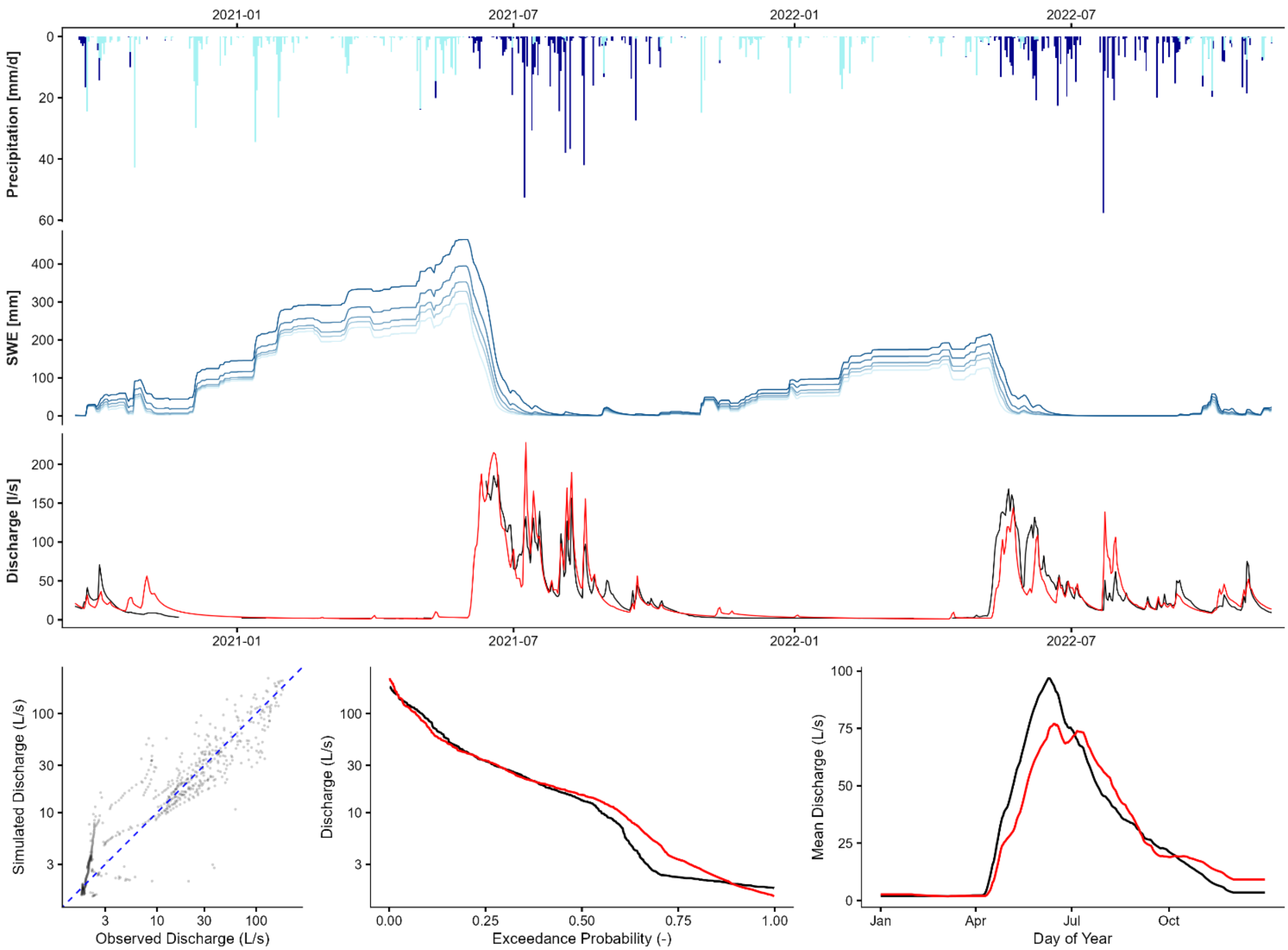

Supplementary Figure S21: Model results for the Vorderes Bergle catchment (Ötztal Alps). The figure presents the simulated hydrological response of the catchment, including the partitioning of catchment-average precipitation into snowfall and rainfall components. The temporal evolution of snow water equivalent (SWE) is shown as the catchment-wide median together with five elevation-band–resolved model time series. Simulated discharge is compared against observed discharge to evaluate the model's ability to reproduce runoff dynamics. Diagnostic panels include (i) a scatterplot of observed versus simulated discharge with a 1:1 reference line, (ii) flow duration curves comparing observed and simulated discharge across the full range of hydrological conditions, and (iii) a 30-day rolling mean of observed and simulated discharge highlighting seasonal variability. Model calibration was based on daily discharge observations (weight = 75%) over the period 17.09.2020–09.11.2022 and satellite-derived snow-covered area (SCA; weight = 5% per each of five elevation bands) for 25.02.2000–29.12.2022, both at daily temporal resolution. Satellite-derived snow-covered area is only available under cloud-free conditions. Overall, the model reproduces snow dynamics and streamflow variability well, with particularly consistent agreement in seasonal behavior. Performance metrics for the calibration period indicate strong agreement between simulations and observations, with KGE′ = 0.89, correlation coefficient = 0.90, coefficient of variation ratio = 1.00, and model bias = 1.01.

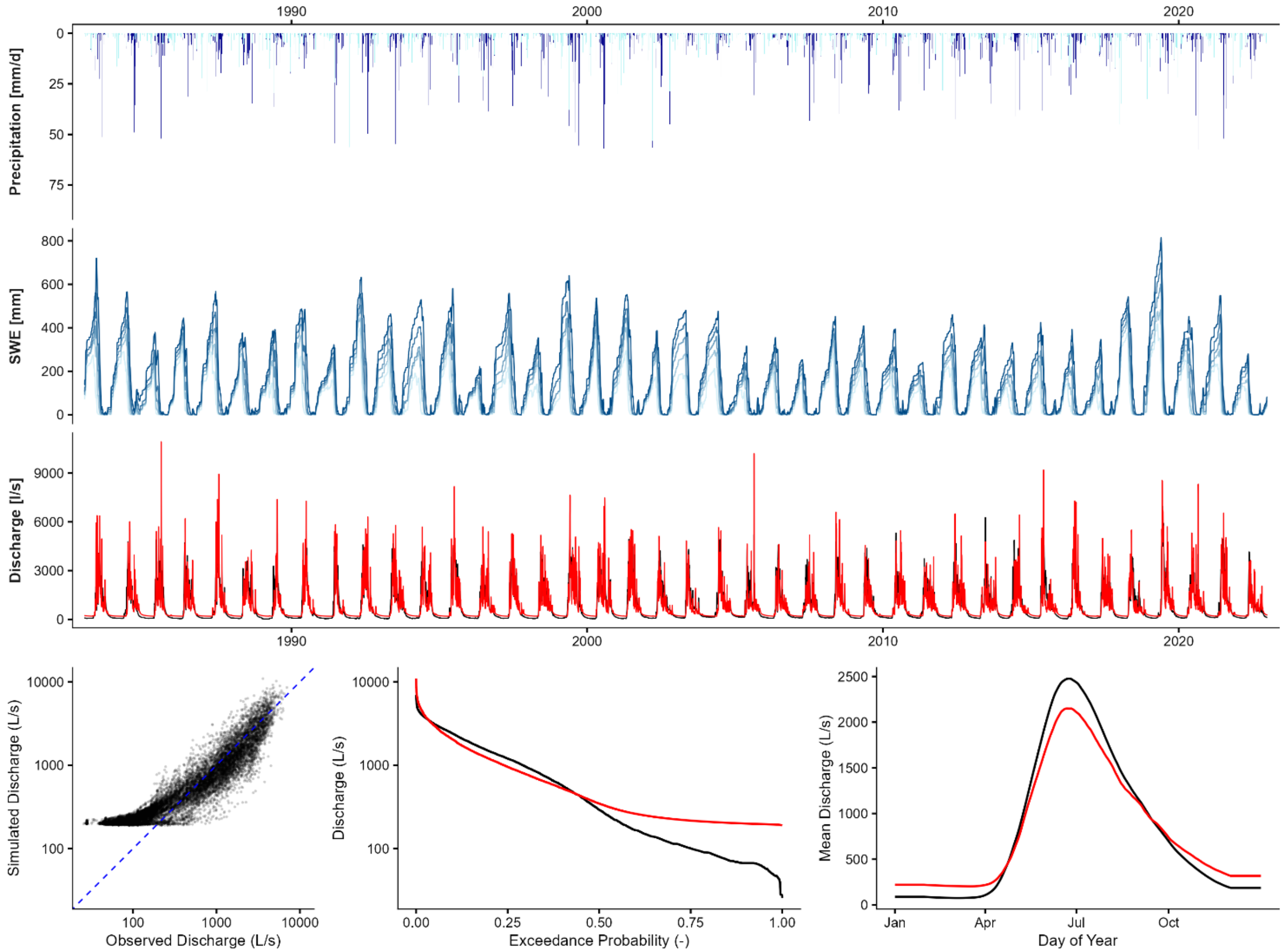

Supplementary Figure S22: Model results for the Radurschlalpe catchment (Ötztal Alps). The figure illustrates the simulated hydrological response of the catchment, including the partitioning of catchment-average precipitation into snowfall and rainfall components. The temporal evolution of snow water equivalent (SWE) is shown as the catchment-wide median together with five elevation-band–resolved model time series. Simulated discharge is compared against observed discharge to evaluate the model's ability to reproduce runoff dynamics. Diagnostic panels include (i) a scatterplot of observed versus simulated discharge with a 1:1 reference line, (ii) flow duration curves comparing observed and simulated discharge across the full range of hydrological conditions, and (iii) a 30-day rolling mean of observed and simulated discharge highlighting seasonal variability. Model calibration was based on daily discharge observations (weight = 75%) over the period 01.01.1983–31.12.2022 and satellite-derived snow-covered area (SCA; weight = 5% per each of five elevation bands) for 25.02.2000–30.12.2022, both at daily temporal resolution. Satellite-derived snow-covered area is only available under cloud-free conditions. Overall, the model reproduces snow dynamics and streamflow variability well, with consistent long-term performance across the extended calibration period. Performance metrics indicate strong agreement between simulations and observations, with KGE′ = 0.89, correlation coefficient = 0.90, coefficient of variation ratio = 1.01, and model bias = 1.01.

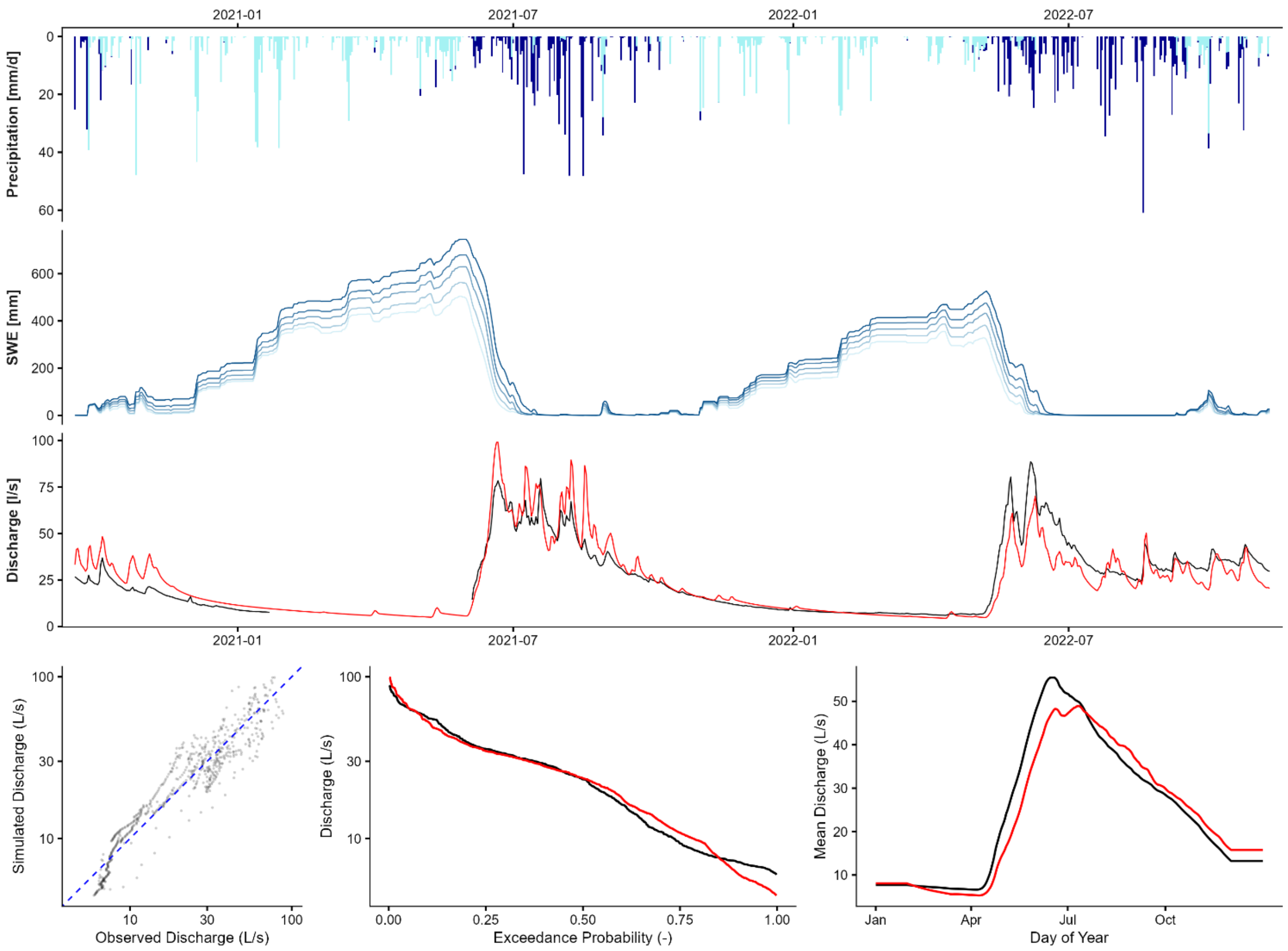

Supplementary Figure S23: Model results for the Rotbühelquelle catchment (Silvretta Alps). The figure presents simulated hydrological results for the catchment, including the partitioning of catchment-average precipitation into snowfall and rainfall components. The temporal evolution of snow water equivalent (SWE) is shown as the catchment-wide median together with five elevation-band–resolved model time series. Simulated discharge is compared against observed discharge to assess the model's ability to reproduce runoff dynamics. Diagnostic panels include (i) a scatterplot of observed versus simulated discharge with a 1:1 reference line, (ii) flow duration curves comparing observed and simulated discharge across the full range of hydrological conditions, and (iii) a 30-day rolling mean of observed and simulated discharge highlighting seasonal variability. Model calibration was based on daily discharge observations (weight = 75%) over the period 16.09.2020–10.11.2022 and satellite-derived snow-covered area (SCA; weight = 5% per each of five elevation bands) for 25.02.2000–22.09.2022, both at daily temporal resolution. Satellite-derived snow-covered area is only available under cloud-free conditions. Overall, the model reproduces snow dynamics and streamflow variability well, with consistent performance across diagnostics. Performance metrics for the calibration period indicate good agreement between simulations and observations, with KGE′ = 0.89, correlation coefficient = 0.90, coefficient of variation ratio = 1.01, and model bias = 1.02.

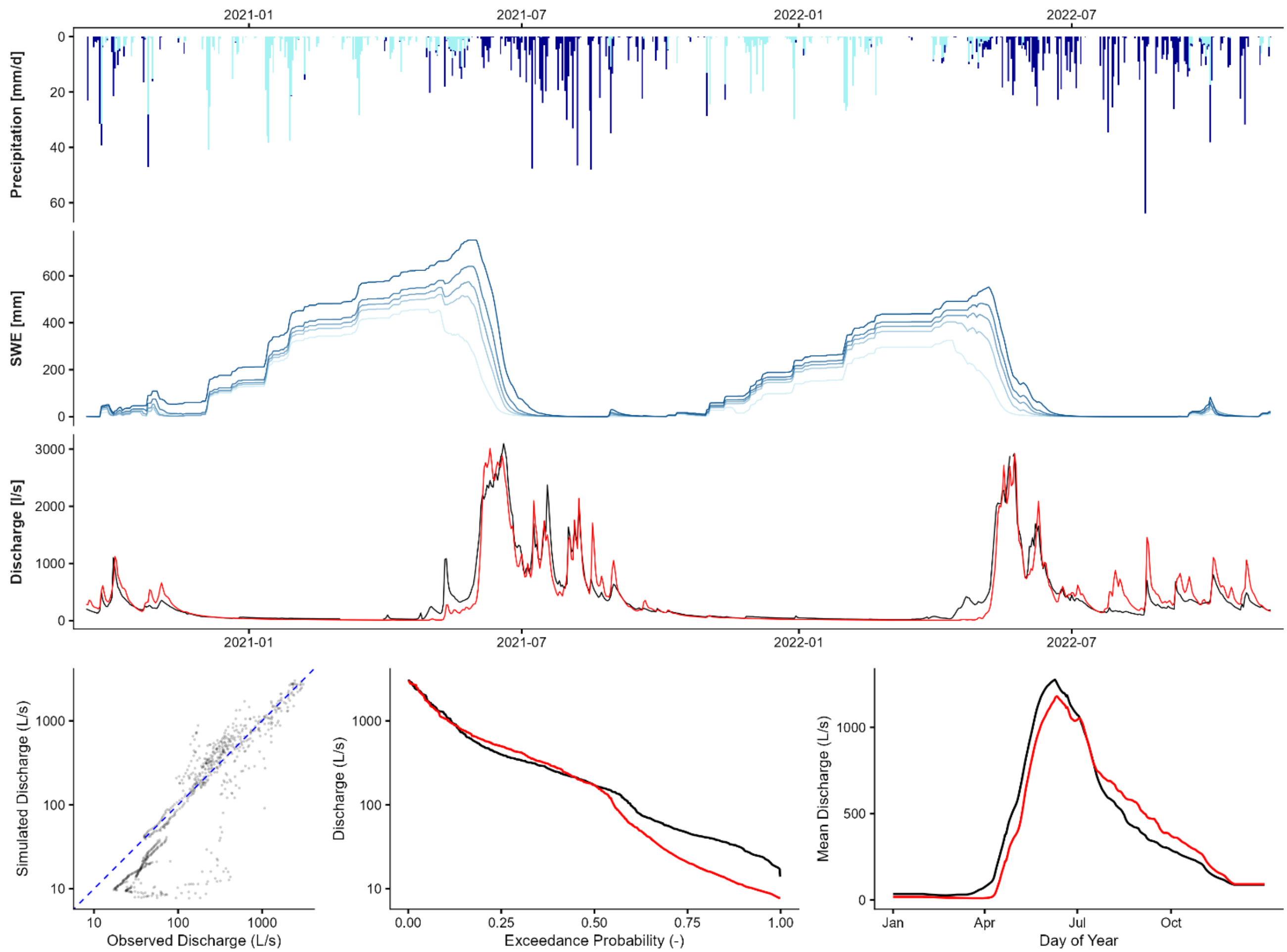

Supplementary Figure S24: Model results for the Vergaldaalpe catchment (Silvretta Alps). The figure presents simulated hydrological results for the catchment, including the partitioning of catchment-average precipitation into snowfall and rainfall components. The temporal evolution of snow water equivalent (SWE) is shown as the catchment-wide median together with five elevation-band–resolved model time series. Simulated discharge is compared against observed discharge to assess the model's ability to reproduce runoff dynamics. Diagnostic panels include (i) a scatterplot of observed versus simulated discharge with a 1:1 reference line, (ii) flow duration curves comparing observed and simulated discharge across the full range of hydrological conditions, and (iii) a 30-day rolling mean of observed and simulated discharge highlighting seasonal variability. Model calibration was based on daily discharge observations (weight = 75%) over the period 15.09.2020–10.11.2022 and satellite-derived snow-covered area (SCA; weight = 5% per each of five elevation bands) for 25.02.2000–23.09.2022, both at daily temporal resolution. Satellite-derived snow-covered area is only available under cloud-free conditions. Overall, the model reproduces snow dynamics and streamflow variability very well, with particularly strong agreement in seasonal behavior and high-flow conditions. Performance metrics for the calibration period indicate strong agreement between simulations and observations, with KGE′ = 0.93, correlation coefficient = 0.94, coefficient of variation ratio = 1.01, and model bias = 1.01.

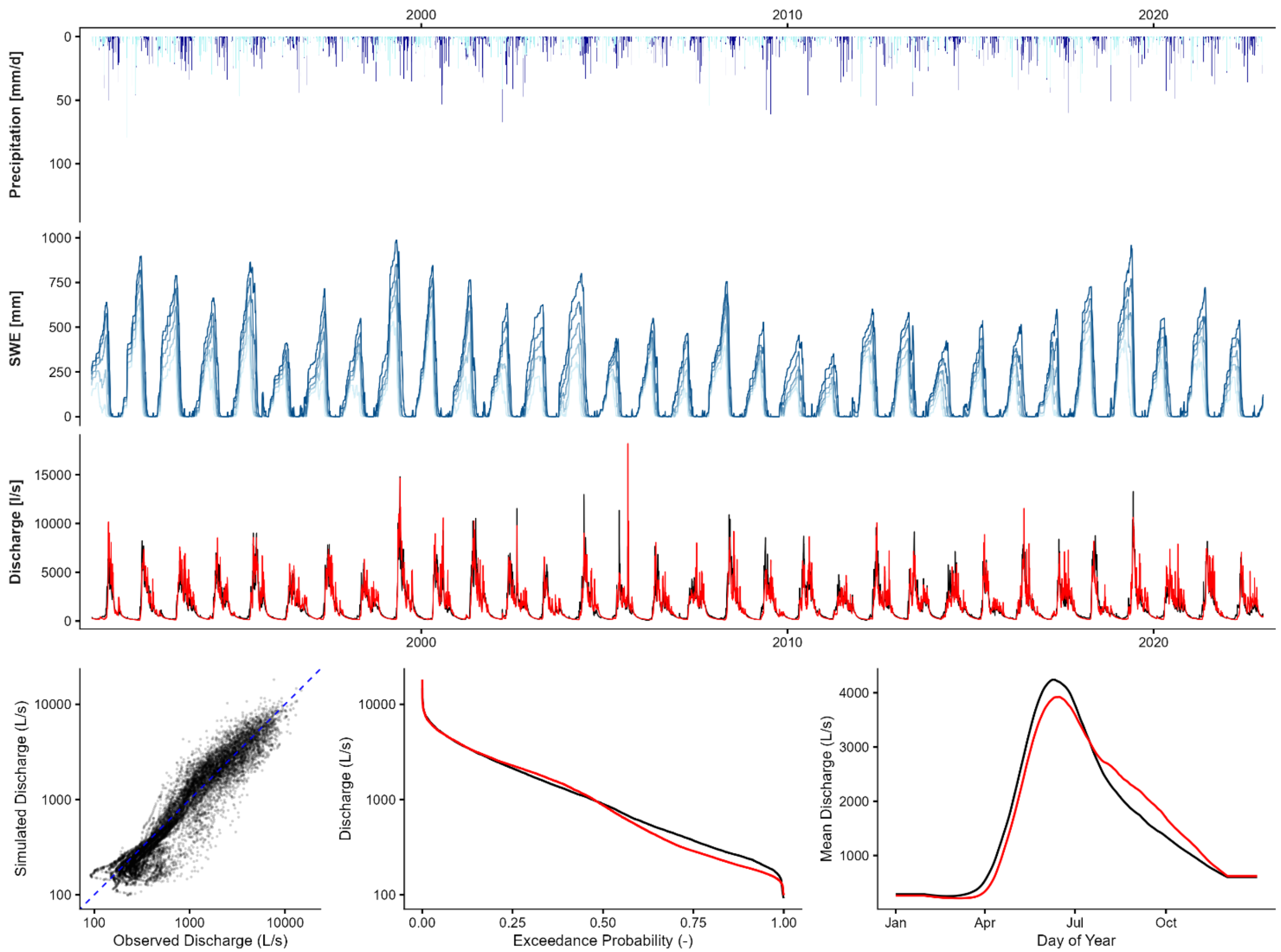

Supplementary Figure S25: Model results for the Gargellen catchment (Silvretta Alps). The figure presents simulated hydrological results for the catchment, including the partitioning of catchment-average precipitation into snowfall and rainfall components. The temporal evolution of snow water equivalent (SWE) is shown as the catchment-wide median together with five elevation-band–resolved model time series. Simulated discharge is compared against observed discharge to evaluate the model's ability to reproduce runoff dynamics. Diagnostic panels include (i) a scatterplot of observed versus simulated discharge with a 1:1 reference line, (ii) flow duration curves comparing observed and simulated discharge across the full range of hydrological conditions, and (iii) a 30-day rolling mean of observed and simulated discharge highlighting seasonal variability. Model calibration was based on daily discharge observations (weight = 75%) over the period 01.01.1991–31.12.2022 and satellite-derived snow-covered area (SCA; weight = 5% per each of five elevation bands) for 25.02.2000–23.09.2022, both at daily temporal resolution. Satellite-derived snow-covered area is only available under cloud-free conditions. Overall, the model reproduces snow dynamics and streamflow variability well, with consistent performance across long-term and seasonal dynamics. Performance metrics for the calibration period indicate strong agreement between simulations and observations, with KGE′ = 0.89, correlation coefficient = 0.91, coefficient of variation ratio = 1.02, and model bias = 1.02.

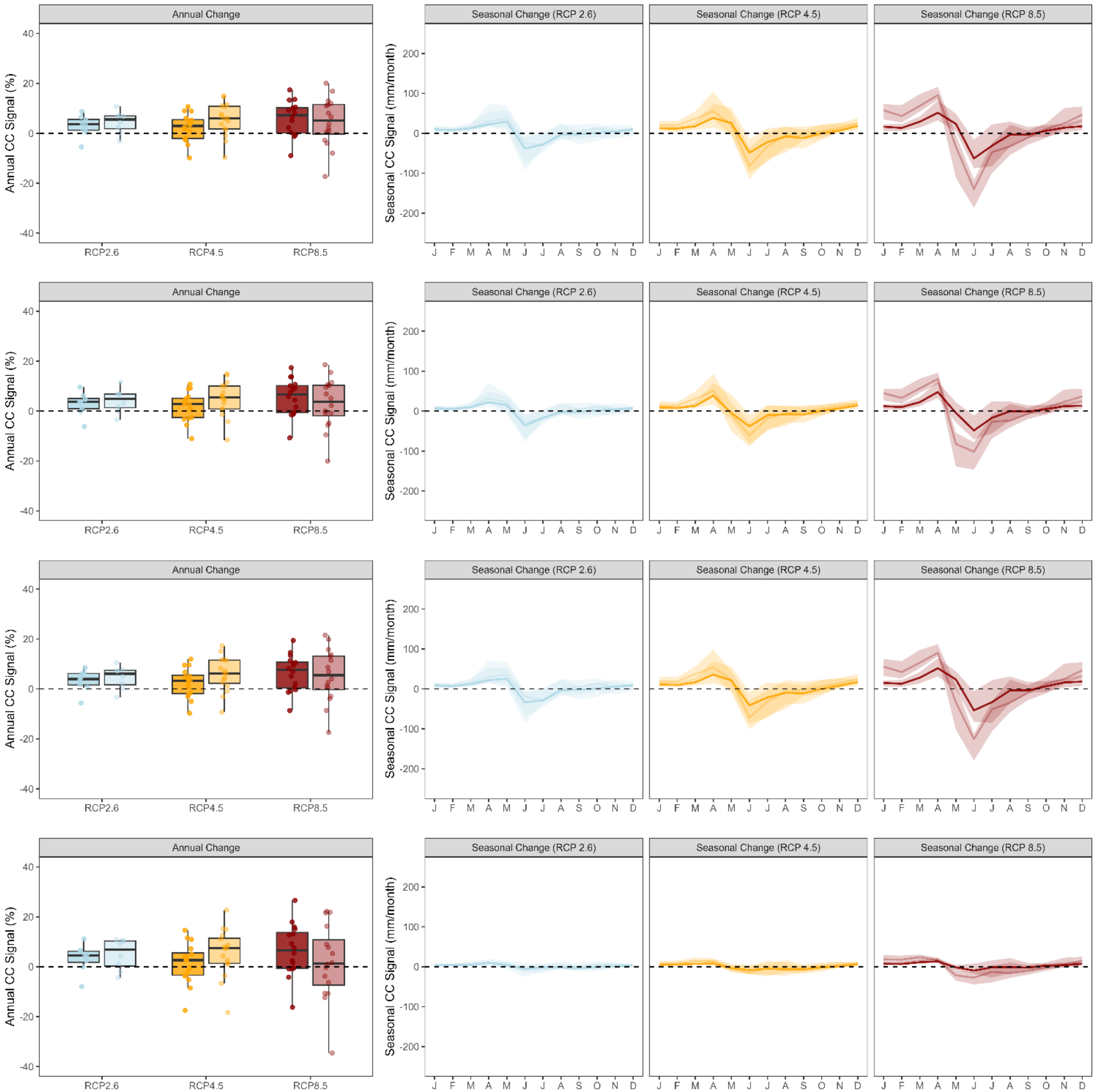

Supplementary Figure S26: Projected changes in runoff behavior in the Seckau Alps study area (a) at the Kettentörlquelle gauging station, (b) at the Kettentörlbach gauging station, (c) within the rock glacier catchments of the study area, (d) at the Hammerjäger gauging station. Changes are shown relative to the historical reference period (1980–2009) for the near-future (2030–2059; saturated colors) and far-future (2070–2099; faded colors) horizons, by emission scenario: RCP2.6 (blue), RCP4.5 (orange), RCP8.5 (red). Boxplots indicate annual discharge changes (relative, left panels), while seasonal changes (mm/month, right panels) show ensemble medians as lines and projection uncertainty as shaded areas.

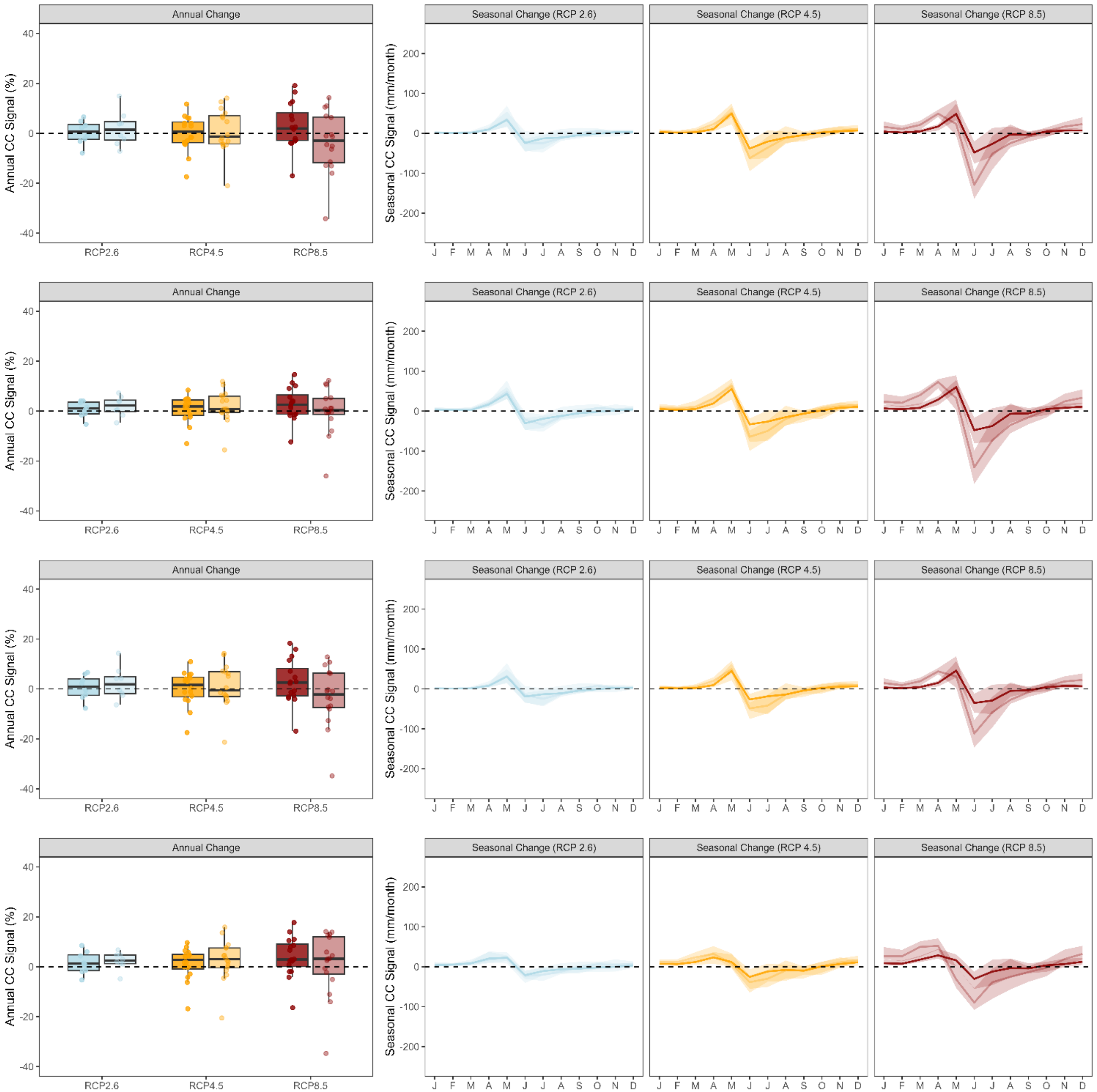

Supplementary Figure S27: Projected changes in runoff behavior in the Radstadt Alps study area (a) at the Lantschfeldquelle gauging station, (b) at the Postalm gauging station, (c) within the rock glacier catchments of the study area, (d) at the Mauterndorf gauging station, characterized by karst aquifers and valley-filling sediments. Changes are shown relative to the historical reference period (1980–2009) for the near-future (2030–2059; saturated colors) and far-future (2070–2099; faded colors) horizons, by emission scenario: RCP2.6 (blue), RCP4.5 (orange), RCP8.5 (red). Boxplots indicate annual discharge changes (relative, left panels), while seasonal changes (mm/month, right panels) show ensemble medians as lines and projection uncertainty as shaded areas.

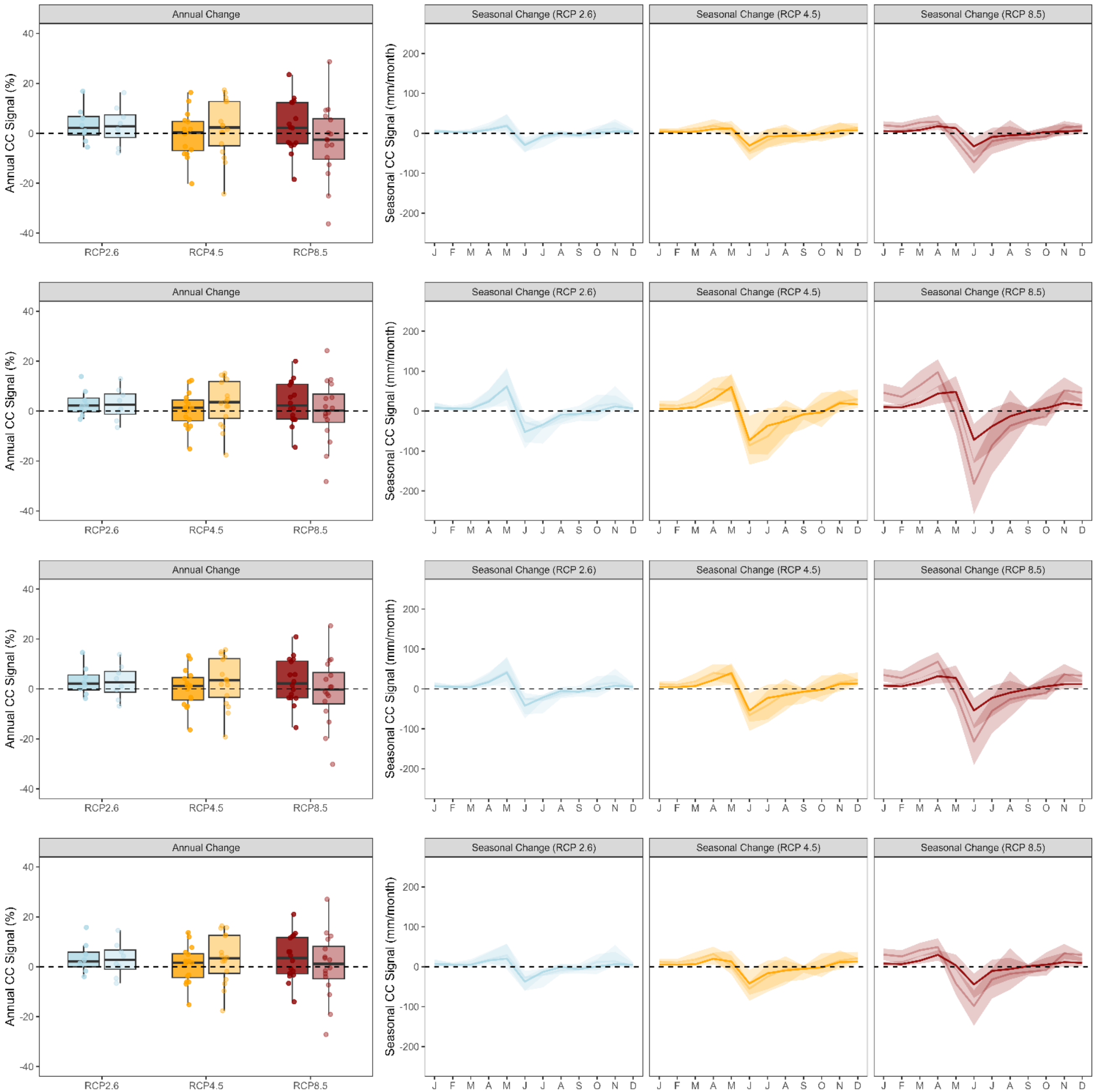

Supplementary Figure S28: Projected changes in runoff behavior in the Reißeck group study area (a) at the Buchleitenquelle gauging station, (b) at the Ochsenhütte gauging station, (c) within the rock glacier catchments of the study area, (d) at the Ruppalm gauging station. Changes are shown relative to the historical reference period (1980–2009) for the near-future (2030–2059; saturated colors) and far-future (2070–2099; faded colors) horizons, by emission scenario: RCP2.6 (blue), RCP4.5 (orange), RCP8.5 (red). Boxplots indicate annual discharge changes (relative, left panels), while seasonal changes (mm/month, right panels) show ensemble medians as lines and projection uncertainty as shaded areas.

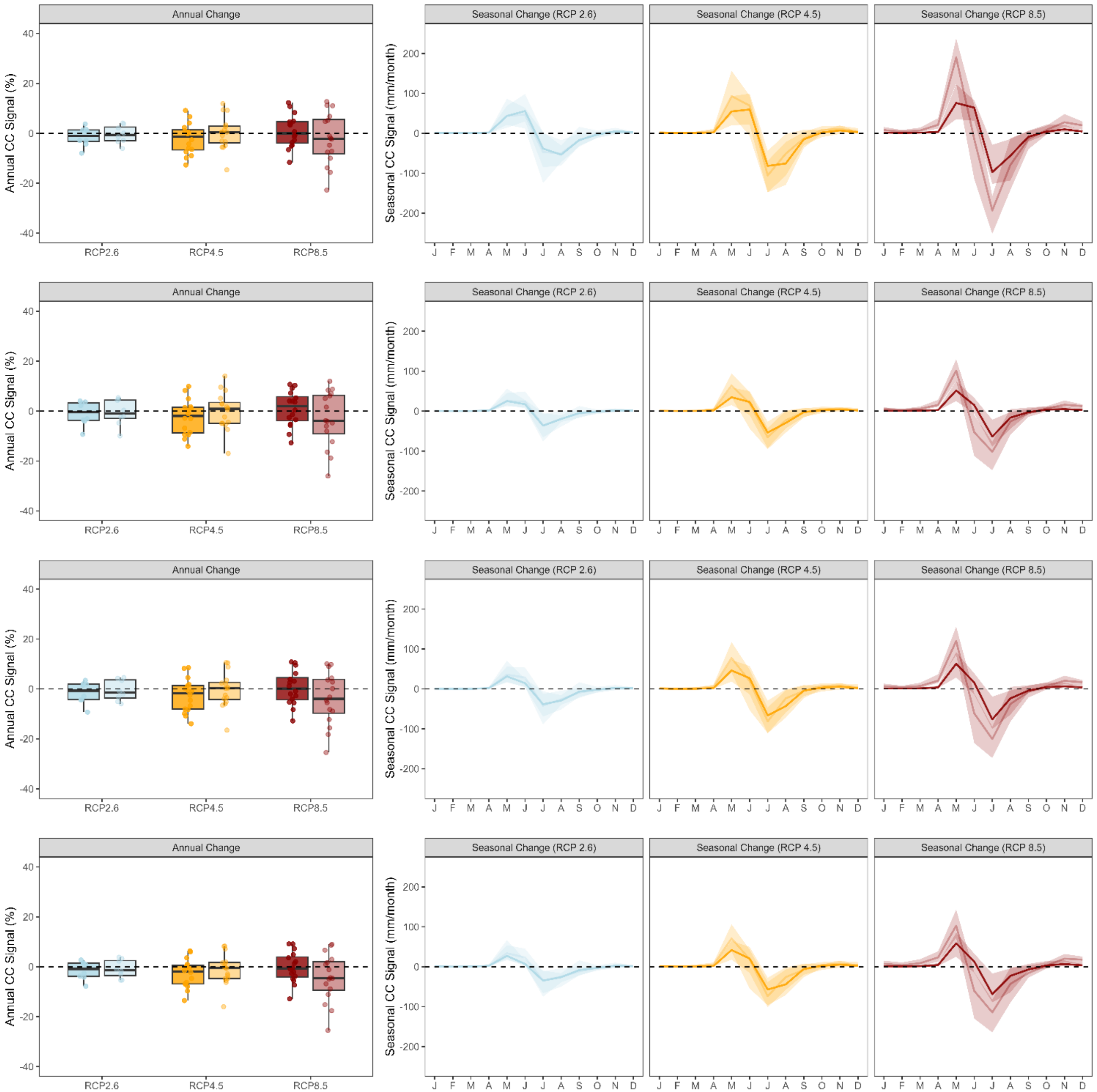

Supplementary Figure S29: Projected changes in runoff behavior in the Ötztal Alps study area (a) at the Arzkarquelle gauging station, (b) at the Vorderes Bergle gauging station, (c) within the rock glacier catchments of the study area, (d) at the Radurschlalpe gauging station. Changes are shown relative to the historical reference period (1980–2009) for the near-future (2030–2059; saturated colors) and far-future (2070–2099; faded colors) horizons, by emission scenario: RCP2.6 (blue), RCP4.5 (orange), RCP8.5 (red). Boxplots indicate annual discharge changes (relative, left panels), while seasonal changes (mm/month, right panels) show ensemble medians as lines and projection uncertainty as shaded areas.

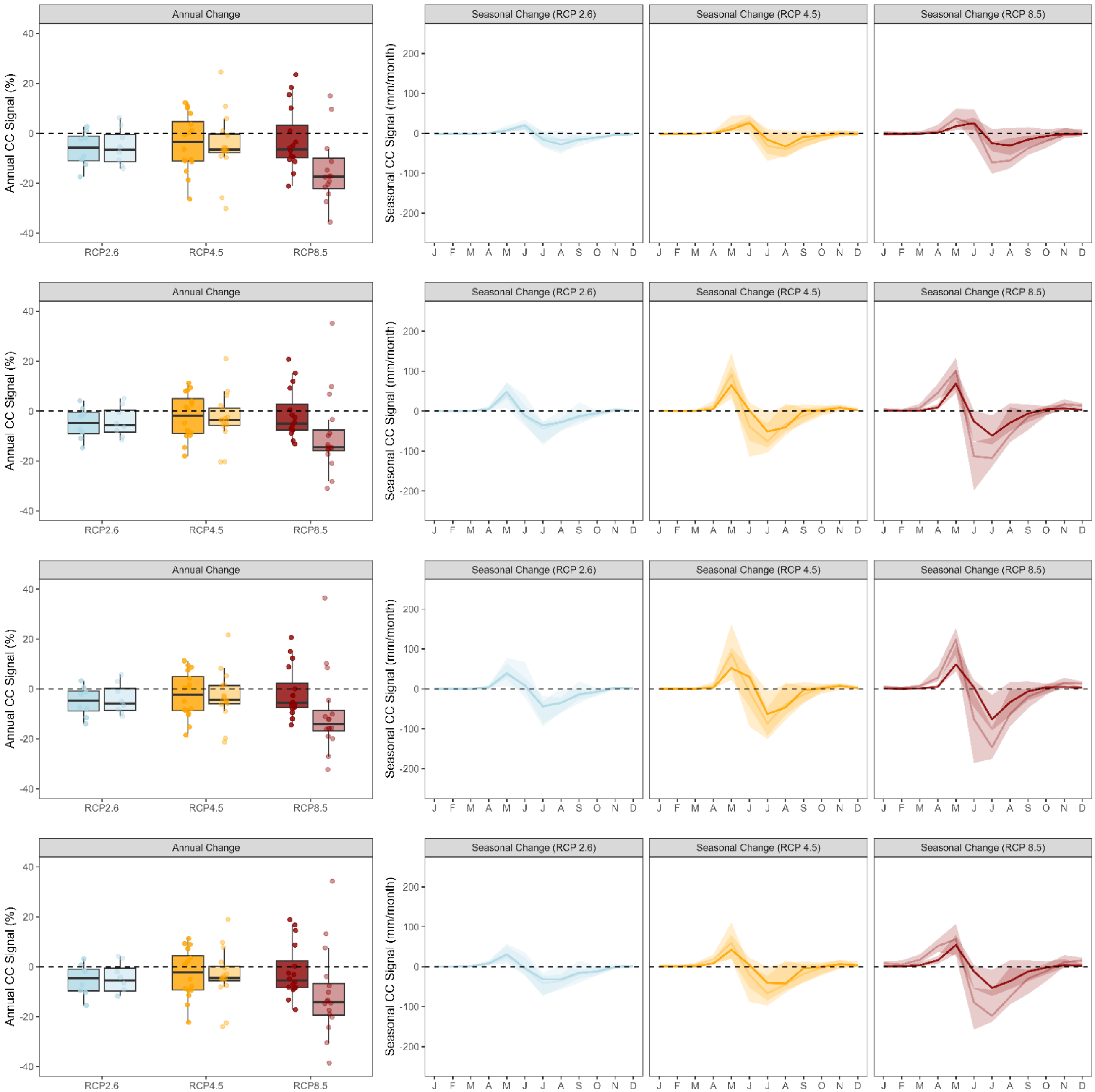

Supplementary Figure S30: Projected changes in runoff behavior in the Silvretta Alps study area (a) at the Rotbühelquelle gauging station, (b) at the Vergaldaalpe gauging station, (c) within the rock glacier catchments of the study area, (d) at the Gargellen gauging station, whose catchment is partly characterized by karst aquifers in the western parts. Changes are shown relative to the historical reference period (1980–2009) for the near-future (2030–2059; saturated colors) and far-future (2070–2099; faded colors) horizons, by emission scenario: RCP2.6 (blue), RCP4.5 (orange), RCP8.5 (red). Boxplots indicate annual discharge changes (relative, left panels), while seasonal changes (mm/month, right panels) show ensemble medians as lines and projection uncertainty as shaded areas.

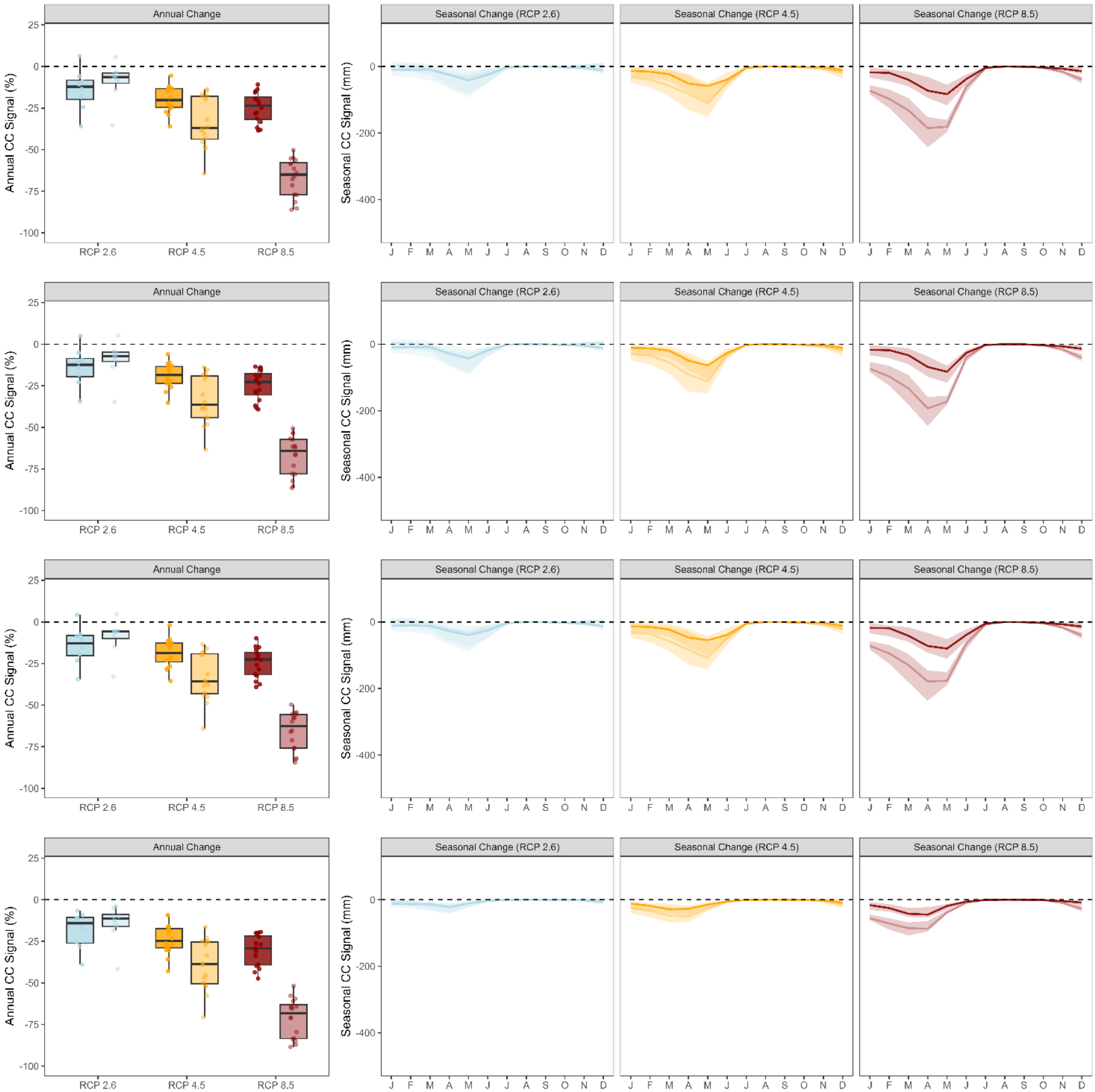

Supplementary Figure S31: Projected changes in snow water equivalent (SWE) of snow cover in the Seckau Alps study area (a) within the Kettentörlquelle catchment, (b) within the Kettentörlbach catchment, (c) within the rock glacier catchments of the study area, (d) within the entire Seckau Alps study area. Changes are shown relative to the historical reference period (1980–2009) for the near-future (2030–2059; saturated colors) and far-future (2070–2099; faded colors) horizons, by emission scenario (RCP2.6, RCP4.5, RCP8.5). Boxplots indicate annual SWE changes (relative, left panels), while seasonal changes (mm, right panels) show ensemble medians as lines and projection uncertainty as shaded areas.

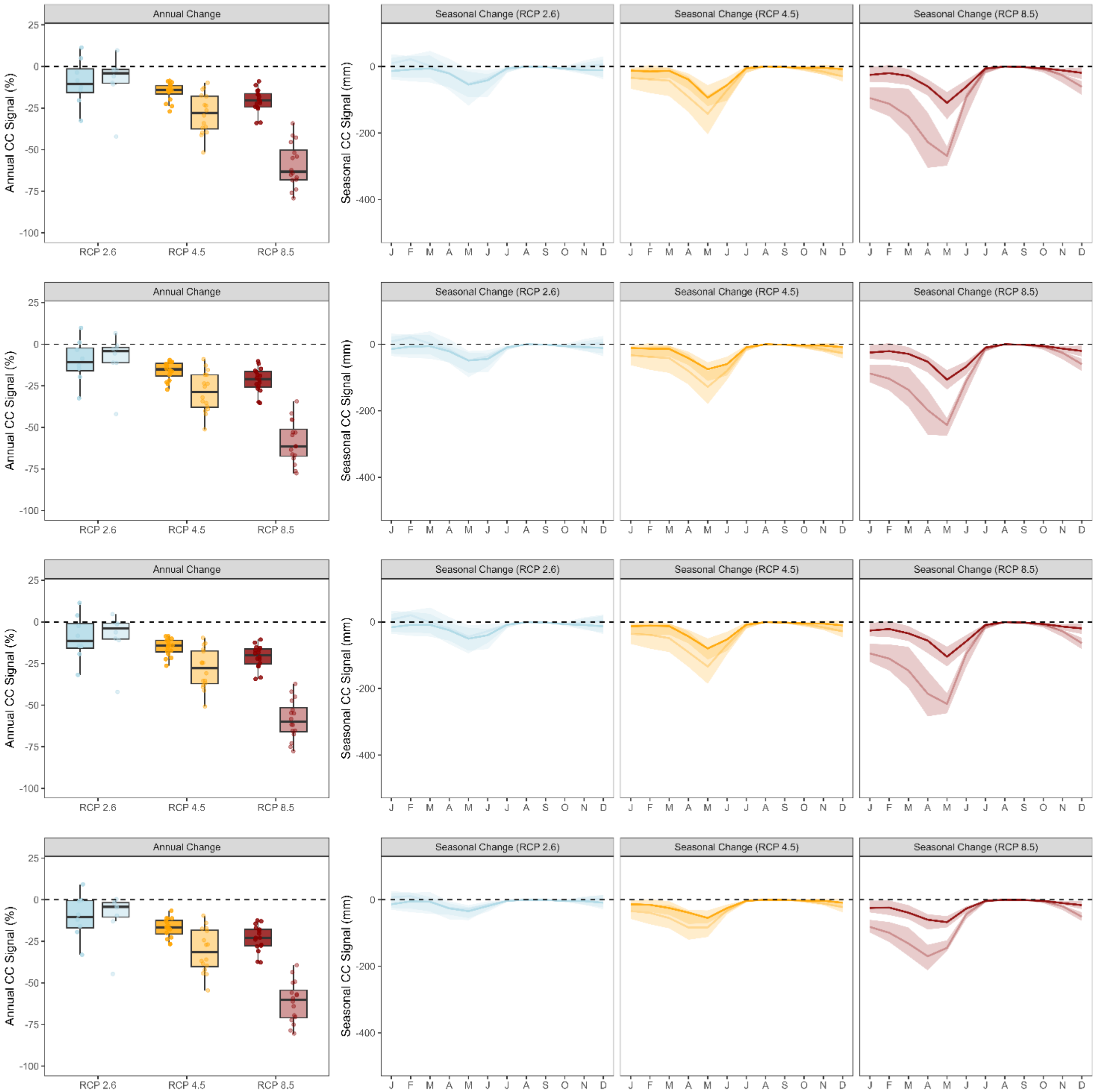

Supplementary Figure S32: Projected changes in snow water equivalent (SWE) of snow cover in the Radstadt Alps study area (a) within the Lantschfeldquelle catchment, (b) within the Postalm catchment, (c) within the rock glacier catchments of the study area, (d) within the entire Radstadt Alps study area. Changes are shown relative to the historical reference period (1980–2009) for the near-future (2030–2059; saturated colors) and far-future (2070–2099; faded colors) horizons, by emission scenario (RCP2.6, RCP4.5, RCP8.5). Boxplots indicate annual SWE changes (relative, left panels), while seasonal changes (mm, right panels) show ensemble medians as lines and projection uncertainty as shaded areas.

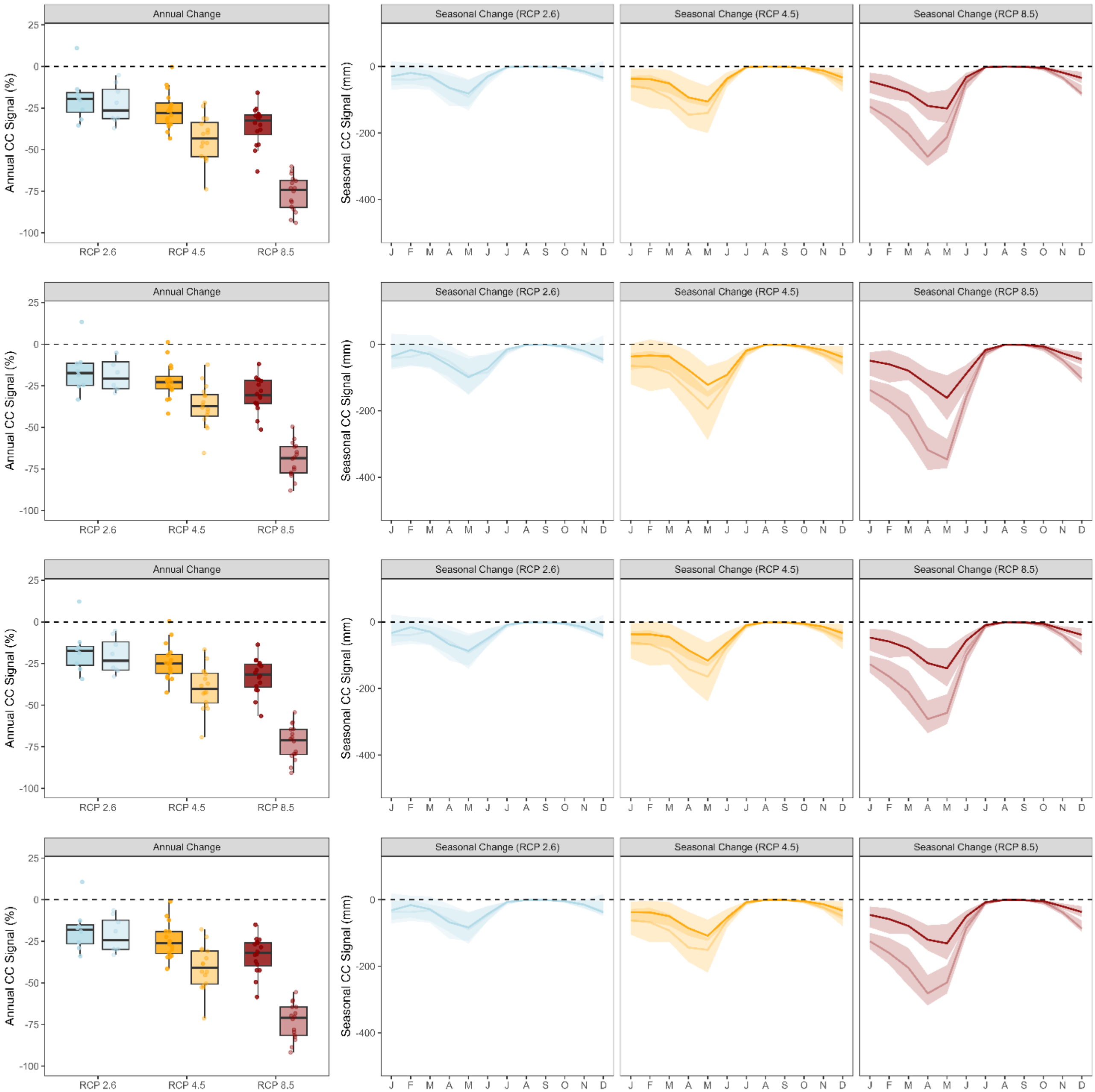

Supplementary Figure S33: Projected changes in snow water equivalent (SWE) of snow cover in the Reißeck Group study area (a) within the Buchleiten catchment, (b) within the Ochsenhütte catchment, (c) within the rock glacier catchments of the study area, (d) within the entire Reißeck Group study area. Changes are shown relative to the historical reference period (1980–2009) for the near-future (2030–2059; saturated colors) and far-future (2070–2099; faded colors) horizons, by emission scenario (RCP2.6, RCP4.5, RCP8.5). Boxplots indicate annual SWE changes (relative, left panels), while seasonal changes (mm, right panels) show ensemble medians as lines and projection uncertainty as shaded areas.

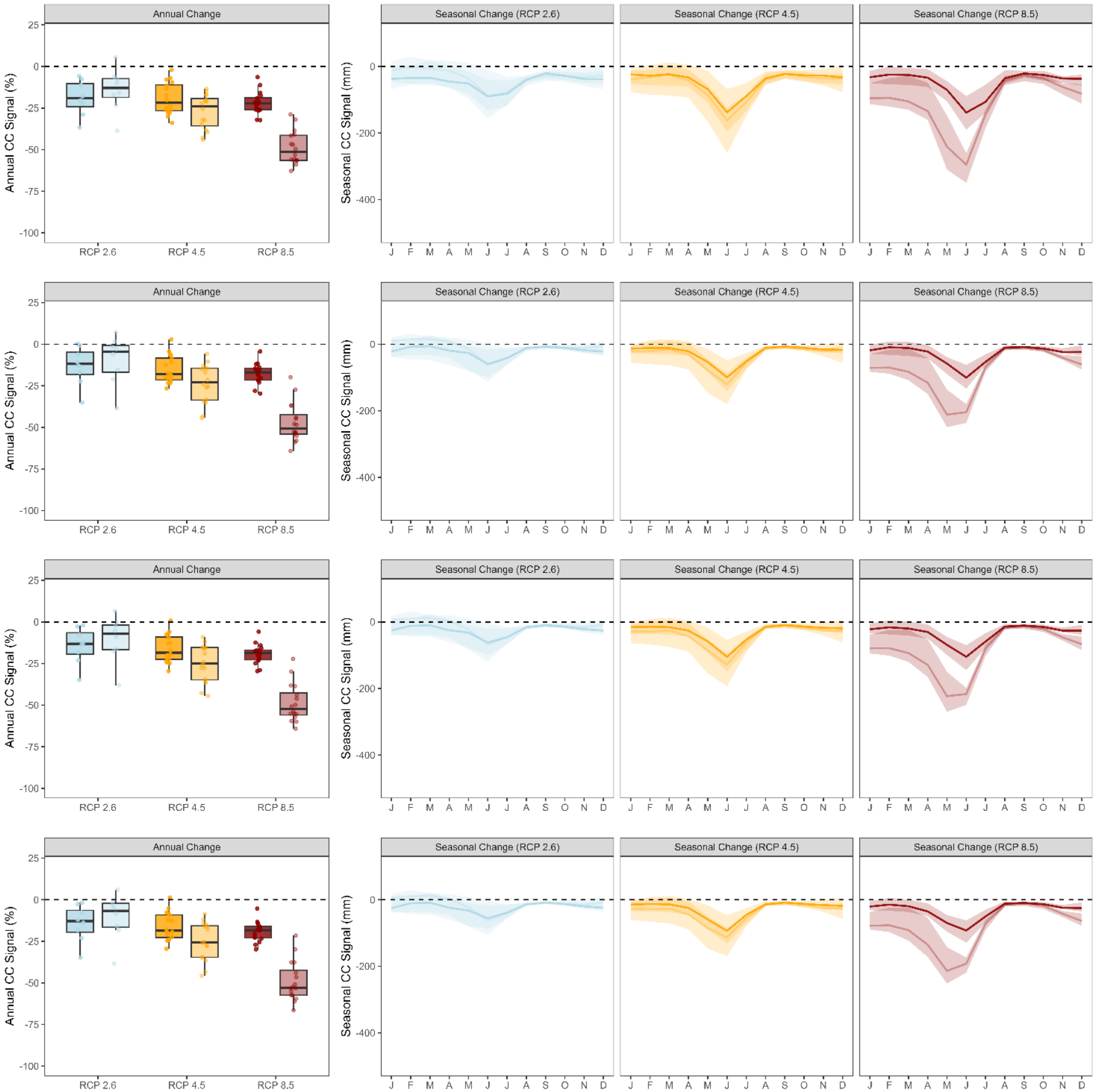

Supplementary Figure S34: Projected changes in snow water equivalent (SWE) of snow cover in the Ötztal Alps study area (a) within the Arzkarquelle catchment, (b) within the Vorderes Bergle catchment, (c) within the rock glacier catchments of the study area, (d) within the entire Ötztal Alps study area. Changes are shown relative to the historical reference period (1980–2009) for the near-future (2030–2059; saturated colors) and far-future (2070–2099; faded colors) horizons, by emission scenario (RCP2.6, RCP4.5, RCP8.5). Boxplots indicate annual SWE changes (relative, left panels), while seasonal changes (mm, right panels) show ensemble medians as lines and projection uncertainty as shaded areas.

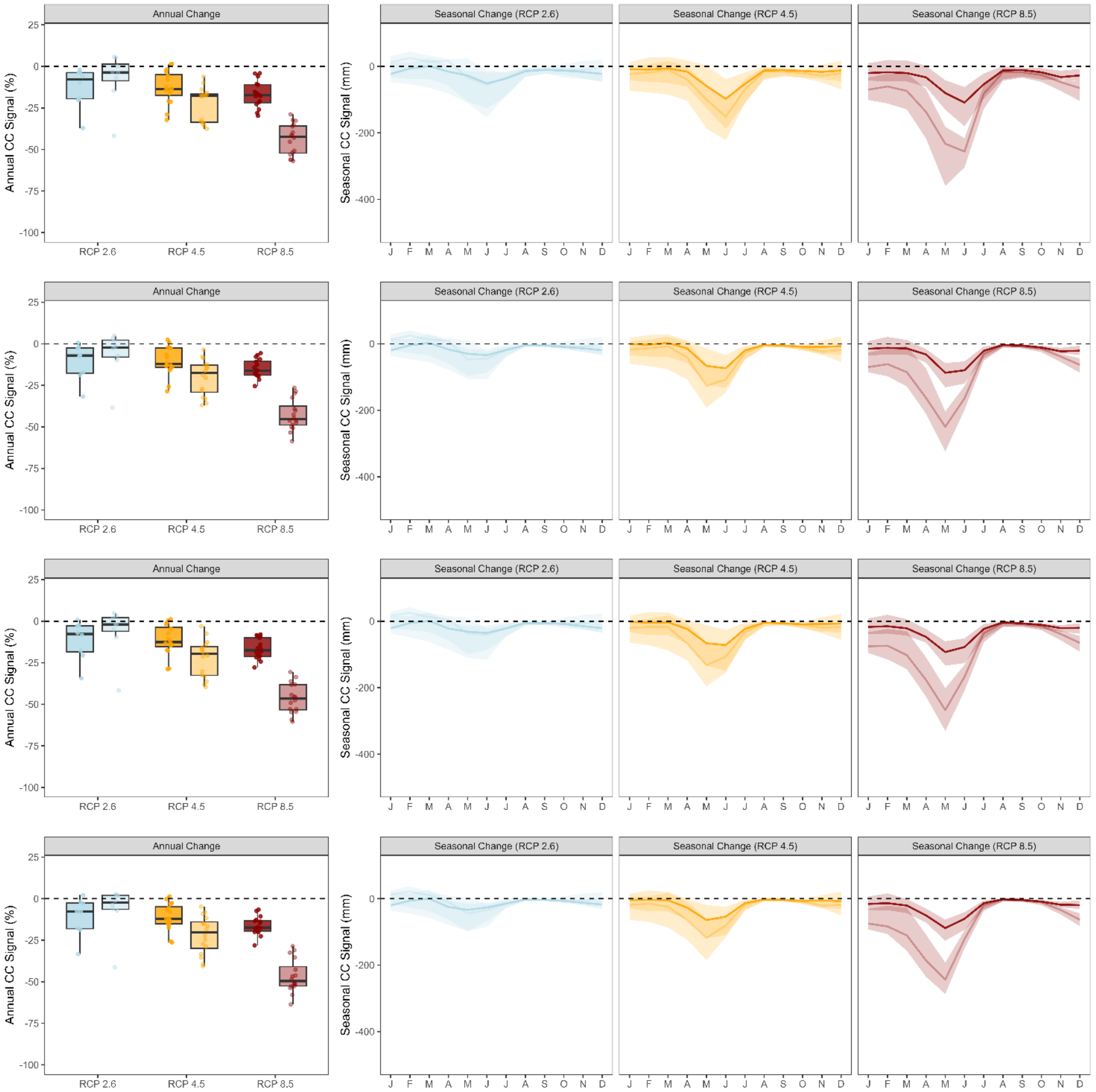

Supplementary Figure S35: Projected changes in snow water equivalent (SWE) of snow cover in the Silvretta Alps study area (a) within the Rotbühelquelle catchment, (b) within the Vergaldaalpe catchment, (c) within the rock glacier catchments of the study area, (d) within the entire Silvretta Alps study area. Changes are shown relative to the historical reference period (1980–2009) for the near-future (2030–2059; saturated colors) and far-future (2070–2099; faded colors) horizons, by emission scenario (RCP2.6, RCP4.5, RCP8.5). Boxplots indicate annual SWE changes (relative, left panels), while seasonal changes (mm, right panels) show ensemble medians as lines and projection uncertainty as shaded areas.

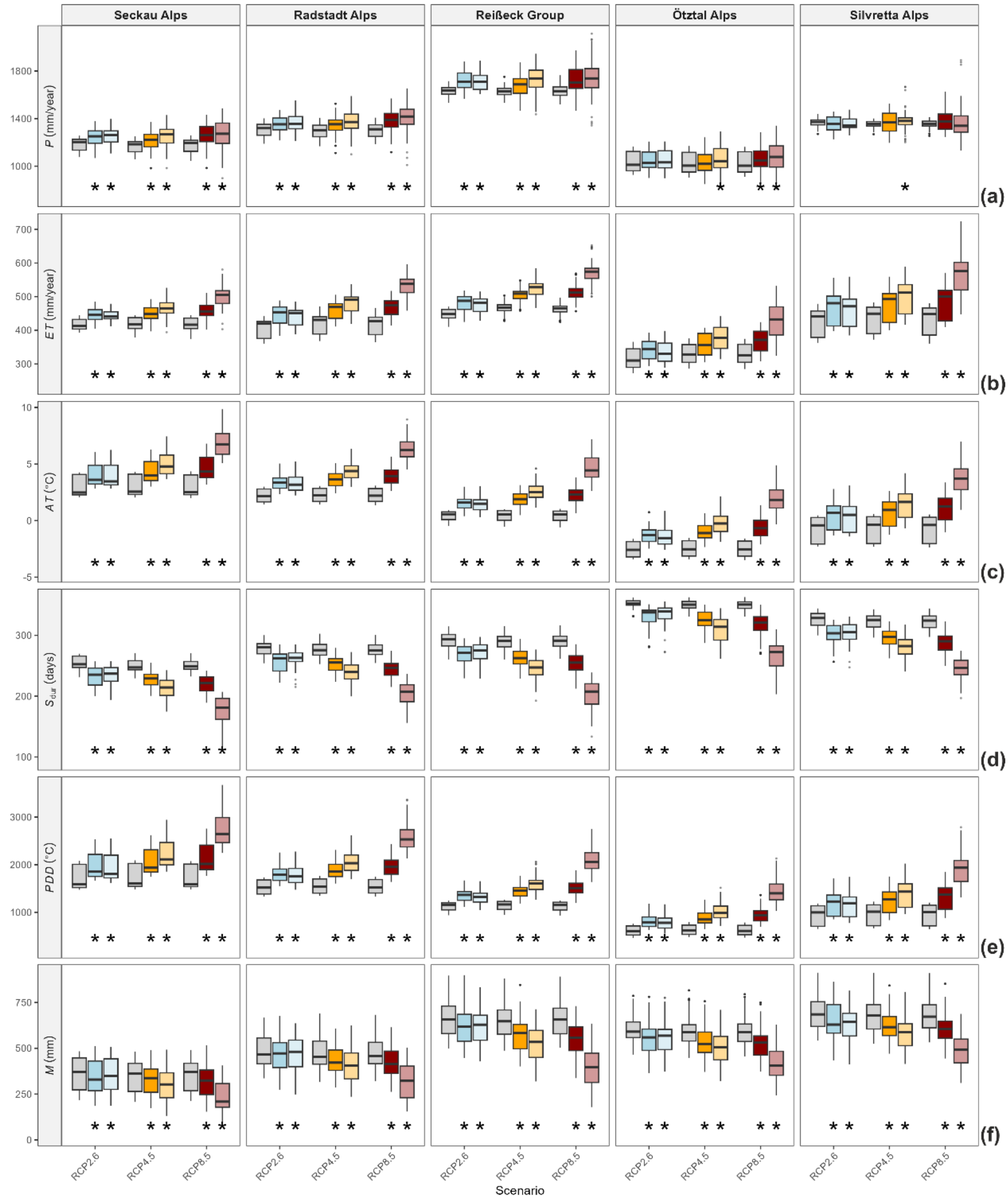

Supplementary Figure S36: Changes in snow dynamics and atmospheric drivers across the five study sites, quantified by annual precipitation (*P*), actual evapotranspiration (*ET*), mean air temperature (*AT*), snow cover duration (S_{dur}), positive degree-day sum (*PDD*), and snowmelt volume (*M*). Boxplots illustrate the ensemble spread for the historical reference period (1980–2009; grey), and the projected shifts for the near-future (2030–2059; saturated colors) and far-future (2070–2099; transparent colors) periods. Results are disaggregated by emission scenario: RCP2.6 (blue), RCP4.5 (orange), and RCP8.5 (red). Asterisks below the boxplots denote statistically significant differences between the future period and the historical reference at the α=0.05 level, determined by the rank-sum test.

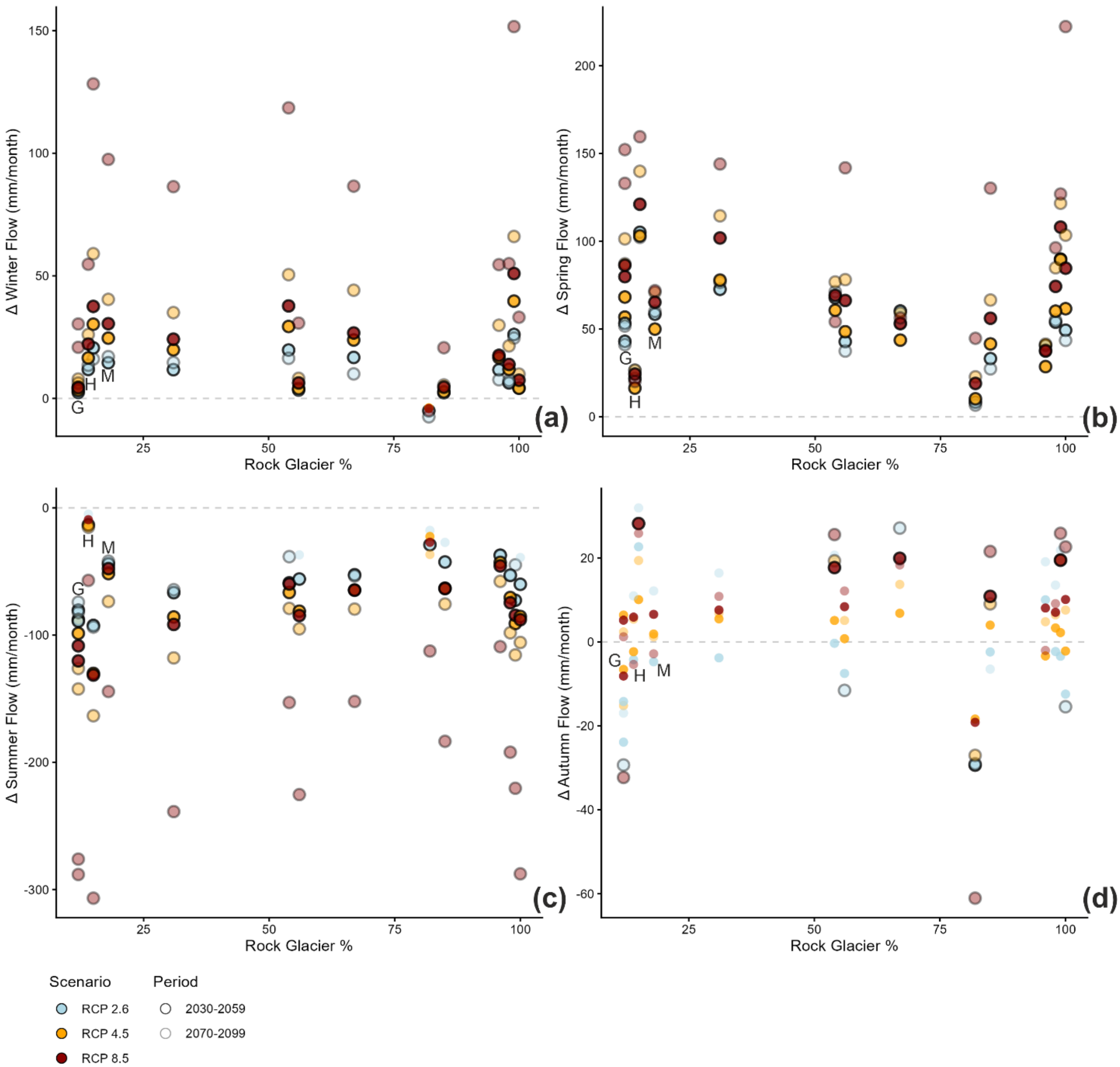

Supplementary Figure S37: Relationship between projected seasonal discharge changes and catchment-scale rock glacier coverage. Panels show absolute changes in mean seasonal runoff for (a) winter (DJF), (b) spring (MAM), (c) summer (JJA), and (d) autumn (SON) plotted against the percentage of the catchment area draining through rock glaciers. Each data point represents a specific sub-catchment, RCP scenario, and future time horizon, with the magnitude of change quantified using Hodges-Lehmann (HL) estimators calculated across the respective climate projections ensemble. Downstream catchments characterized by karst aquifers or valley-fill sediments—including Hammerjäger (H) in the Seckau Alps, Mauterndorf (M) in the Radstadt Alps, and Gargellen (G) in the Silvretta Alps—are explicitly highlighted. Colors indicate the emission scenarios: RCP 2.6 (blue), RCP 4.5 (orange), and RCP 8.5 (red). Color saturation denotes the time horizon: near-future periods (2030–2059) are shown in saturated colors, while far-future periods (2070–2099) are shown with transparency. Statistically significant changes (α=0.05) are highlighted with a black outline.

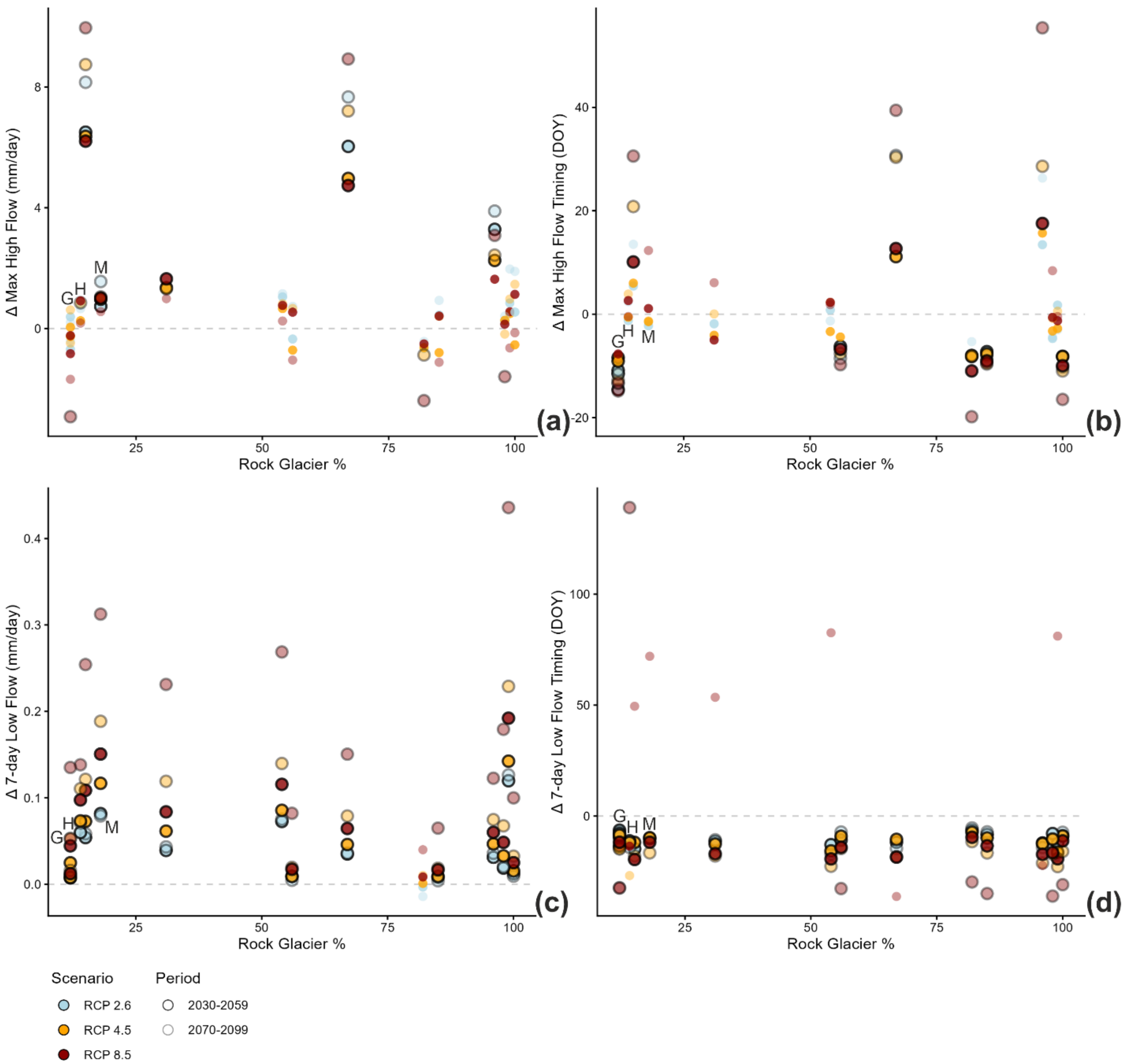

Supplementary Figure S38: Relationship between projected changes in extreme discharge metrics and catchment-scale rock glacier coverage. Panels show projected changes in (a) the magnitude of annual maximum flows, (b) the timing of annual maximum flows, (c) the magnitude of annual 7-day low flows, and (d) the timing of annual 7-day low flows plotted against the percentage of the catchment area draining through rock glaciers. Each data point represents a specific sub-catchment, RCP scenario, and future time horizon, with the magnitude of change quantified using Hodges-Lehmann (HL) estimators calculated across the respective climate projections ensemble. Downstream catchments characterized by karst aquifers or valley-fill sediments—including Hammerjäger (H) in the Seckau Alps, Mauterndorf (M) in the Radstadt Alps, and Gargellen (G) in the Silvretta Alps—are explicitly highlighted. Colors indicate the emission scenarios: RCP 2.6 (blue), RCP 4.5 (orange), and RCP 8.5 (red). Color saturation denotes the time horizon: near-future periods (2030–2059) are shown in saturated colors, while far-future periods (2070–2099) are shown with transparency. Statistically significant changes (α=0.05) are highlighted with a black outline.

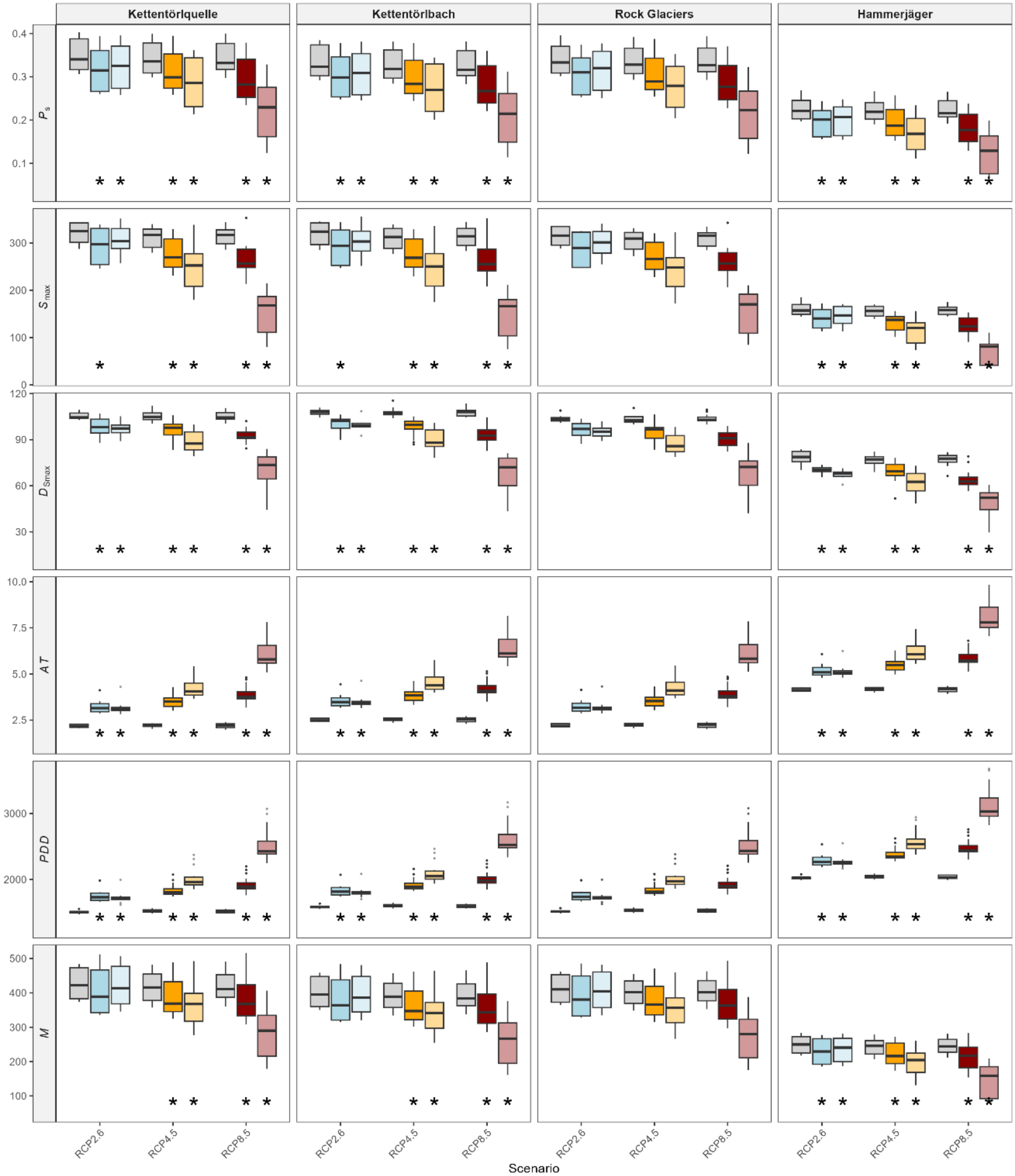

Supplementary Figure S39: Changes in snow dynamics and atmospheric drivers across the subcatchments of the Seckau Alps, quantified by snow fraction of precipitation (P_s), maximum snow water equivalent (S_{Smax}) and its timing (D_{Smax}), mean air temperature (*AT*), positive degree-day sum (*PDD*), and annual snowmelt volume (*M*). Boxplots illustrate the ensemble spread for the historical reference period (1980–2009; grey), and the projected shifts for the near-future (2030–2059; saturated colors) and far-future (2070–2099; transparent colors) periods. Results are disaggregated by emission scenario: RCP2.6 (blue), RCP4.5 (orange), and RCP8.5 (red). Asterisks below the boxplots denote statistically significant differences between the future period and the historical reference at the α=0.05 level, determined by the rank-sum test.

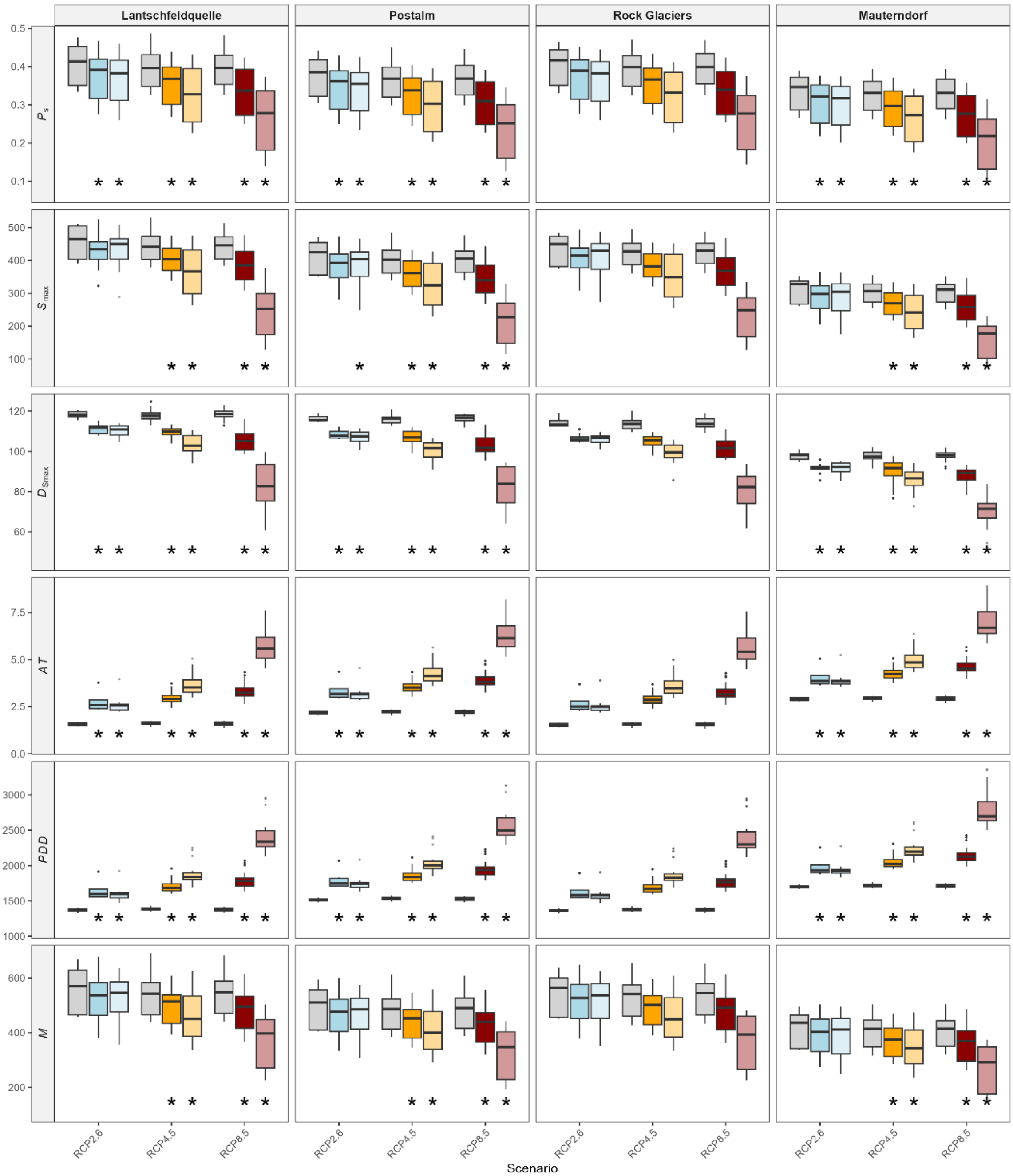

Supplementary Figure S40: Changes in snow dynamics and atmospheric drivers across the subcatchments of the Radstadt Alps, quantified by snow fraction of precipitation (P_s), maximum snow water equivalent (S_{Smax}) and its timing (D_{Smax}), mean air temperature (*AT*), positive degree-day sum (*PDD*), and annual snowmelt volume (*M*). Boxplots illustrate the ensemble spread for the historical reference period (1980–2009; grey), and the projected shifts for the near-future (2030–2059; saturated colors) and far-future (2070–2099; transparent colors) periods. Results are disaggregated by emission scenario: RCP2.6 (blue), RCP4.5 (orange), and RCP8.5 (red). Asterisks below the boxplots denote statistically significant differences between the future period and the historical reference at the α=0.05 level, determined by the rank-sum test.

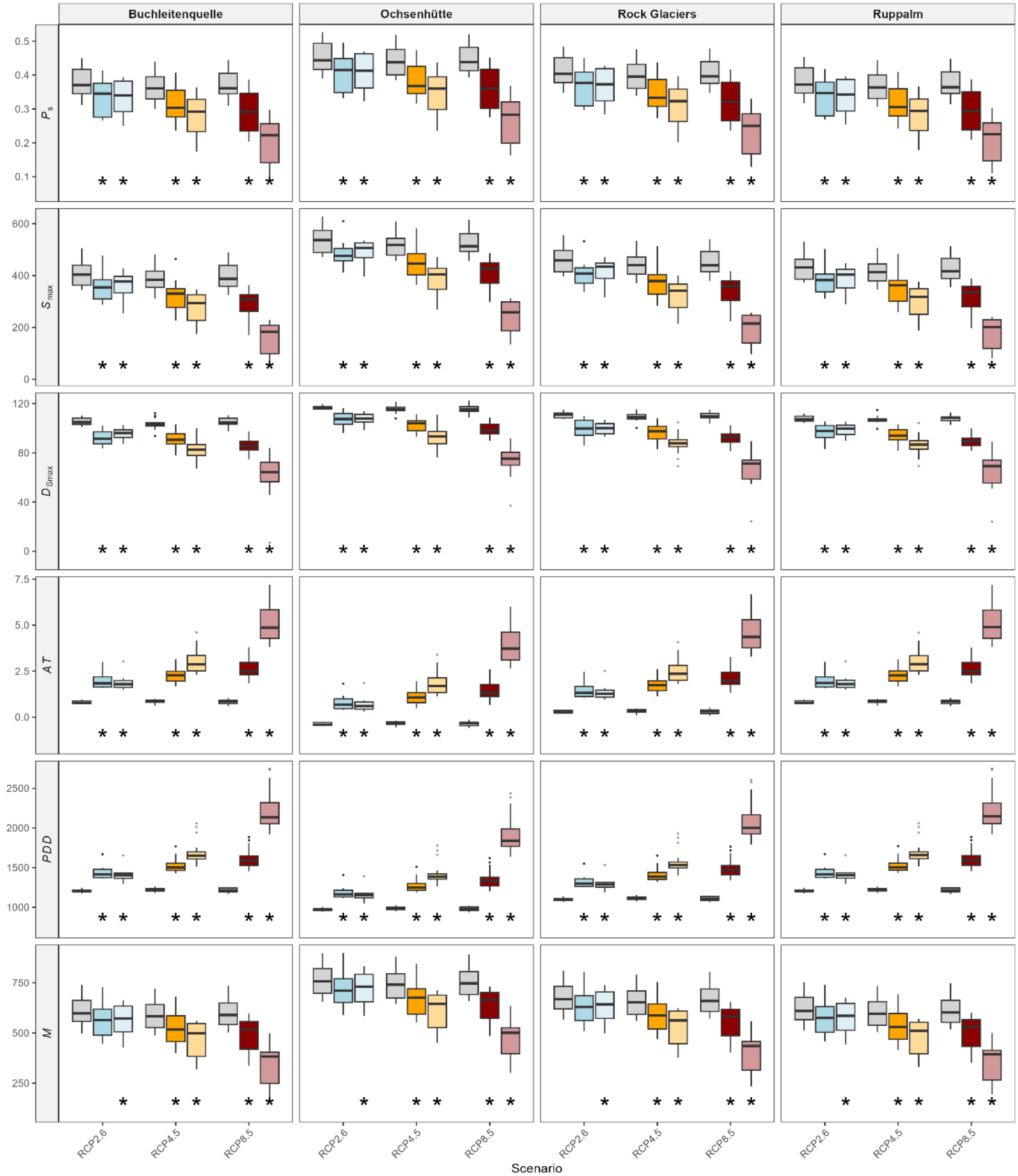

Supplementary Figure S41: Changes in snow dynamics and atmospheric drivers across the subcatchments of the Reißeck Group, quantified by snow fraction of precipitation (P_s), maximum snow water equivalent (S_{Smax}) and its timing (D_{Smax}), mean air temperature (*AT*), positive degree-day sum (*PDD*), and annual snowmelt volume (*M*). Boxplots illustrate the ensemble spread for the historical reference period (1980–2009; grey), and the projected shifts for the near-future (2030–2059; saturated colors) and far-future (2070–2099; transparent colors) periods. Results are disaggregated by emission scenario: RCP2.6 (blue), RCP4.5 (orange), and RCP8.5 (red). Asterisks below the boxplots denote statistically significant differences between the future period and the historical reference at the α=0.05 level, determined by the rank-sum test.

Supplementary Figure S42: Changes in snow dynamics and atmospheric drivers across the subcatchments of the Ötztal Alps, quantified by snow fraction of precipitation (P_s), maximum snow water equivalent (S_{Smax}) and its timing (D_{Smax}), mean air temperature (*AT*), positive degree-day sum (*PDD*), and annual snowmelt volume (*M*). Boxplots illustrate the ensemble spread for the historical reference period (1980–2009; grey), and the projected shifts for the near-future (2030–2059; saturated colors) and far-future (2070–2099; transparent colors) periods. Results are disaggregated by emission scenario: RCP2.6 (blue), RCP4.5 (orange), and RCP8.5 (red). Asterisks below the boxplots denote statistically significant differences between the future period and the historical reference at the α=0.05 level, determined by the rank-sum test.

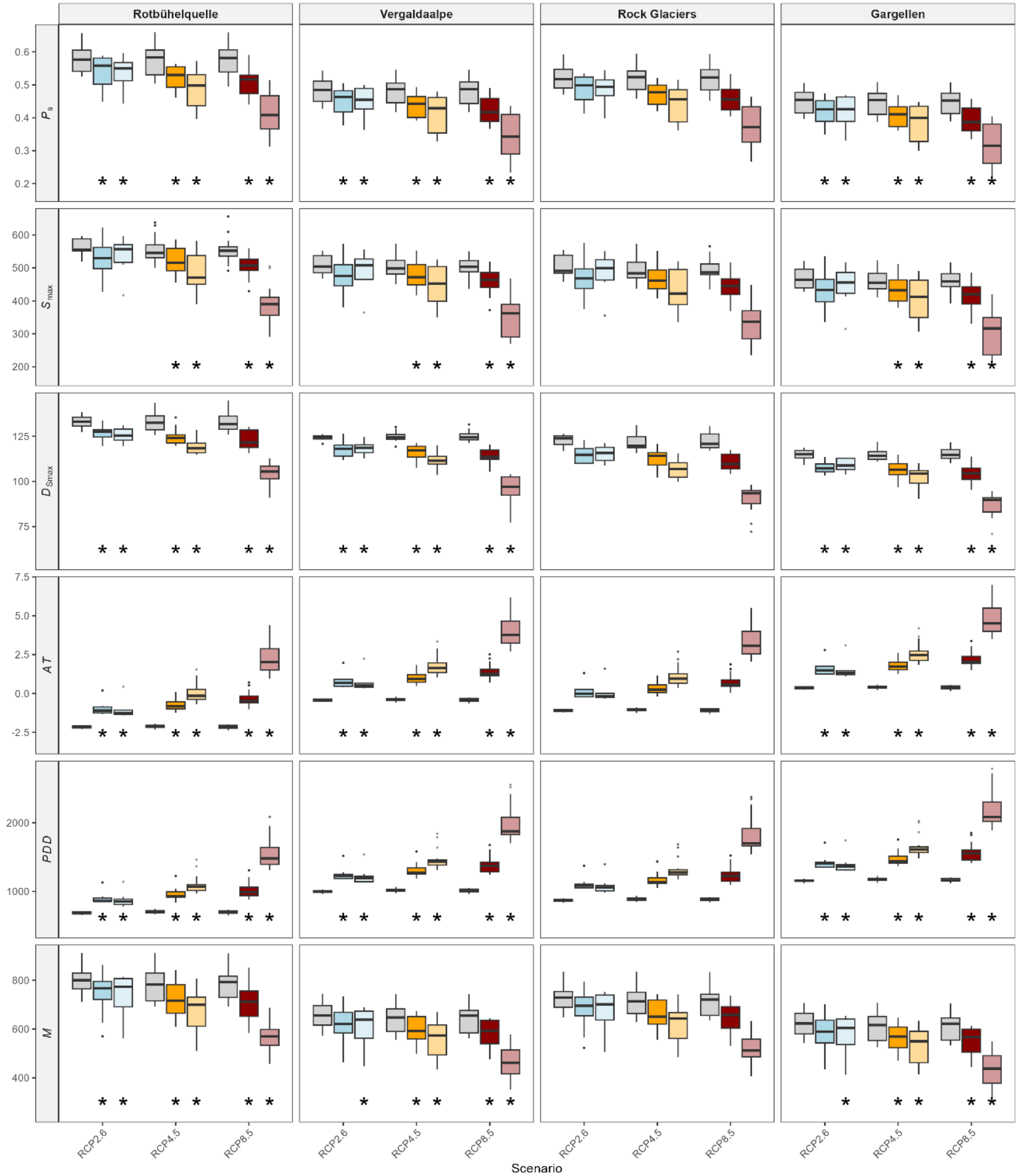

Supplementary Figure S43: Changes in snow dynamics and atmospheric drivers across the subcatchments of the Silvretta Alps, quantified by snow fraction of precipitation (P_s), maximum snow water equivalent (S_{Smax}) and its timing (D_{Smax}), mean air temperature (AT), positive degree-day sum (PDD), and annual snowmelt volume (M). Boxplots illustrate the ensemble spread for the historical reference period (1980–2009; grey), and the projected shifts for the near-future (2030–2059; saturated colors) and far-future (2070–2099; transparent colors) periods. Results are disaggregated by emission scenario: RCP2.6 (blue), RCP4.5 (orange), and RCP8.5 (red). Asterisks below the boxplots denote statistically significant differences between the future period and the historical reference at the α=0.05 level, determined by the rank-sum test.

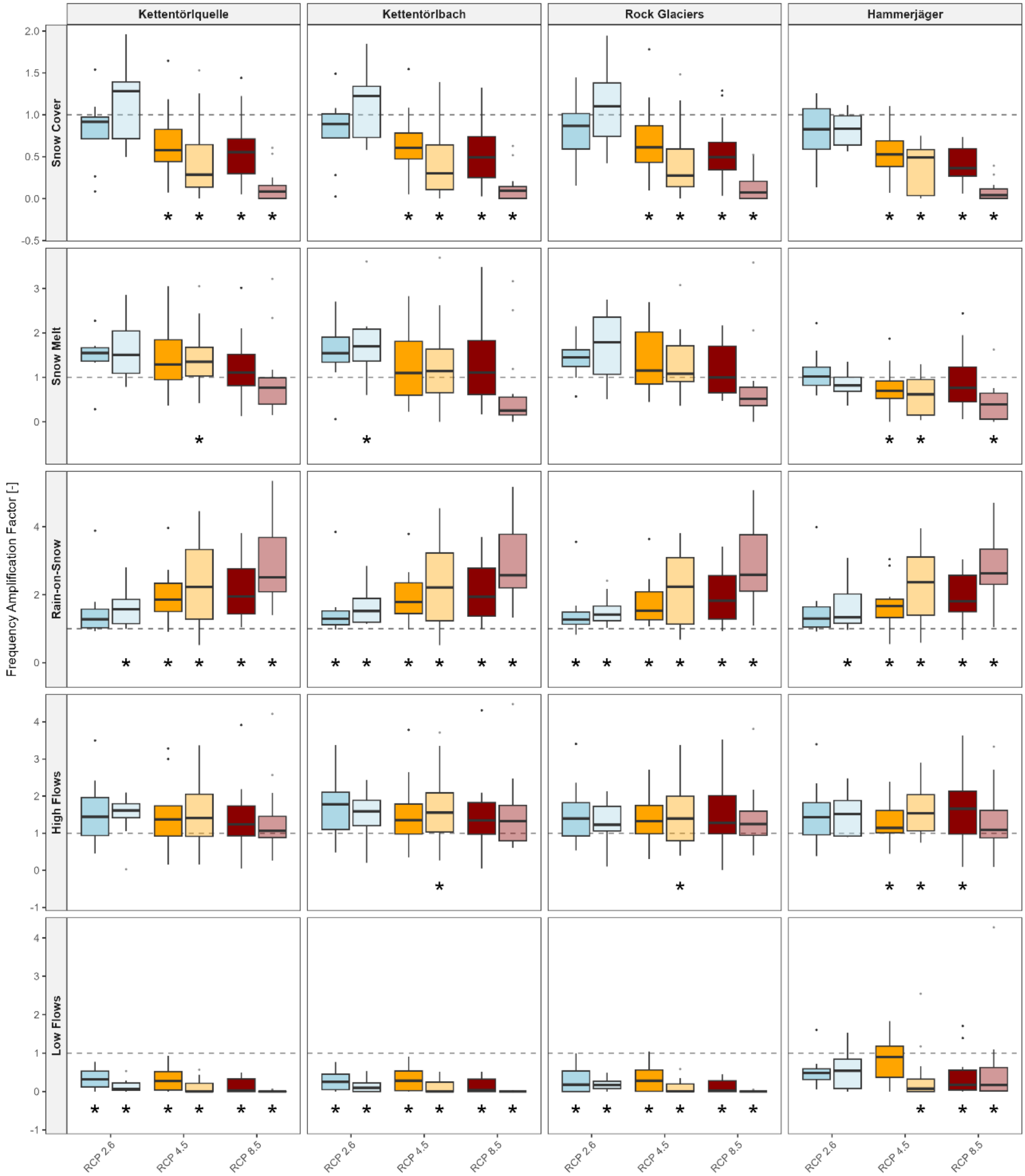

Supplementary Figure S44: Change in the frequency of historical 10-year events across the Seckau Alps subcatchments. Boxplots depict the ensemble spread across all climate model runs per RCP. The y-axis represents the frequency amplification factor, indicating the projected change in the likelihood of historical (1980–2009) 10-year return period events under future climate conditions. Results are disaggregated by emission scenario—RCP2.6 (blue), RCP4.5 (orange), and RCP8.5 (red)—and by time horizon: near-future (2030–2059; saturated colors) and far-future (2070–2099; transparent colors). Asterisks below the boxplots indicate that the shift in frequency is statistically significant at the α=0.05 level based on a rank-sum test.

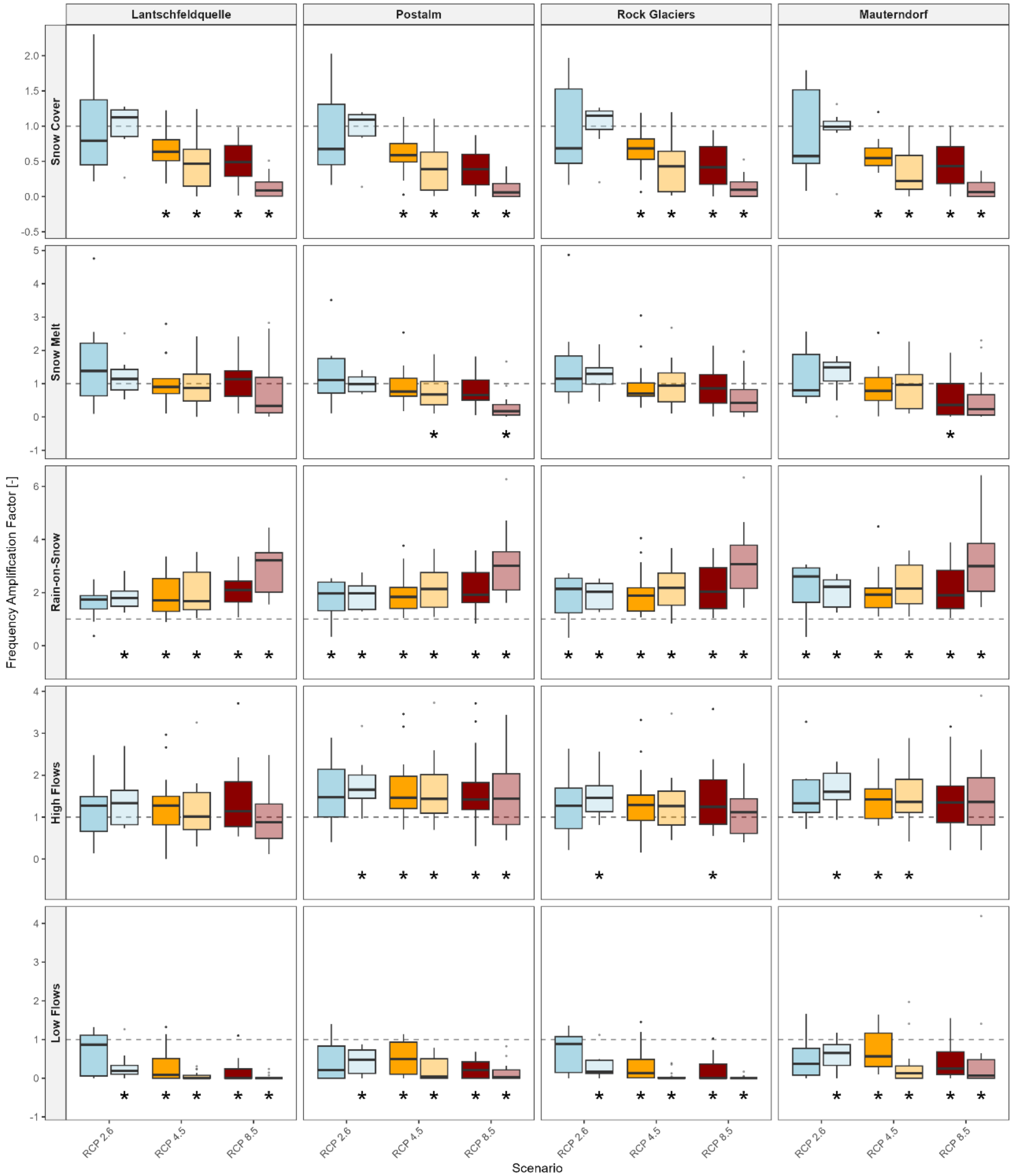

Supplementary Figure S45: Change in the frequency of historical 10-year events across the Radstadt Alps subcatchments. Boxplots depict the ensemble spread across all climate model runs per RCP. The y-axis represents the frequency amplification factor, indicating the projected change in the likelihood of historical (1980–2009) 10-year return period events under future climate conditions. Results are disaggregated by emission scenario—RCP2.6 (blue), RCP4.5 (orange), and RCP8.5 (red)—and by time horizon: near-future (2030–2059; saturated colors) and far-future (2070–2099; transparent colors). Asterisks below the boxplots indicate that the shift in frequency is statistically significant at the α=0.05 level based on a rank-sum test.

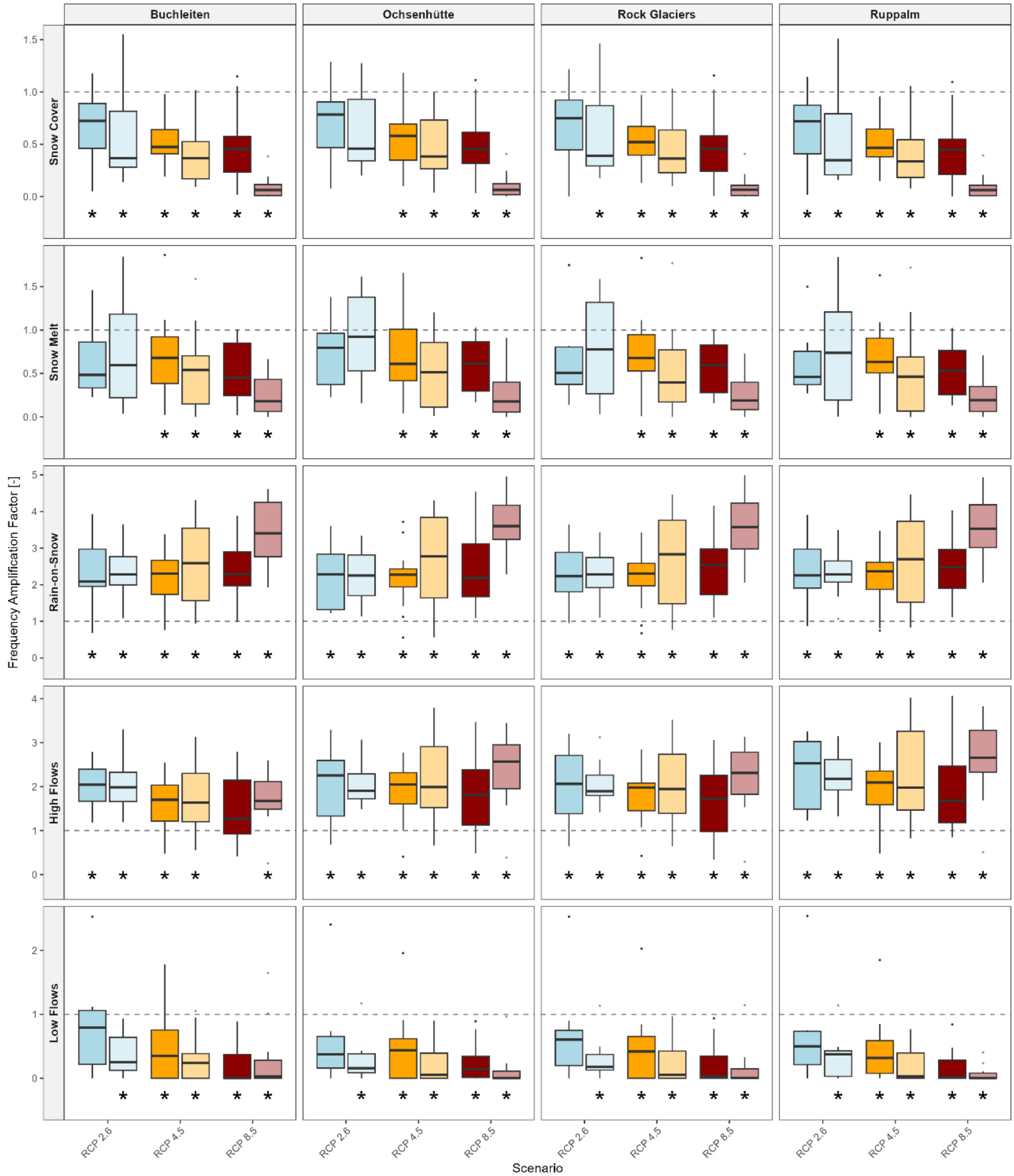

Supplementary Figure S46: Change in the frequency of historical 10-year events across the Reißeck Group subcatchments. Boxplots depict the ensemble spread across all climate model runs per RCP. The y-axis represents the frequency amplification factor, indicating the projected change in the likelihood of historical (1980–2009) 10-year return period events under future climate conditions. Results are disaggregated by emission scenario—RCP2.6 (blue), RCP4.5 (orange), and RCP8.5 (red)—and by time horizon: near-future (2030–2059; saturated colors) and far-future (2070–2099; transparent colors). Asterisks below the boxplots indicate that the shift in frequency is statistically significant at the α=0.05 level based on a rank-sum test.

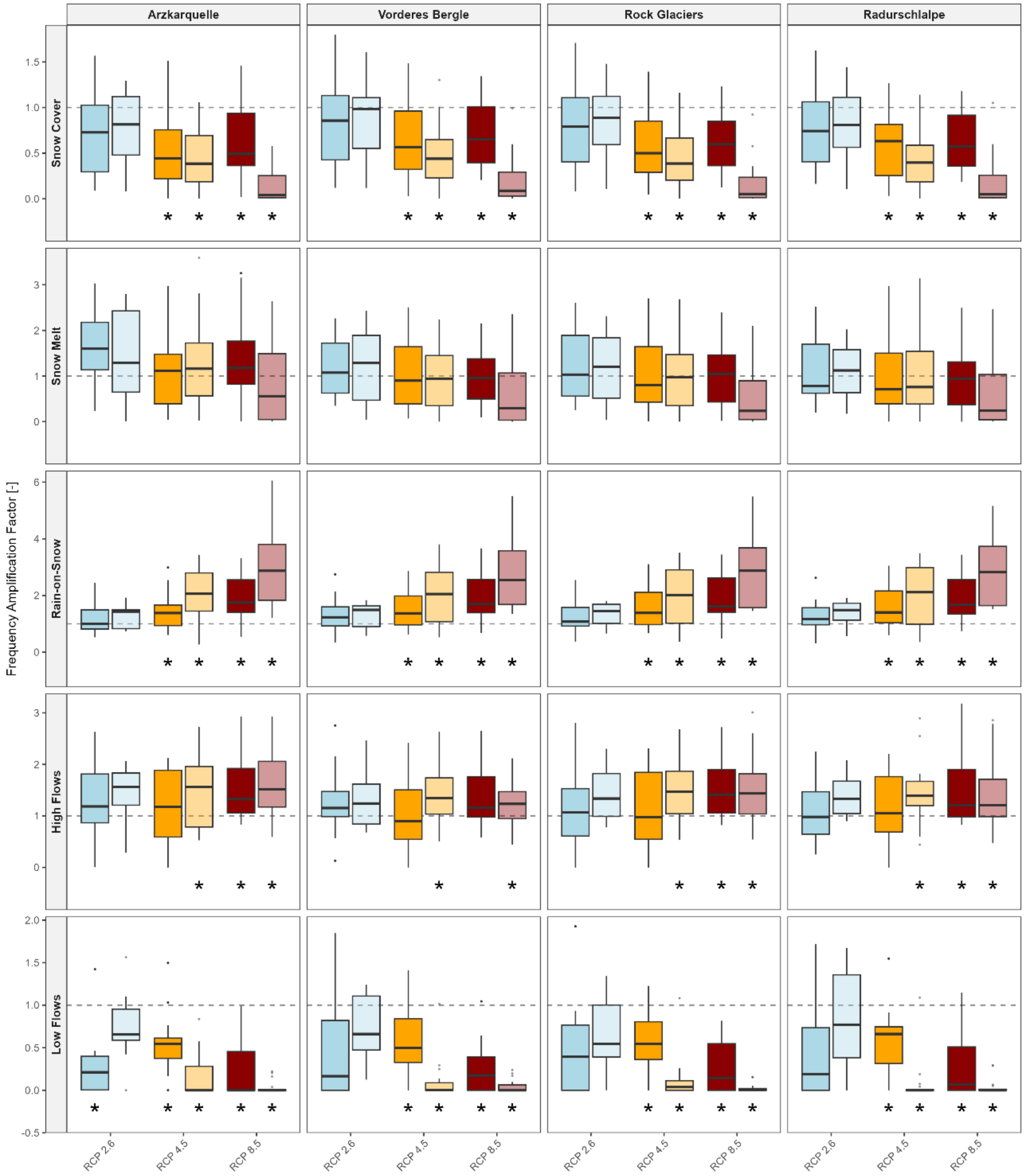

Supplementary Figure S47: Change in the frequency of historical 10-year events across the Ötztal Alps subcatchments. Boxplots depict the ensemble spread across all climate model runs per RCP. The y-axis represents the frequency amplification factor, indicating the projected change in the likelihood of historical (1980–2009) 10-year return period events under future climate conditions. Results are disaggregated by emission scenario—RCP2.6 (blue), RCP4.5 (orange), and RCP8.5 (red)—and by time horizon: near-future (2030–2059; saturated colors) and far-future (2070–2099; transparent colors). Asterisks below the boxplots indicate that the shift in frequency is statistically significant at the α=0.05 level based on a rank-sum test.

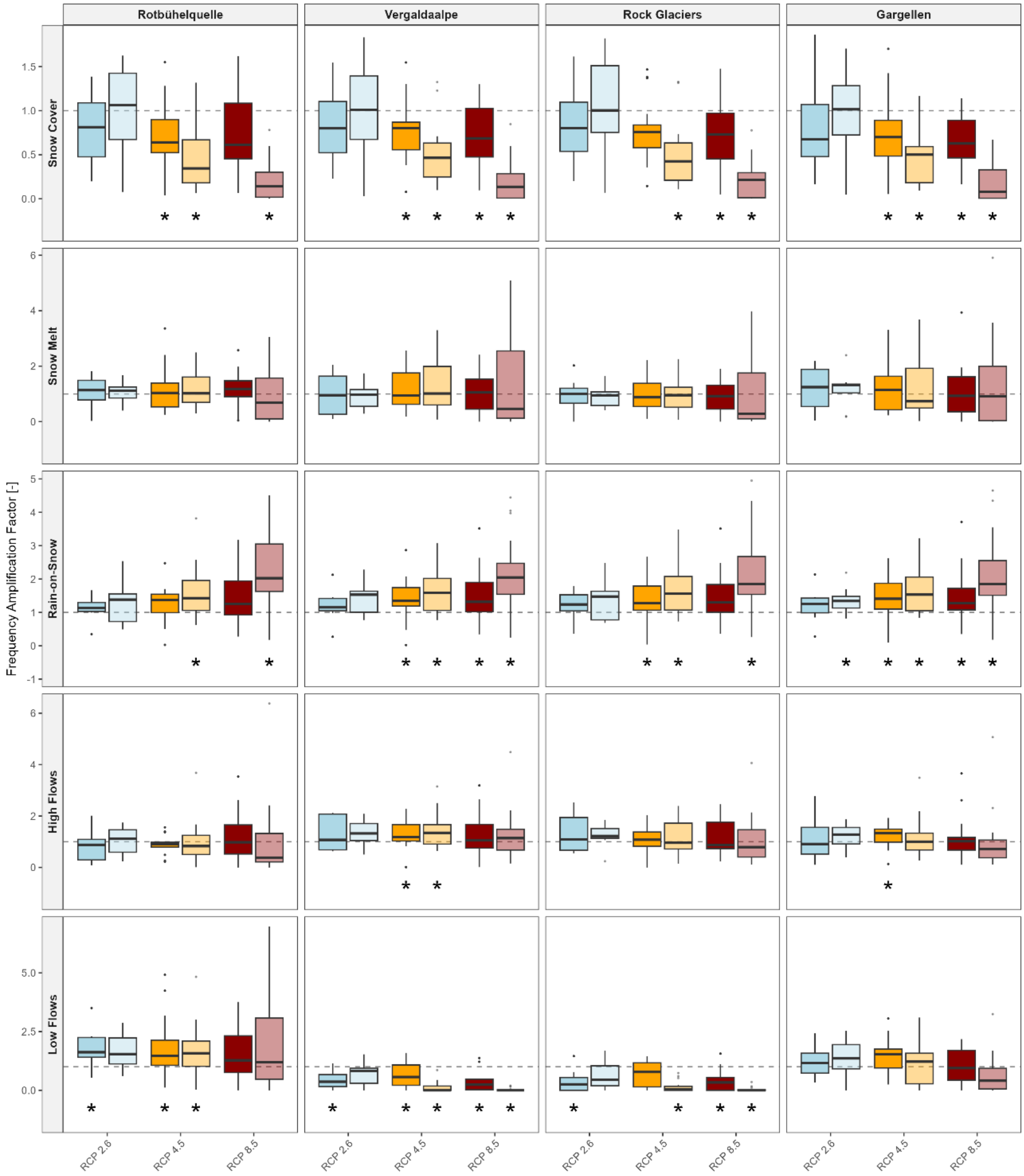

Supplementary Figure S48: Change in the frequency of historical 10-year events across the Silvretta Alps subcatchments. Boxplots depict the ensemble spread across all climate model runs per RCP. The y-axis represents the frequency amplification factor, indicating the projected change in the likelihood of historical (1980–2009) 10-year return period events under future climate conditions. Results are disaggregated by emission scenario—RCP2.6 (blue), RCP4.5 (orange), and RCP8.5 (red)—and by time horizon: near-future (2030–2059; saturated colors) and far-future (2070–2099; transparent colors). Asterisks below the boxplots indicate that the shift in frequency is statistically significant at the α=0.05 level based on a rank-sum test.

Supplementary Table S1: Projected changes in hydrometeorological indices across study sites under RCP scenarios. This table summarizes changes aggregated per study site for individual RCP scenarios, comparing a near-future period (2030–2059) and a far-future period (2070–2099) against the historical reference period. Reported indices include annual runoff (Q) and seasonal runoff for winter (Q_{DJF}), spring (Q_{MAM}), summer (Q_{JJA}), and autumn (Q_{SON}). For each site, scenario, and time horizon, changes are quantified using the Hodges–Lehmann (HL) estimator as a robust measure of the median shift, together with the corresponding *p*-value from a Wilcoxon rank-sum test to assess statistical significance of the differences between periods.

Index	RCP	Seckau Alps		Radstadt Alps		Reißeck Group		Ötztal Alps		Silvretta Alps	
		2030-2059	2070-2099	2030-2059	2070-2099	2030-2059	2070-2099	2030-2059	2070-2099	2030-2059	2070-2099
Q	2.6	p=0.007; HL=46.3	p=<0.001; HL=65.6	p=0.107; HL=16.4	p=0.023; HL=33.1	p=<0.001; HL=39.9	p=0.002; HL=45.9	p=0.107; HL=-12.9	p=0.855; HL=-3.1	p=<0.001; HL=-52.4	p=0.004; HL=-42.0
Q	4.5	p=0.010; HL=26.9	p=<0.001; HL=63.2	p=0.114; HL=17.0	p=0.016; HL=28.3	p=0.706; HL=3.3	p=0.006; HL=36.1	p=0.029; HL=-22.4	p=0.703; HL=-4.0	p=0.084; HL=-26.6	p=0.006; HL=-38.6
Q	8.5	p=<0.001; HL=64.7	p=0.012; HL=46.6	p=0.001; HL=41.0	p=0.644; HL=7.6	p=0.005; HL=34.2	p=0.721; HL=5.0	p=0.622; HL=4.7	p=0.088; HL=-28.1	p=0.193; HL=-32.7	p=<0.001; HL=-137.6
Q_{DJF}	2.6	p=<0.001; HL=18.4	p=<0.001; HL=17.1	p=<0.001; HL=10.3	p=<0.001; HL=12.8	p=<0.001; HL=16.5	p=<0.001; HL=11.5	p=<0.001; HL=3.2	p=0.004; HL=2.4	p=0.790; HL=0.4	p=0.623; HL=-0.6
Q_{DJF}	4.5	p=<0.001; HL=27.5	p=<0.001; HL=46.1	p=<0.001; HL=18.1	p=<0.001; HL=32.4	p=<0.001; HL=23.5	p=<0.001; HL=44.3	p=<0.001; HL=3.5	p=<0.001; HL=7.7	p=0.051; HL=1.9	p=0.003; HL=4.1
Q_{DJF}	8.5	p=<0.001; HL=35.6	p=<0.001; HL=108.2	p=<0.001; HL=22.6	p=<0.001; HL=77.3	p=<0.001; HL=27.3	p=<0.001; HL=88.9	p=<0.001; HL=6.0	p=<0.001; HL=27.7	p=0.021; HL=3.0	p=<0.001; HL=16.6
Q_{MAM}	2.6	p=<0.001; HL=55.0	p=<0.001; HL=60.1	p=<0.001; HL=60.0	p=<0.001; HL=62.6	p=<0.001; HL=65.9	p=<0.001; HL=66.4	p=<0.001; HL=41.5	p=<0.001; HL=36.2	p=<0.001; HL=34.5	p=<0.001; HL=33.7
Q_{MAM}	4.5	p=<0.001; HL=55.8	p=<0.001; HL=73.1	p=<0.001; HL=62.0	p=<0.001; HL=88.7	p=<0.001; HL=58.6	p=<0.001; HL=81.9	p=<0.001; HL=49.5	p=<0.001; HL=80.5	p=<0.001; HL=45.0	p=<0.001; HL=69.6
Q_{MAM}	8.5	p=<0.001; HL=68.2	p=<0.001; HL=65.4	p=<0.001; HL=80.6	p=<0.001; HL=105.9	p=<0.001; HL=69.9	p=<0.001; HL=86.2	p=<0.001; HL=66.2	p=<0.001; HL=154.8	p=<0.001; HL=60.9	p=<0.001; HL=112.4
Q_{JJA}	2.6	p=0.001; HL=-41.2	p=<0.001; HL=-28.6	p=<0.001; HL=-56.0	p=<0.001; HL=-53.2	p=<0.001; HL=-60.1	p=<0.001; HL=-60.8	p=<0.001; HL=-50.1	p=0.004; HL=-33.4	p=<0.001; HL=-62.1	p=<0.001; HL=-51.3
Q_{JJA}	4.5	p=<0.001; HL=-53.8	p=<0.001; HL=-68.0	p=<0.001; HL=-68.1	p=<0.001; HL=-96.4	p=<0.001; HL=-76.9	p=<0.001; HL=-101.3	p=<0.001; HL=-74.9	p=<0.001; HL=-92.5	p=<0.001; HL=-63.6	p=<0.001; HL=-99.4
Q_{JJA}	8.5	p=<0.001; HL=-49.8	p=<0.001; HL=-141.7	p=<0.001; HL=-71.0	p=<0.001; HL=-189.4	p=<0.001; HL=-78.3	p=<0.001; HL=-187.3	p=<0.001; HL=-76.6	p=<0.001; HL=-228.7	p=<0.001; HL=-77.5	p=<0.001; HL=-220.7
Q_{SON}	2.6	p=0.603; HL=-2.3	p=0.014; HL=17.4	p=0.509; HL=-3.2	p=0.010; HL=12.8	p=<0.001; HL=16.9	p=<0.001; HL=24.9	p=0.303; HL=-6.6	p=<0.001; HL=-11.3	p=0.005; HL=-21.6	p=<0.001; HL=-24.8
Q_{SON}	4.5	p=0.796; HL=0.8	p=<0.001; HL=12.9	p=0.430; HL=3.4	p=0.137; HL=5.0	p=0.317; HL=4.3	p=0.026; HL=12.2	p=0.572; HL=1.2	p=0.008; HL=7.5	p=0.287; HL=-5.7	p=0.007; HL=-12.3
Q_{SON}	8.5	p=<0.001; HL=13.4	p=0.008; HL=15.4	p=0.034; HL=6.9	p=0.226; HL=6.5	p=<0.001; HL=18.7	p=0.011; HL=12.9	p=<0.001; HL=9.4	p=<0.001; HL=18.6	p=0.255; HL=-7.0	p=<0.001; HL=-28.5

Supplementary Table S2: Projected changes in hydrometeorological indices across study sites under RCP scenarios. This table summarizes changes aggregated per study site for individual RCP scenarios, comparing a near-future period (2030–2059) and a far-future period (2070–2099) against the historical reference period. Reported indices include Richards-Baker flashiness index (*RB*), annual maximum flow (Q_{max}) and its timing (D_{max}), as well as annual minimum 7-day low flow (Q_{7min}) and its timing (D_{7min}). For each site, scenario, and time horizon, changes are quantified using the Hodges–Lehmann (HL) estimator as a robust measure of the median shift, together with the corresponding *p*-value from a Wilcoxon rank-sum test to assess statistical significance of the differences between periods.

Index	**RCP**	**Seckau Alps**		**Radstadt Alps**		**Reißeck Group**		**Ötztal Alps**		**Silvretta Alps**	
		2030-2059	**2070-2099**	**2030-2059**	**2070-2099**	**2030-2059**	**2030-2059**	**2070-2099**	**2030-2059**	**2070-2099**	**2030-2059**
RB	2.6	p=0.003; HL=+0.005	p=0.001; HL=+0.004	p=<0.001; HL=+0.006	p=<0.001; HL=+0.006	p=<0.001; HL=+0.013	p=<0.001; HL=+0.013	p=0.663; HL=-0.001	p=0.900; HL=+0.000	p=0.107; HL=-0.002	p=0.003; HL=-0.002
RB	4.5	p=<0.001;HL=+0.005	p=<0.001;HL=+0.008	p=<0.001;HL=+0.007	p=<0.001;HL=+0.010	p=<0.001;HL=+0.014	p=<0.001;HL=+0.023	p=0.923;HL=+0.000	p=<0.001;HL=+0.006	p=0.211;HL=+0.001	p=0.055;HL=+0.003
RB	8.5	p=0.003;HL=+0.005	p=0.001;HL=+0.004	p=<0.001;HL=+0.006	p=<0.001;HL=+0.006	p=<0.001;HL=+0.013	p=<0.001;HL=+0.013	p=0.663;HL=-0.001	p=0.900;HL=+0.000	p=0.107;HL=-0.002	p=0.003;HL=-0.002
Q_{max}	2.6	p=0.031; HL=0.9	p=0.007; HL=1.2	p=0.074; HL=0.7	p=0.002; HL=1.2	p=<0.001; HL=4.7	p=<0.001; HL=6.1	p=0.768; HL=0.2	p=0.021; HL=1.1	p=0.643; HL=-0.3	p=0.360; HL=-0.3
Q_{max}	4.5	p=0.032; HL=0.4	p=0.002; HL=0.8	p=0.003; HL=0.8	p=0.006; HL=0.8	p=<0.001; HL=4.0	p=<0.001; HL=5.5	p=0.070; HL=-0.6	p=0.012; HL=0.8	p=0.215; HL=-0.3	p=0.384; HL=-0.3
Q_{max}	8.5	p=0.037; HL=0.7	p=0.867; HL=-0.1	p=<0.001; HL=1.0	p=0.955; HL=-0.0	p=<0.001; HL=3.7	p=<0.001; HL=6.9	p=0.025; HL=0.7	p=0.134; HL=-0.8	p=0.139; HL=-0.5	p=<0.001; HL=-2.3
D_{max}	2.6	p=0.747; HL=1.0	p=0.439; HL=-1.2	p=0.218; HL=-2.7	p=0.136; HL=-4.4	p=0.052; HL=10.6	p=<0.001; HL=20.3	p=<0.001; HL=-7.0	p=<0.001; HL=-8.6	p=<0.001; HL=-11.0	p=<0.001; HL=-9.7
D_{max}	4.5	p=0.243; HL=-2.0	p=0.273; HL=2.1	p=0.148; HL=-2.8	p=0.733; HL=-0.7	p=0.003; HL=10.6	p=<0.001; HL=25.0	p=<0.001; HL=-6.8	p=<0.001; HL=-9.6	p=<0.001; HL=-9.4	p=<0.001; HL=-9.6
D_{max}	8.5	p=0.666; HL=0.9	p=0.835; HL=0.7	p=0.306; HL=-1.8	p=0.057; HL=9.6	p=<0.001; HL=12.7	p=<0.001; HL=39.6	p=<0.001; HL=-8.7	p=<0.001; HL=-11.9	p=<0.001; HL=-9.0	p=<0.001; HL=-15.5
Q_{7min}	2.6	p=<0.001; HL=0.1	p=<0.001; HL=0.1	p=<0.001; HL=0.0	p=<0.001; HL=0.0	p=<0.001; HL=0.0	p=<0.001; HL=0.0	p=<0.001; HL=0.0	p=<0.001; HL=0.0	p=0.053; HL=0.0	p=0.277; HL=0.0
Q_{7min}	4.5	p=<0.001; HL=0.1	p=<0.001; HL=0.2	p=<0.001; HL=0.1	p=<0.001; HL=0.1	p=<0.001; HL=0.1	p=<0.001; HL=0.1	p=<0.001; HL=0.0	p=<0.001; HL=0.0	p=<0.001; HL=0.0	p=<0.001; HL=0.0
Q_{7min}	8.5	p=<0.001; HL=0.1	p=<0.001; HL=0.3	p=<0.001; HL=0.1	p=<0.001; HL=0.2	p=<0.001; HL=0.1	p=<0.001; HL=0.2	p=<0.001; HL=0.0	p=<0.001; HL=0.1	p=<0.001; HL=0.0	p=<0.001; HL=0.1
D_{7min}	2.6	p=<0.001; HL=-12.4	p=<0.001; HL=-16.2	p=<0.001; HL=-9.1	p=<0.001; HL=-10.6	p=<0.001; HL=-12.7	p=<0.001; HL=-14.8	p=<0.001; HL=-9.5	p=<0.001; HL=-7.2	p=<0.001; HL=-7.1	p=<0.001; HL=-7.0
D_{7min}	4.5	p=<0.001; HL=-14.7	p=<0.001; HL=-23.9	p=<0.001; HL=-10.8	p=<0.001; HL=-17.3	p=<0.001; HL=-11.9	p=<0.001; HL=-19.3	p=<0.001; HL=-9.2	p=<0.001; HL=-15.7	p=<0.001; HL=-8.3	p=<0.001; HL=-13.5
D_{7min}	8.5	p=<0.001; HL=-17.0	p=0.001; HL=104.4	p=<0.001; HL=-15.3	p=0.118; HL=-28.5	p=<0.001; HL=-18.5	p=0.787; HL=-21.4	p=<0.001; HL=-12.8	p=<0.001; HL=-33.0	p=<0.001; HL=-11.6	p=<0.001; HL=-30.9

Supplementary Table S3: Projected changes in hydrometeorological indices across study sites under RCP scenarios. This table summarizes changes aggregated per study site for individual RCP scenarios, comparing a near-future period (2030–2059) and a far-future period (2070–2099) against the historical reference period. Reported indices include maximum snow water equivalent (S_{max}) and its timing (D_{Smax}), as well as maximum snowmelt rate (M_{max}) and its timing (D_{Mmax}). For each site, scenario, and time horizon, changes are quantified using the Hodges–Lehmann (HL) estimator as a robust measure of the median shift, together with the corresponding *p*-value from a Wilcoxon rank-sum test to assess statistical significance of the differences between periods.

Index	**RCP**	**Seckau Alps**		**Radstadt Alps**		**Reißeck Group**		**Ötztal Alps**		**Silvretta Alps**	
		2030-2059	**2070-2099**	**2030-2059**	**2070-2099**	**2030-2059**	**2030-2059**	**2070-2099**	**2030-2059**	**2070-2099**	**2030-2059**
S_{max}	2.6	p=<0.001; HL=-23.6	p=<0.001; HL=-14.5	p=0.002; HL=-22.8	p=<0.001; HL=-19.4	p=<0.001; HL=-53.2	p=<0.001; HL=-50.8	p=<0.001; HL=-30.6	p=0.005; HL=-22.4	p=0.001; HL=-28.8	p=0.034; HL=-12.2
S_{max}	4.5	p=<0.001; HL=-30.5	p=<0.001; HL=-54.8	p=<0.001; HL=-36.5	p=<0.001; HL=-67.4	p=<0.001; HL=-71.3	p=<0.001; HL=-116.3	p=<0.001; HL=-39.1	p=<0.001; HL=-67.1	p=<0.001; HL=-28.2	p=<0.001; HL=-62.0
S_{max}	8.5	p=<0.001; HL=-45.6	p=<0.001; HL=-135.4	p=<0.001; HL=-52.4	p=<0.001; HL=-172.3	p=<0.001; HL=-105.6	p=<0.001; HL=-256.5	p=<0.001; HL=-47.8	p=<0.001; HL=-150.2	p=<0.001; HL=-44.8	p=<0.001; HL=-156.1
D_{Smax}	2.6	p=<0.001; HL=-8.0	p=<0.001; HL=-9.2	p=<0.001; HL=-7.1	p=<0.001; HL=-7.8	p=<0.001; HL=-11.2	p=<0.001; HL=-9.8	p=<0.001; HL=-6.5	p=<0.001; HL=-7.5	p=<0.001; HL=-6.8	p=<0.001; HL=-6.2
D_{Smax}	4.5	p=<0.001; HL=-8.7	p=<0.001; HL=-16.3	p=<0.001; HL=-8.2	p=<0.001; HL=-14.0	p=<0.001; HL=-12.8	p=<0.001; HL=-21.4	p=<0.001; HL=-9.9	p=<0.001; HL=-14.3	p=<0.001; HL=-8.3	p=<0.001; HL=-12.7
D_{Smax}	8.5	p=<0.001; HL=-14.3	p=<0.001; HL=-33.8	p=<0.001; HL=-11.9	p=<0.001; HL=-31.4	p=<0.001; HL=-18.2	p=<0.001; HL=-41.1	p=<0.001; HL=-11.7	p=<0.001; HL=-31.8	p=<0.001; HL=-10.2	p=<0.001; HL=-28.5
M_{max}	2.6	p=0.003; HL=0.3	p=0.290; HL=0.2	p=0.877; HL=-0.1	p=0.049; HL=-0.5	p=<0.001; HL=-1.4	p=0.006; HL=-1.0	p=0.643; HL=0.2	p=0.790; HL=0.2	p=0.877; HL=-0.1	p=0.833; HL=-0.1
M_{max}	4.5	p=0.418; HL=-0.1	p=0.018; HL=-0.4	p=0.086; HL=-0.4	p=0.009; HL=-0.8	p=<0.001; HL=-1.3	p=<0.001; HL=-2.3	p=0.479; HL=-0.3	p=0.033; HL=-0.8	p=0.867; HL=0.1	p=0.351; HL=-0.5
M_{max}	8.5	p=0.038; HL=-0.3	p=<0.001; HL=-2.2	p=0.002; HL=-0.7	p=<0.001; HL=-3.3	p=<0.001; HL=-2.3	p=<0.001; HL=-5.4	p=0.215; HL=-0.5	p=<0.001; HL=-3.4	p=0.215; HL=-0.4	p=0.003; HL=-2.9
D_{Mmax}	2.6	p=<0.001; HL=-9.8	p=<0.001; HL=-12.7	p=<0.001; HL=-8.4	p=<0.001; HL=-10.3	p=<0.001; HL=-17.8	p=<0.001; HL=-15.4	p=<0.001; HL=-9.5	p=<0.001; HL=-8.5	p=<0.001; HL=-9.0	p=<0.001; HL=-8.1
D_{Mmax}	4.5	p=<0.001; HL=-14.1	p=<0.001; HL=-22.2	p=<0.001; HL=-10.6	p=<0.001; HL=-18.7	p=<0.001; HL=-20.0	p=<0.001; HL=-29.8	p=<0.001; HL=-12.5	p=<0.001; HL=-17.6	p=<0.001; HL=-9.4	p=<0.001; HL=-14.3
D_{Mmax}	8.5	p=<0.001; HL=-20.0	p=<0.001; HL=-48.2	p=<0.001; HL=-14.2	p=<0.001; HL=-40.8	p=<0.001; HL=-26.6	p=<0.001; HL=-64.3	p=<0.001; HL=-13.4	p=<0.001; HL=-35.5	p=<0.001; HL=-12.2	p=<0.001; HL=-31.0

Supplementary Table S4: Projected changes in frequency amplification factors of extreme hydrological events across study sites under RCP scenarios. This table summarizes changes aggregated per study site for individual RCP scenarios, comparing a near-future period (2030–2059) and a far-future period (2070–2099) against the historical reference period. Reported indices characterize changes in the frequency of extreme events defined by historical return periods of 10 years, including extremely snow-rich winters (maximum snow water equivalent), extreme snowmelt events (maximum daily snowmelt rate), extreme rain-on-snow events (co-occurring maximum melt and rainfall on a single day), extreme high flows, and extreme 7-day low flows. For each site, scenario, and time horizon, shifts are quantified using the Hodges–Lehmann (HL) estimator as a robust measure of the median change, together with the corresponding *p*-value from a Wilcoxon rank-sum test to assess the statistical significance of the differences between periods.

Index	**RCP**	**Seckau Alps**		**Radstadt Alps**		**Reißeck Group**		**Ötztal Alps**		**Silvretta Alps**	
		2030-2059	**2070-2099**	**2030-2059**	**2070-2099**	**2030-2059**			**2030-2059**	**2070-2099**	**2030-2059**
Snow Cover	2.6	p=0.014; HL=0.86	p=0.719; HL=1.03	p=0.692; HL=0.95	p=0.36; HL=1.04	p=<0.001; HL=0.71	p=<0.001; HL=0.55	p=0.019; HL=0.77	p=0.045; HL=0.83	p=0.045; HL=0.8	p=0.846; HL=1.03
Snow Cover	4.5	p=<0.001; HL=0.6	p=<0.001; HL=0.37	p=<0.001; HL=0.62	p=<0.001; HL=0.4	p=<0.001; HL=0.52	p=<0.001; HL=0.4	p=<0.001; HL=0.59	p=<0.001; HL=0.43	p=<0.001; HL=0.73	p=<0.001; HL=0.44
Snow Cover	8.5	p=<0.001; HL=0.49	p=<0.001; HL=0.08	p=<0.001; HL=0.44	p=<0.001; HL=0.1	p=<0.001; HL=0.45	p=<0.001; HL=0.07	p=<0.001; HL=0.64	p=<0.001; HL=0.13	p=<0.001; HL=0.69	p=<0.001; HL=0.17
Snow Melt	2.6	p=<0.001; HL=1.41	p=0.003; HL=1.44	p=0.106; HL=1.3	p=0.057; HL=1.17	p=<0.001; HL=0.6	p=0.08; HL=0.81	p=0.091; HL=1.26	p=0.115; HL=1.24	p=0.638; HL=1.05	p=0.861; HL=1.02
Snow Melt	4.5	p=0.151; HL=1.16	p=0.174; HL=1.11	p=0.097; HL=0.86	p=0.12; HL=0.85	p=<0.001; HL=0.67	p=<0.001; HL=0.5	p=0.981; HL=1	p=0.854; HL=0.98	p=0.563; HL=1.07	p=0.42; HL=1.1
Snow Melt	8.5	p=0.51; HL=1.06	p=<0.001; HL=0.51	p=0.06; HL=0.82	p=<0.001; HL=0.38	p=<0.001; HL=0.55	p=<0.001; HL=0.24	p=0.394; HL=1.07	p=0.029; HL=0.54	p=0.965; HL=1	p=0.536; HL=1.05
Rain-on-Snow	2.6	p=<0.001; HL=1.33	p=<0.001; HL=1.55	p=<0.001; HL=1.91	p=<0.001; HL=1.91	p=<0.001; HL=2.31	p=<0.001; HL=2.3	p=0.05; HL=1.22	p=<0.001; HL=1.32	p=0.011; HL=1.2	p=<0.001; HL=1.36
Rain-on-Snow	4.5	p=<0.001; HL=1.75	p=<0.001; HL=2.3	p=<0.001; HL=1.9	p=<0.001; HL=2.16	p=<0.001; HL=2.24	p=<0.001; HL=2.69	p=<0.001; HL=1.49	p=<0.001; HL=2.02	p=<0.001; HL=1.39	p=<0.001; HL=1.59
Rain-on-Snow	8.5	p=<0.001; HL=1.95	p=<0.001; HL=2.79	p=<0.001; HL=2.11	p=<0.001; HL=2.95	p=<0.001; HL=2.36	p=<0.001; HL=3.59	p=<0.001; HL=1.88	p=<0.001; HL=2.8	p=<0.001; HL=1.42	p=<0.001; HL=2.03
High Flows	2.6	p=<0.001; HL=1.5	p=<0.001; HL=1.51	p=0.002; HL=1.38	p=<0.001; HL=1.57	p=<0.001; HL=2.13	p=<0.001; HL=2.06	p=0.203; HL=1.16	p=<0.001; HL=1.4	p=0.436; HL=1.13	p=0.01; HL=1.23
High Flows	4.5	p=<0.001; HL=1.33	p=<0.001; HL=1.53	p=<0.001; HL=1.39	p=<0.001; HL=1.38	p=<0.001; HL=1.88	p=<0.001; HL=2.02	p=0.254; HL=1.11	p=<0.001; HL=1.43	p=0.008; HL=1.14	p=0.117; HL=1.12
High Flows	8.5	p=<0.001; HL=1.37	p=0.002; HL=1.22	p=<0.001; HL=1.39	p=0.006; HL=1.25	p=<0.001; HL=1.72	p=<0.001; HL=2.3	p=<0.001; HL=1.46	p=<0.001; HL=1.39	p=0.58; HL=1.05	p=0.374; HL=0.89
Low Flows	2.6	p=<0.001; HL=0.36	p=<0.001; HL=0.17	p=<0.001; HL=0.57	p=<0.001; HL=0.37	p=0.011; HL=0.54	p=<0.001; HL=0.27	p=<0.001; HL=0.35	p=0.007; HL=0.73	p=0.117; HL=0.8	p=0.898; HL=0.97
Low Flows	4.5	p=<0.001; HL=0.35	p=<0.001; HL=0.12	p=<0.001; HL=0.41	p=<0.001; HL=0.07	p=<0.001; HL=0.38	p=<0.001; HL=0.21	p=<0.001; HL=0.56	p=<0.001; HL=0.05	p=0.547; HL=0.94	p=<0.001; HL=0.53
Low Flows	8.5	p=<0.001; HL=0.16	p=<0.001; HL=0	p=<0.001; HL=0.19	p=<0.001; HL=0.02	p=<0.001; HL=0.16	p=<0.001; HL=0.06	p=<0.001; HL=0.24	p=<0.001; HL=0.01	p=<0.001; HL=0.56	p=<0.001; HL=0.18